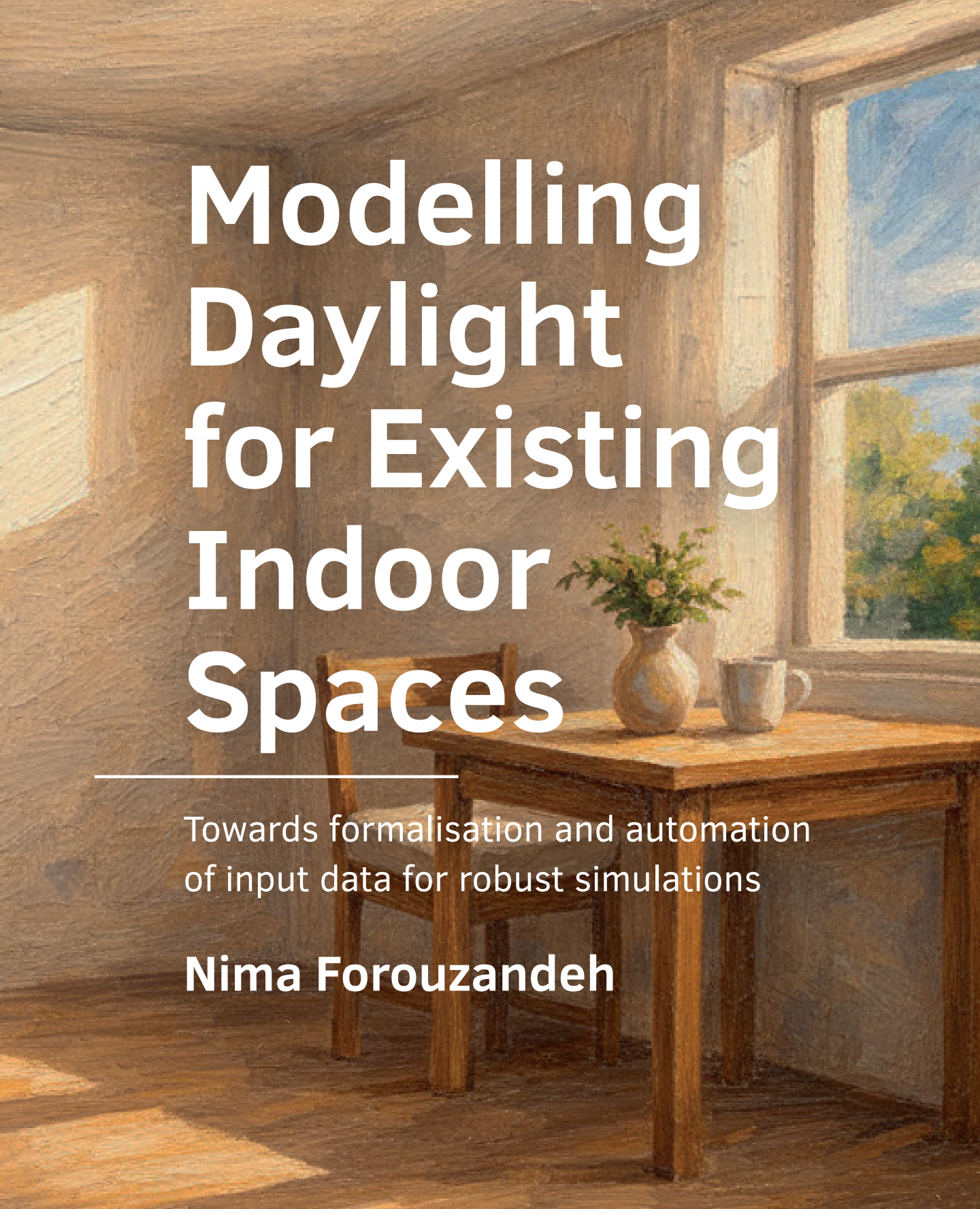

Modelling Daylight for Existing Indoor Spaces

Towards formalisation and automation of input data for robust simulations

Nima Forouzandeh

Modelling Daylight for Existing Indoor Spaces

Towards formalisation and automation of input data for robust simulations

Nima Forouzandeh

A+BE | Architecture and the Built Environment | TU Delft BK

26#05

Design | © Sirene Ontwerpers, Véro Crickx

Cover image | Nima Forouzandeh (AI-generated)

Keywords | Climate-based daylight modelling (CBDM), Existing buildings, Indoor geometry reconstruction, Image-based material characterization, spectral daylight simulation

ISBN 978-94-6384-918-0
ISSN 2212-3202

This dissertation is open access at https://doi.org/10.71690/abe.2026.05

Modelling Daylight for Existing Indoor Spaces

Towards formalisation and automation of input data for simulations

Dissertation

for the purpose of obtaining the degree of doctor
at Delft University of Technology
by the authority of the Rector Magnificus,
Prof.dr.ir. H. Bijl,
chair of the Board for Doctorates
to be defended publicly on
Wednesday, 18 March 2026 at 12:30

by

Nima FOROUZANDEH SHAHRAKI

This dissertation has been approved by the promotors.

Composition of the doctoral committee:

Rector Magnificus,	chairperson
Prof.dr. J.E. Stoter,	Delft University of Technology, promotor
Dr. E. Brembilla,	Delft University of Technology, copromotor
Dr. L. Nan,	Delft University of Technology, copromotor

Independent members:

Prof. dr. S.C. Pont,	Delft University of Technology
Em. prof. dr. J. Mardaljevic,	Loughborough University, United Kingdom
Dr. ir. S.J. Oude Elberink,	University of Twente
Dr. ir. R.C.G.M. Loonen,	Eindhoven University of Technology
Prof. dr. ir. M.J. Tenpierik,	Delft University of Technology, reserve member

Dr. J.A. Jakubiec of Toronto University has contributed greatly to the preparation of this dissertation.

Key words: Climate-based daylight modelling (CBDM), Existing buildings, Indoor geometry reconstruction, Image-based material characterization, spectral daylight simulation
Printed by: CB
Cover by: Nima Forouzandeh (AI-generated)

Series: A+BE | Architecture and the Built Environment
ISBN: 978-94-6384-918-0

An electronic version of this dissertation is available at: http://repository.tudelft.nl

To my family, mentors, and friends.

Acknowledgement

From the outset of my PhD, it became evident to me that what a large number of people contribute—both directly and indirectly—to its successful completion, often without being formally part of it. I am very grateful to have these few paragraphs to acknowledge those people—in many cases too briefly. I sincerely apologise to anyone I may have unintentionally left out.

My greatest gratitude goes to my supervisory team, Eleonora *Brembilla*, Liangliang *Nan*, and Jantien *Stoter*. I would like to acknowledge Eleonora for the important role she played in shaping my trajectory. Her feedback improved my work and manuscripts and were a great reminder to always start from simple before moving to complex. She provided me with the freedom to explore different directions throughout my PhD. I also benefitted from the supervision of the *3DGeoinformation* group. I would like to thank Liangliang for always making time to share his solid feedback on my work. His questions and comments were a great asset to my PhD. I am grateful to Jantien for being so kind as to meet and discuss important aspects of my PhD on several occasions, and for her openness to interdisciplinary research.

I am grateful to the members of my PhD committee: Prof. John *Mardaljevic*, Dr. Sander *Oude Elberink*, Dr. Roel *Loonen*, and Prof. Sylvia *Pont* for their constructive comments. Prof. Sylvia *Pont* also served on my Go/No-Go committee together with Dr. Michela *Turrin*, and both provided input that later helped refine my work.

I had a great opportunity, thanks to Eleonora's timely planning, to visit the *Design for Climate & Comfort Lab* at the *John H. Daniels Faculty of Architecture, Landscape, and Design* at the *University of Toronto* in my second year and to work with Dr. Alstan *Jakubiec*. Much of my current interest in spectral daylight sensing and simulation is a souvenir I began to carry from that period, through working closely with him.

I have also learned a great deal from my co-authors over the past years. Many thanks to Dr. Eleonora *Brembilla*, Dr. Lars O. *Grobe*, Dr. Jin *Huang*, Dr. Alstan *Jakubiec*, Shadi *Jami*, Dr. Maryam *Khoshbakht*, Dr. Dong-Hyun *Kim*, Dr. Liangliang *Nan*, Dr. Zohreh *Shaghaghian*, Prof. Jantien *Stoter*, Dr. Mohammad *Tahsildoost*, Dr. Mahsa *Zomorodian*, Dr. Shahram *Delfani*, Hanieh *Nourkojouri*, and Hanieh *Ahmadi*. I would also like to thank the many anonymous reviewers of our manuscripts. Our papers would certainly not have their final quality without their comments.

My PhD and scientific colleagues at AE+T played a big role in my daily PhD life and in

shaping my views on many matters. Our informal exchanges made the PhD experience richer and more human. I would like to thank Feras *Alsaggaf*, Cem *Ataman*, Nan *Bai*, Lourdes *Beneito*, Prateek *Bhustali*, Tess *Blom*, Adriana *Ciardiello*, Agnese *Chiucchiù*, Carla *Chacón Villanueva*, Simone *D'Amore*, Wilfried *Damen*, Pedro *de la Barra*, Erica *Ding*, Shivani *Dolas*, Berk *Ekici*, Tamara *Egger*, Amira *Elnouty*, Bodil *Eiterstraum*, Ahmed *Felimban*, Mahda *Foroughi*, Michiel *Fremouw*, Amneh *Hamida*, Hamza *Hamida*, Rebecca *Hartwel*, Menandros *Ioannidis*, Amin *Jalilzadeh*, Moses *Katontoka*, Kyujin *Kim*, Anna Maria *Koniari*, Aga *Kuś*, Brenda *Leoser*, Emeline *Lin*, Elham *Maghsoudi*, Federica *Marulo*, Ziead *Metwally*, Filippo *Molaioni*, Lara *Neuhaus*, Jack *O'Hagan*, Ruben *van der Plas*, Juan Carlos *Prazmowski*, Federica *Ramognoli*, Justin *Schembri*, Nick *ten Caat*, Raquel *Viula*, Prateek *Wahi*, Ziao *Wang*, and Yan *Zhou*. I am thankful to have been able to connect with each and every one of you—thank you. It was also a pleasure to connect with fellow PhDs in the *3DGeoinformation*: Lukas *Beuster*, Shenglan *Du*, Weixiao *Gao*, Nadine *Hobeika*, Jin *Huang*, Nail *Ibrahimli*, Camilo *León-Sánchez*, and Ivan *Pađen*—thank you. I also genuinely enjoyed the time spent with other PhD and scientific colleagues beyond the AE+T Department: Enshan *Chen*, Hazal *Deniz Kaya*, Casper *van Engelenburg*, Ömer *Faruk Ağırsoy*, Anna *Batallé Garcia*, Ghazal *Mosafer Zadeh*, Fatemeh *Mostafavi*, Maryam *Naghibi*, Ran *Pan*, Mark *van de Rout*, Saman *Seyff*, Gent *Shehu*, Pedram *Soltani*, Cynthia *Souaid*, Daniël *van Staveren*, Nima *Tabrizi*, Fatemeh *Vafaei*, Mônica *Veras Morais*, Cehao *Yu*, Vicente *Lenz*, and Halina *Zarate*.

Many of the ideas in this dissertation have emerged through numerous formal and informal discussions with experts I encountered during my PhD. I would like to thank Stef *Lhermitte* and Hugo *Ledeux* for their spot-on remarks and questions about surface interpolation used in the Illuminance-proxy technique; Charalampos *Andriotis* for sharing his views on ANN for image-based material characterisation; Seyran *Khademi* for sharing her expertise on material characterisation and photogrammetry; Peter *van Oosterom* for his remark on the standardisation of geometries during AE+T Bites; Valentine *Deschaintre*, James *Ferwerda*, and Xuejiao *Luo* for their support in testing their image-based material characterisation techniques; Stephan *Wasilewski* for his remark about calculating simulation time at the Radiance workshop in Innsbruck; Dr. Jan *Wienold* and Prof. Laura *Bellia* for brainstorming during LumeNet at EPFL on different parts of my work; Regina *Bokel* for her concise yet impactful questions and inputs during our chats. Thanks to Elmar *Eisenman* for our meeting on material characterisation, and especially for introducing me to Mark *van de Rout*, who was then a PhD colleague of his. Thank to Mark for his great comments on image-based material characterisation, metamerism, and his passion during our conversations. I extend my gratitude to Carmelo *Mineo* for providing implementation guidance on boundary-point detection; Linh *Truong-Hong* for providing code on point-cloud mapping and window detection; Filip *Biljecki* for his kind support for testing his Random3Dcity geometry-generation code; and, last but not least, Greg *Ward* for creating and maintaining *Radiance*.

Special thanks go to the different leaders of ECD section throughout the span of my PhD—Prof. Martin *Tenpierik*, Prof. Laure *Itard*, and Dr. Craig *Martin*. I was fortunate to be introduced to our section by the former manager assistant, Bo *Song*, and to have planned my defence with Annelies *Friesser*. I would like to extend my gratitude to the

other former and present members of the management and the secretariat team at AE+T: Sasha *Kasturiarachchi*, Carla *van der Krogt*, Daniel *Pantophlet*, Françoise *van Puffelen*, Yvonne *Vredeveld*, Tessa *Vermeulen*, and Linda *van Rijsbergen*, as well as the department managers, Dr. Onno *De Wit* and Kim *Scheffelaar*, and the department heads, Prof. Mauro *Overend* and Prof. Michiel *Kreutzer*. I am also grateful to the HR officers, Ms. Nathalie *Bast* and Ms. Julia *Kreuwel*, and to the PhD mentors from our department, Dr. Regina *Bokel* and Dr. Arjen *Meijer*. Many thanks to the Faculty Graduate School—Nouzha *Chamkh*, Inge *Meulenberg*, and Dr. Paul *Chan*. Thanks to Ms. Véro *Crickx* and Dr. Frank *Van der Hoeven* for their support with the book cover and thesis layout. Thanks to the former and present data stewards of our A+BE faculty, Dr. Diana *Popa* and Dr. Janine *Strandberg* for their help in managing my PhD data at different stages.

Special and heartfelt thanks to Tim *Schouws*, Thijs *Hamilton*, Maartje *Damen*, and Giorgos *Iliopoulos* for letting me be a member of their supervisory team. Thanks to my collaborators on these theses: Shervin *Azadi*, Dr. Pirouz *Nourian*, Dr. John *Heintz*, Dr. Roel *Schipper*, Prof. Christian *Louter*, Laura *Franx*, Prof. Sylvia *Pont*, Mônica *Veras Morais*, Dr. Giorgio *Aguigiaro*, Dr. Ken *Aroyo Ohori*, Dr. Azarakhsh *Rafiei*, Dr. Michela *Turrin*, and Herman *de Wolf*. Big thanks to Eleonora for organising the regular M.Sc. meetings and for giving me the opportunity to follow—and occasionally contribute to—the development of other students and their graduation projects.

I would also like to thank the professors and senior researchers I learned from and was pleased to connect with during *Radiance* workshops, the *LuxEuropa* conference, and *LumeNet*: Prof. Maryline *Andersen*, Prof. Laura *Bellia*, Dr. Kynthia *Chamilothori*, Dr. Jens *Christoffersen*, Dr. Juliëtte *van Duijnhoven*, Prof. Steve *Fotios*, Dr. David *Geisler-Moroder*, Prof. Myriam *McCulloch-Aries*, Dr. Andrew *McNeil*, Nicolas *Roy*, Dr. Roland *Schregle*, Rob *Shakespeare*, Prof. Manuel *Spitschan*, Greg *Ward*, and Dr. Jan *Wienold*. I am also grateful to the researchers I met at these events, whose discussions and exchanges were both stimulating and grounding: Margarita *Alwalidi*, Priji *Balakrishnan*, Lucien *Bickerstaff*, Catherine *Bratschi*, Giuseppe *De Michele*, Sietse *de Vries*, Abdelkader *El Kounni*, Myrta *Gkaintatzi-Masouti*, Meike *Goessling*, Frithjof *Hansen*, Sneha *Jain*, Dong Hyun *Kim*, Hanieh *Khodaei Tehrani*, Lukas *Liegener*, Iza *Linders*, Tahereh *Mallahnia*, Marshal *Maskarenj*, Pierre-Etienne *Merret*, Mohammad Mahdi *Mohammadi*, Miriam *Nader Elias*, Marzieh *Nazari*, Mikkel *Pedersen*, Valeria *Piccioni*, Elham *Rastegari*, Sarith *Subramaniam*, Stephen *Wasilewski*, Nicholas *Witton*, and Beatrice *Yuen*.

Beyond work, I was fortunate to spend time with kind and caring friends, sharing both joys and doubts. I would like to thank Ali, Amirhossein R., Amirhossein T., Fatemeh, Golnoush, Hasti, Hengameh, Leila, Mahdi, Mohamad, Mohammad, Saman, Sara, Sina, and Zahra. Your companionship was a true gift.

Thanks to the people who planned and managed so many exciting activities at X: Ashkan, Kjeld, Leila, Marco, Nuno, Olga, and Shamangi.

Finally, I would like to thank my family. I thank my mother, Zohreh, for instilling in me

a love for science and education; my father, Masoud, for his kindness and attentiveness; and Ramin, for being a great brother.

Summary

Despite the maturity of physically-based simulation tools, daylight modelling in existing buildings remains challenging. In practice, their applications are constrained by difficulties in acquiring, defining, and validating the input data. These limitations arise at multiple stages: reconstructing indoor geometry to meet the requirements of daylight models, accurately characterising material optical properties, and calibrating simulated models. Together, these aspects create bottlenecks that limit the reliability and broader applicability of such models in post-occupancy studies and retrofit analyses.

This dissertation develops and validates definitions and techniques for constructing, evaluating, and calibrating digital indoor models for daylight and spectral simulation, aiming to reduce error, effort, and time. It focuses on *developing and assessing (semi-)automatic workflows for the creation, characterisation, and calibration of indoor daylight models.*

To address this overarching goal, the following research questions are investigated:

- How sensitive are Climate-based daylight modelling (CBDM) results to geometric levels of detail?
- What are the uncertainties caused by inaccurate material definitions in CBDM results?
- How can indoor geometries be efficiently reconstructed to meet the requirements of daylight simulation models?
- To what extent can image-based material characterisation techniques be applied to indoor daylight models?
- How can simulated spectral indoor models be calibrated to account for uncertainties in scene reconstruction?

Research Methodology

A mixed-method approach combining modelling and measurement was employed. The research comprised five interconnected activities, each addressing one of the research questions.

The first activity introduced a data-driven definition of Geometrical Level of Detail (GLoD) for interior spaces. Five GLoDs were defined by incrementally including

non-permanent Oriented Bounding Box (OBB) areas, from GLoD0 (permanent shells only) to GLoD4 (complete geometry). Six case-study rooms were simulated using an advanced 2-phased *Radiance* method. Performance was evaluated in terms of Total Annual Illumination (TAI), spatial Root Mean Squared Error (RMSE), and computation time.

The second activity developed a measurement-informed definition of Material Class of Precision (MCoP) to quantify how uncertainty in optical properties propagates to annual daylight metrics. Based on 106 paired measurements using Average Hemispherical Reflectance (AHR) with a reflectance spectrophotometer as ground truth, four normal distributions ($\sigma \in [0.05,\ 0.20]$) were defined for reflectance and transmittance. Five GLoDs were combined with four MCoPs in a Monte Carlo experiment (500 iterations per cell; 60,000 simulations in total), with errors quantified using Percentage Error (PE), Mean Absolute Percentage Error (MAPE), and RMSE.

The third activity addressed the effort required to manually construct indoor geometry by leveraging a three-step *semi-automatic* pipeline for reconstructing simulation-ready GLoD0 geometry from point clouds. The workflow comprised: (1) preprocessing; (2) watertight reconstruction of permanent surfaces using *PolyFit* (Nan and Wonka, 2017); and (3) semi-automatic window boundary reconstruction through candidate patch detection, lasso-based selection, regularization, and trimming/extrusion.

The fourth activity evaluated three *image-based* techniques for estimating material reflectance—Illuminance-Proxy (Mardaljevic et al., 2015), Ferwerda (Ferwerda, 2018), and Luo (Luo et al., 2024)—and assessed their influence on daylight simulation. In addition, a spectral uplifting method (Jakob and Hanika, 2019) was also tested to reconstruct full spectral reflectance from Red, Green, Blue (RGB) inputs, which supports non-visual daylight simulations.

The final activity introduced and tested a *calibration* workflow for indoor spectral daylight simulation that addresses key uncertainty sources in scene reconstruction—sun–sky conditions, exterior obstructions, and window spectral transmittance—by selecting window transmittance as a single tunable parameter. Short-term field measurements in a university classroom under overcast conditions were used to identify the optimal transmittance scaling by minimising 18-channel irradiance errors.

Results

– *Sensitivity of CBDM results to geometric levels of detail*

Gradual exclusion of non-permanent objects from GLoD4 to GLoD0 increases average TAI error by ≈1.08% to 18.05% respectively, with the largest deviations around object locations where daylight was obstructed. Errors are higher in densely furnished rooms and lower in open rooms. Computation time drops substantially (up to ∼3×) as geometry is simplified. In practice, GLoD2 (removing objects with OBB

area $< 2.4\ \mathrm{m}^2$) limits average TAI error to $< 10\%$–15% while providing large speed gains, offering a pragmatic balance for early analyses; higher GLoDs are advisable for detailed design or dense furnishings.

- *Sensitivity of CBDM results to uncertainty in defining material properties*

  Output TAI distributions widen consistently with increasing input uncertainty, while medians remain stable. Distributions are generally symmetric but often deviate from normality, indicating the presence of non-linear transformations in the simulation. Uncertainty in predicting annual results increases approximately linearly with MCoP across spaces and GLoDs. In the most complete geometry (GLoD4), median uncertainty spans $\sim$10%–35% depending on the room (narrower in some spaces and 5%–15% in one high-window case). Spatial analysis shows larger uncertainty near glazing, implicating window *transmittance* as the dominant contributor compared to surface *reflectance*.

- *Efficient geometry reconstruction* Across multiple rooms of varying sizes, shapes, and window complexity, the semi-automatic pipeline reconstructs GLoD0 models with a total modelling time (user + compute) under 5 minutes for successful cases. Useful Daylight Illuminance (UDI) absolute error is $< 10\%$; mean TAI percentage error is within 12%–18% for rooms with rectangular windows and up to 44% for rooms with non-rectangular or arched openings; Daylight Glare Probability (DGP) RMSE is < 0.04. Advantages include watertightness, the inclusion of window extrusion, reduced user interaction to mitigate false detections, and a symmetric-window prior more robust than strict rectangularity. Limitations include planarity assumptions, missing mullions and co-planar subsurfaces, challenges with arched openings, susceptibility to complex geometries, omission of beams/columns, and untested multi-room scalability.

- *Image-based material characterisation* Ferwerda's technique provides the most balanced performance (Mean Relative Bias (MRB)$\approx$13%, Root Mean Squared Relative Error (RMSRE)$\approx$31%) with stable results across lighting, TAI overestimation of 33%–65%, and negligible influence on DGP (< 0.02). Illuminance-Proxy achieves MRB$\approx$19% and RMSRE$\approx$41% but overestimates TAI by $\sim$101% in the case study, performing best on diffuse, planar surfaces under smooth illumination. Luo's method exhibits the largest errors in reflectance ($\Delta\rho$ up to 0.48; ΔE_{ab} up to $\sim$70) and TAI overestimation ($\sim$134%). Spectral uplifting reconstructs full spectra with wavelength-wise RMSRE $< 20\%$ and Melanopic equivalent daylight illuminance (m-EDI) deviation $< 6\%$, confirming that tristimulus inputs can support spectral daylight simulations with small added uncertainty.

- *Spectral calibration*

  Simulated–measured spectral shapes agree well even before calibration (Pearson $r = 0.89$–0.92), explaining the stability of the M/P ratio. After scaling the window transmittance spectrum while preserving its shape, systematic bias on the control sensor is nearly eliminated for Photopic Illuminance (E_v) and m-EDI ($\mathrm{MBE}_{\mathrm{rel}} \in [-5.8\%,\ 2.7\%]$), with total error magnitude $\mathrm{RMSE}_{\mathrm{rel}} \approx 18\%$ and dispersion $\sigma_{\mathrm{rel}} \approx 18\%$. Residual spatial errors increase with distance from the façade, indicating that inter-reflections and local modelling inaccuracies dominate at greater depths.

Samenvatting

Ondanks de volwassenheid van fysisch gebaseerde simulatieprogramma's blijft daglichtmodellering in bestaande gebouwen uitdagend. In de praktijk worden toepassingen beperkt door moeilijkheden bij het verkrijgen, definiëren en valideren van essentiële invoergegevens. Deze beperkingen doen zich voor in verschillende fasen: het reconstrueren van de binnengeometrie volgens de eisen van daglichtmodellen, het nauwkeurig karakteriseren van materiaaleigenschappen en het kalibreren van de gesimuleerde modellen. Gezamenlijk vormen deze aspecten knelpunten die de betrouwbaarheid en toepasbaarheid van dergelijke modellen voor bestaande gebouwen, zoals voor post-occupancy-studies en renovatieanalyses, beperken.

Dit proefschrift ontwikkelt en valideert definities en technieken voor het opbouwen, evalueren en kalibreren van digitale binnenmodellen voor daglicht- en spectrale simulatie, met als doel de fout, inspanning en rekentijd te verminderen. De nadruk ligt op het ontwikkelen en beoordelen van (semi-)automatische workflows voor het opstellen, karakteriseren en kalibreren van binnendaglichtmodellen voor bestaande gebouwen.

Om dit overkoepelende doel te bereiken, worden de volgende onderzoeksvragen onderzocht:

- Hoe gevoelig zijn Climate-based daylight modelling (CBDM)-resultaten voor geometrische detailniveaus?
- Welke onzekerheden ontstaan door onnauwkeurige materiaalspecificaties in CBDM-resultaten?
- Hoe kunnen binnengeometrieën efficiënt worden gereconstrueerd voor daglichtsimulatie?
- In welke mate kunnen beeldgebaseerde technieken worden toegepast voor materiaal karakterisering?
- Hoe kunnen spectrale binnenmodellen worden gekalibreerd om onzekerheden in reconstructie te compenseren?

Onderzoeksmethode

Er is een gecombineerde aanpak gebruikt gebaseerd op modellering en meting. Het onderzoek bestaat uit vijf samenhangende onderdelen, elk gericht op één onderzoeksvraag.

Het eerste onderdeel introduceert een data-gedreven definitie van Geometrical Level of Detail (GLoD) voor binnenruimtes. Vijf niveaus werden gedefinieerd door stapsgewijs niet-permanente objecten toe te voegen met behulp van Oriented Bounding Box (OBB)-oppervlakken, van GLoD0 (enkel permanente schillen) tot GLoD4 (volledige geometrie). Zes praktijkruimtes werden gesimuleerd met een geavanceerde tweefasen-*Radiance*-methode. De prestaties werden geëvalueerd op basis van totale jaarlijkse verlichtingssterkte (Total Annual Illumination (TAI)), ruimtelijke Root Mean Squared Error (RMSE) en rekentijd.

Het tweede onderdeel ontwikkelt een meet-geïnformeerde definitie van Material Class of Precision (MCoP) om te kwantificeren hoe onzekerheden in optische eigenschappen zich voortplanten naar jaarlijkse daglichtstatistieken. Op basis van 106 gekoppelde metingen met een Average Hemispherical Reflectance (AHR) en een reflectantie-spectrofotometer als referentie werden vier normale verdelingen ($\sigma \in [0.05,\ 0.20]$) gedefinieerd voor reflectantie en transmissie. Vijf GLoDs werden gecombineerd met vier MCoPs in een Monte Carlo-experiment (500 iteraties per cel; in totaal 60.000 simulaties). Fouten werden gekwantificeerd met Percentage Error (PE), Mean Absolute Percentage Error (MAPE) en Root Mean Squared Error (RMSE).

Het derde onderdeel richt zich op het verminderen van de handmatige inspanning bij het modelleren van binnengeometrie via een driefasen *semi-automatische* pipeline om simulatie-klare GLoD0-modellen te reconstrueren uit puntenwolken. De workflow omvat: (1) voorbewerking; (2) waterdichte reconstructie van permanente oppervlakken met *PolyFit* (Nan and Wonka, 2017); en (3) semi-automatische reconstructie van raamgrenzen via detectie van kandidaat-vlakken, selectie met een lasso-tool, regularisatie en extrusie.

Het vierde onderdeel evalueert drie *beeldgebaseerde* technieken voor het schatten van materiaalreflectantie—Illuminance-Proxy (Mardaljevic et al., 2015), Ferwerda (Ferwerda, 2018) en Luo (Luo et al., 2024)—en hun invloed op daglichtsimulatie. Daarnaast werd een spectrale reconstructiemethode (Jakob and Hanika, 2019) getest om volledige spectra te reconstrueren uit Red, Green, Blue (RGB)-inputs, wat niet-visuele daglichtsimulaties ondersteunt.

Het laatste onderdeel introduceert en test een *kalibratie*-workflow voor spectrale binnendaglichtsimulatie die rekening houdt met onzekerheden in scène-reconstructie—zon-hemelcondities, externe obstructies en spectrale transmissie van ramen—door de raamtransmissie als enige afstembare parameter te gebruiken. Korte veldmetingen onder bewolkte omstandigheden werden gebruikt om de optimale transmissieschaal te bepalen door 18-kanaals irradiantie-fouten te minimaliseren.

Resultaten

- *Geometrische gevoeligheid* Het weglaten van niet-permanente objecten van GLoD4 naar GLoD0 verhoogt de gemiddelde TAI-fout van ongeveer 1,1% tot 18%, met de grootste afwijkingen nabij objectlocaties. Fouten zijn groter in dicht gemeubileerde ruimten. De rekentijd daalt tot circa 3× bij vereenvoudigde geometrie. GLoD2 biedt een praktische balans (fout <10–15%) met aanzienlijke snelheidswinst.
- *Onzekerheid in materiaaleigenschappen* De spreiding van Total Annual Illumination (TAI)-resultaten neemt lineair toe met de MCoP. Medianen blijven stabiel, maar de verdelingen volgen niet een normale verdeling. In GLoD4 varieert de mediaan onzekerheid van 10–35%, afhankelijk van de ruimte. De grootste onzekerheid bevindt zich nabij ramen, wat aangeeft dat transmissie een dominantere rol speelt dan reflectie.
- *Efficiënte geometrische reconstructie* De semi-automatische pipeline reconstrueert GLoD0-modellen in minder dan 5 minuten per ruimte. UDI-fout is <10%, TAI-fout 12–18% (tot 44% bij niet-rechthoekige openingen) en DGP-RMSE <0,04. De sterke punten van de pipeline zijn: waterdichtheid, raamextrusie, minder gebruikersinteractie en robuustheid tegen foutdetecties. De beperkingen zijn: vlakheidsaanname, ontbrekende stijlen/delen, beperkte toepasbaarheid op complexe of meervoudige ruimtes.
- *Beeldgebaseerde materiaalkarakterisering* Ferwerda's methode levert de meest gebalanceerde prestaties (Mean Relative Bias (MRB)≈13%, Root Mean Squared Relative Error (RMSRE)≈31%), met stabiele resultaten en beperkte invloed op DGP (<0,02). Illuminance-Proxy overschat TAI sterk (101%) maar werkt goed bij diffuse, vlakke oppervlakken. Luo's methode vertoont de grootste fouten ($\Delta\rho$ tot 0,48; ΔE_{ab} tot 70). Spectrale reconstructie bereikt een golflengte-RMSRE <20% en m-EDI-afwijking <6%, wat de bruikbaarheid van RGB-inputs bevestigt.
- *Spectrale kalibratie* Gesimuleerde en gemeten spectra komen goed overeen (Pearson $r = 0{,}89$–$0{,}92$). Na schaalcorrectie van de raamtransmissie is de systematische bias vrijwel verdwenen ($\mathrm{MBE}_{\mathrm{rel}} \in [-5{,}8\%,\ 2{,}7\%]$), met $\mathrm{RMSE}_{\mathrm{rel}} \approx 18\%$. De resterende ruimtelijke fouten nemen toe met afstand tot de gevel.

Contents

Summary vii
Samenvatting xi
Acknowledgement vii
List of Acronyms xviii
List of Figures xxvii
List of Tables xxx

1 **Introduction** 1

1.1 **Overview** 1
1.2 **Research Outline** 3
1.2.1 Problem statement and research gaps 3
1.2.2 Research Aim and Objectives 4
1.3 **Outline of this dissertation** 5

2 **Sensitivity of CBDM results to Geometrical Levels of Detail** 9

2.1 **Introduction** 10
2.2 **Literature review** 11
2.3 **Data and Methods** 12
2.3.1 Geometrical Level of Detail (GLoD) 12
2.3.2 Case study spaces and input preparation 13
2.3.3 Simulation setup 16
2.3.4 Error calculation 17
2.4 **Results** 17
2.4.1 Definition of GLoDs 17
2.4.2 Influence of varying GLoDs 17

2.5 **Discussion** 21
2.6 **Conclusion** 22

3 **Sensitivity of CBDM Results to Material Classes of Precision** 25

3.1 **Introduction** 26
3.2 **Literature review** 26
3.3 **Data and methods** 27
3.3.1 Case study spaces 27
3.3.2 Material Class of Precision (MCoP) 27
3.3.3 Monte Carlo simulation 28
3.3.4 Simulation setup 31
3.3.5 Error calculation and uncertainty measures 31
3.4 **Results** 31
3.4.1 Annual simulation results 31
3.4.2 Influence of varying MCoPs 32
3.5 **Discussion** 33
3.6 **Conclusion** 37

4 **Semi-automatic reconstruction of room geometry** 41

4.1 **Introduction** 42
4.2 **Literature review** 43
4.3 **Methodology** 47
4.3.1 Reconstruction pipeline 47
4.3.1.1 Preprocessing 48
4.3.1.2 Permanent structure reconstruction 49
4.3.1.3 Window reconstruction 49
4.3.2 Implementation 51
4.3.3 Use case rooms 52
4.3.4 Generation of ground truth models 53
4.3.5 Performance evaluation 53

4.4 **Results** 56
4.4.1 Visual comparison 57
4.4.2 Geometrical comparison 57
4.4.3 Daylight availability 57
4.4.4 Glare 64
4.5 **Discussion** 65
4.5.1 Advantages 65
4.5.2 Limitations 67
4.6 **Conclusion** 68

5 **Characterisation of material optical properties** 71

5.1 **Introduction** 72
5.2 **Literature review** 74
5.3 **Methodology** 75
5.3.1 Material data collection 76
5.3.1.1 Ground truth 76
5.3.1.2 Illuminance proxy 77
5.3.1.3 Luo's method 79
5.3.1.4 Ferwerda's method 81
5.3.1.5 Spectral uplifting 82
5.3.2 Performance evaluation 82
5.4 **Results** 84
5.4.1 Tristimulus and reflectance estimations 84
5.4.2 Impact on daylight availability and visual comfort 89
5.4.3 Spectral uplifting 90
5.5 **Discussion** 92
5.6 **Conclusion** 96

6 **Calibration of a spectral daylight model** 99

6.1 **Introduction** 100

6.2 **Literature Review** 102

6.3 **Methods** 107

6.3.1 Use case room 108

6.3.2 Spectral light measurements 108

6.3.3 Simulated model 109

6.3.4 Calibration workflow 111

6.3.4.1 Finding the best-performing window 112

6.3.4.2 Evaluation of the calibrated models 113

6.4 **Results** 114

6.4.1 Best-performing window 114

6.4.2 Errors in the calibrated models 114

6.5 **Discussion** 120

6.6 **Conclusion** 121

7 **Conclusions, Reflections and Future Research** 123

7.1 **Conclusions** 124

7.1.1 Answers to the research questions 124

7.1.1.1 RQ1: How sensitive are Climate-based daylight modelling (CBDM) results to geometric levels of detail? 124

7.1.1.2 RQ2 – What are the uncertainties caused by inaccurate material definition in CBDM results? 125

7.1.1.3 RQ3 – How can indoor geometries be efficiently reconstructed to meet the requirements of daylight simulation models? 126

7.1.1.4 RQ4 – To what extent can image-based material characterisation techniques be applied to simulated indoor daylight models? 127

7.1.1.5 RQ5 – How can simulated spectral indoor models be calibrated to account for uncertainties in scene reconstruction? 128

7.2 **Key Contributions** 129

7.3 **Future Work** 131

7.3.1 RQ1 131

7.3.2 RQ2 131

7.3.3 RQ3 132

7.3.4 RQ4 133
7.3.5 RQ5 133
References 135
APPENDIX A Uncertainty indicators 141
APPENDIX B Results of the normality test 143
APPENDIX C UDI and TAI simulation results 145
APPENDIX D Temporal Mean Relative Bias 147
APPENDIX E Results of the three-channel illuminance-proxy 149
Curriculum Vitæ 151

List of Acronyms

AABB Axis-aligned Bounding Box.

AC Air Conditioning.

AE Absolute Error.

AECO Architecture, Engineering, Construction, Operation.

AHR Average Hemispherical Reflectance.

ASE Annual Sunlight Exposure.

ASHRAE American Society of Heating, Refrigerating and Air-Conditioning Engineers.

BIM Building Information Modelling.

BREEAM Building Research Establishment Environmental Assessment Method.

CAD Computer-aided design.

CBDM Climate-based daylight modelling.

CCT Correlated Colour Temperature.

CD Chamfer Distance.

CIBSE Chartered Institution of Building Services Engineers.

CIE Commission Internationale de l'Éclairage.

CS Circadian Stimulus.

CVRMSE Coefficient of Variation of the Root Mean Square Error.

DDS Dynamic Daylight Simulation.

DF Daylight Factor.

DGP Daylight Glare Probability.

DHE Diffuse Horizontal Illuminance.

DHI Diffuse Horizontal Irradiance.

DNE Direct Normal Illuminance.

DNI Direct Normal Irradiance.

DSLR Digital Single-lens Reflex [camera].

E_v Photopic Illuminance.

GHI Global Horizontal Irradiance.

GLoD Geometrical Level of Detail.

GUI Graphical User Interface.

HD Hausdorff Distance.

HDR High Dynamic Range.

IIL ipRGC-influenced light.

ipRGC intrinsically Photosensitive Retinal Ganglion Cells.

LED light-emitting diode.

LEED Leadership in Energy and Environmental Design.

LiDAR Light Detection and Ranging.

LoD Levels of Detail.

m-EDI Melanopic equivalent daylight illuminance.

MAE Mean Absolute Error.

MAPE Mean Absolute Percentage Error.

MBE Mean bias error.

MCoP Material Class of Precision.

MPC Model Predictive Control.

MRB Mean Relative Bias.

NIF Non-image forming.

NMBE Normalized Mean bias error.

OBB Oriented Bounding Box.

PCA Principal Component Analysis.

PE Percentage Error.

POE Post-occupancy Evaluation.

RANSAC Random Sample Consensus.

RB Relative Bias.

RGB Red, Green, Blue.

RMSE Root Mean Squared Error.

RMSRE Root Mean Squared Relative Error.

SA Sensitivity Analysis.

SCE Specular component excluded.

SCI Specular component included.

sDA spatial Daylight Autonomy.

SPD Spectral Power Distribution.

STD Standard Deviation.

SVBRDF Spatially variant bidirectional reflectance distribution function.

TAI Total Annual Illumination.

TAO Tropical Atmosphere Ocean.

TMRB Temporal Mean Relative Bias.

UDI Useful Daylight Illuminance.

VLT Visible Light Transmission.

WFR Window-to-Floor Ratio.

WWR Window-to-wall Ratio.

List of Figures

1.1 Structure of this dissertation. 6

2.1 Bounding geometries. From left to right: (a) Surrounding Sphere, (b) Axis-aligned bounding box, (c) OBB, and (d) Convex hull. 13

2.2 Summary of object sizes in the case study spaces. 14

2.3 Additional case study spaces for GLoD definition – 3D views. 15

2.4 3D representation of spaces in multiple GLoDs. The number of objects is indicated above each GLoD. 18

2.5 The GLoD where each semantic first appears in the models. Some of the semantics appear in different GLoDs for the first time, which are indicated in *italics*. 18

2.6 Influence of geometrical resolution on annual illuminance predictions (PE [%]) 19

2.7 Influence of geometrical resolution on annual illuminance predictions (RMSE [lx]). 19

2.8 Influence of geometrical resolution on annual daylight results - GLoD0 and GLoD4 20

2.9 Influence of geometrical resolution on simulation time 21

3.1 Bell curve fitted to AHR errors compared against measurements from a reflectance spectrophotometer. 29

3.2 An example of four MCoPs used in the Monte Carlo simulation. In this example the ground truth is 0.6. 29

3.3 The GLoD-MCoP matrix. 29

3.4 Workflow of the uncertainty quantification study. 30

3.5 Convergence experiment to determine the sufficient number of simulations — for room *WBG640* (MCoP0.2, GLoD4)). 500 simulations is considered sufficient. 30

3.6 TAI results for GLoD4. Box plots show the inter-quartile ranges for each GLoD-MCoP combination. The highest and lowest 5 percentiles are considered and visualized as outliers. Note that the scales in the y-axis differ for *DA_200* and *WBG550* for better readability. 33

3.7 UDI maps for the six spaces. The considered UDI range is 300-3000 lx. 34

3.8 Distribution of errors in the estimation of the TAI for space DA_200 with the four different MCoP and the fitted normal probability density functions for each one (*DA_200*). 35

3.9 Influence of varying MCoP. 36

3.10 Spatial distribution of prediction errors caused by inaccurate material definition (MCoP0.2-GLoD4–W01050). 37

3.11 Uncertainty in the calculation of annual grid-based illuminance values. Crosses represent the uncertainty as calculated in Eq. A.3. Gradient colours represent the interpolated uncertainty across the 2D domain of 0.05–0.20 reflectance–transmittance independent uncertainties. 38

4.1 Reconstruction pipeline. Manual steps are shown in black, and automated steps are shown in white. Visual examples beside each block illustrate the corresponding stage of the process, from raw scanning to final 3D model generation. 48

4.2 An example of permanent structure reconstructed using *PolyFit* (left) and user wall selection (right). 49

4.3 Candidate window patch detection workflow. Triangles exceeding the edge-length threshold from the Delaunay triangulation are classified as *holes* (white faces), while the remaining faces are non-hole faces (grey faces). Connected hole faces are grouped into labelled *regions*, and regions that satisfy the area criterion are identified as *candidate window patches (yellow edge)*. 50

4.4 User window patch selection, while user draws the lasso tool (left) and completed selection (right). 51

4.5 A screen shot of the program during the user interaction. 52

4.6 Point clouds and an indoor view from the five rooms used for this study. 54

4.7 Selected views for glare analysis 56

4.8 Intermediate and final visualizations from the four successful reconstruction cases. From left to right: input point cloud, visible points and surfaces prior to user wall selection, user-marked window region, final 3D model, a fisheye render from the glare views corresponding to Fig. 4.7. 58

4.9 A failure case. The *OrangeHall* contains a large number of points capturing interior objects, such as large exhibition objects and large staircases, resulting in undesired permanent structure reconstructed by *PolyFit*. 59

4.10 Comparison of manually reconstructed (in black) with the proposed semi-automatic technique (in red). 60

4.11 TAI heat maps for semi-automatic (bottom) and manual (middle) geometries, along with their bias (top). 62

4.12 Temporal illuminance relative bias across rooms. Left: sensor locations. Right: corresponding relative bias (RB). 63

4.13 False colour images of the summer solstice time step for manual (left) and semi-automatic (right) geometries. 64

4.14 DGP for manual and semi-automatic reconstruction pipelines 65

5.1 Case study room as seen with a fisheye camera from two points and two directions. 76

5.2 Ground-truth measurement setup: reflectance spectrophotometer and its calibration module. 77

5.3 Inputs for the illuminance-proxy method. From left to right: luminance map [cd/m^2], example mask indicating the area of interest for the whole wall, spots of known reflectance 78

5.4 Masks with a unique material for an example wall. 78

5.5 Input HDR for three-channel illuminance-proxy. Courtesy of Dong Hyun Kim, captured at LIPID lab, EPFL, 2024. 79

5.6 Input region and points of interest for three channel illuminance proxy, blue diamonds are the points with known reflectance, red dots are the points of interest. 80

5.7 Phone cap to block ambient light and prevent inter-reflections. 80

5.8 An example original input image (left) and output from Luo's method (right), consisting of diffuse reflectance, specular component, roughness, and normal maps. 81

5.9 Different lighting conditions for testing Ferwerda's technique: daylight only (left), electric lighting only (middle), and mixed daylight and electric lighting (right). 81

5.10 Selected view for spectral simulation, same case study room as for previous analyses. 82

5.11 Output reflectance map from three channel illuminance-proxy. 86

5.12 Absolute RGB error values for 19 query points across the two samples for the three-channel illuminance-proxy. 87

5.13 Comparison of visible reflectance for Luo, Ferwerda, and illuminance-proxy. 87

5.14 Colour differences with ground truth in terms of ΔEab for Luo and Ferwerda. 88

5.15 Colour differences with ground truth in terms of ΔEab for Ferwerda's technique under different lighting conditions. 88

5.16 A rendered view of the case study room with the four set of material properties from left to right: ground truth, illuminance-proxy, Ferwerda's, and Luo's. 89

5.17 A rendered view of the case study room with materials obtaind from the Ferwerda's technique under different lighting conditions, from left to right: daylight, electric, mixed, and cap. 90

5.18 Comparison of different characterisations (top), and influence of different lighting conditions for Ferwerda's method (bottom). The histograms on the top and right sides of the graphs show the frequency of occurring DGP results. 91

5.19 Spectral Absolute Error (AE), RMSRE, and MRB across visible wavelengths for 801 samples. 92

5.20 Comparison of spectral irradiance simulated at a fixed viewpoint, using measured and uplifted spectral reflectance as input. From top pair to the bottom one: (1) June 22nd – 11:00, (2) June 22nd – 9:00, (3) June 22nd – 9:00, and (4) June 22nd – 11:00. 93

6.1 Influencing inputs in indoor spectral irradiance simulation. 102

6.2 3D model and real fisheye view of the studied room. 109

6.3 Irradiance inside and outside of the window for transmittance calculation. This is measured by Konica Minolta CL-500A. 109

6.4 m-EDI values from measurement. 110

6.5 Preparation of measured and simulated data 110

6.6 Schematic prioritisation matrix for designing a calibration workflow for each influencing parameters listed in Fig.6.1. 111

6.7 Calibration pipeline 112

6.8 Spectral properties of the window materials for each iteration of the calibration process. The dashed lines represent the positive adjustments, the dotted lines represent the negative adjustments, and the solid black line represents the measured data. The Visible Light Transmission (VLT) of each option is in the parenthesis. 113

6.9 Spectral comparison for a single example time step at the control nanoLambda sensor after calibration. 115

6.10 Spectral transmittance of *Window_neg_3* window. 116

6.11 Spectral simulation errors on the control sensor before (top) and after calibration (bottom). 116

6.12 Comparison of measured and simulated E_v and m-EDI, before and after calibration for the control sensor and the other sensors; sensor locations as shown in Fig. 6.2. 117

6.13 Spatial pattern of accuracy (MBE_{rel}) and precision (σ_{rel}) after calibration. Point size indicates the magnitude of the metric. 118

List of Tables

2.1 Descriptions of the case study rooms. 14

2.2 Case study Rooms – 3D representation. 15

2.3 Additional case study spaces for GLoD definition—general information. 16

2.4 Influence of geometrical resolution on annual daylight results - RMSE and PE. 20

4.1 A summary of the reconstruction algorithms. The listed works are not applied to daylight simulation. 45

4.2 RANSAC parameters used in this work for plane extraction 49

4.3 Description of the rooms 53

4.4 Geometric comparison between manually and semi-automatically reconstructed models (distances in metres). 57

4.5 ASE and sDA results 59

4.6 Spatial relative bias of UDI for (i)nsufficient, (a)utonomous, and (e)xceeding ranges. 61

4.7 Summary of spatial relative bias for TAI 61

5.1 DNI, DHI, Global Horizontal Irradiance (GHI), Direct Normal Illuminance (DNE), and Diffuse Horizontal Illuminance (DHE) values for the Summer solstice (June 21) at three times of day, used in the spectral simulations. 83

5.2 Interpolated illuminance map, reflectance map, and mean reflectance for five main surfaces of the studied room 85

5.3 Overall performance of illuminance-proxy, Ferwerda, and Luo for estimation of visible reflectance. 86

5.4 Overall performance of Ferwerda's technique under different lighting conditions. 88

5.5 TAI values and corresponding Percentage Error (PE) for illuminance-proxy, Ferwerda, and Luo in use case room. 90

5.6 Overall performance of Ferwerda's technique under different lighting conditions. 90

5.7 Simulated m-EDI with measured and uplifted spectral materials. 92

5.8 Comparison of different methods and corresponding MRB and RMSRE values. Results from AHR, ENTPE, and Sample chart are measured by Bodart et al. (2008). 93

5.9 TAI Percentage Errors for Different Methods 94

6.1 Lighting recommendations for different indoor environments (Brown et al., 2022). 101

6.2 Summary of validation and calibration studies for indoor daylight simulation. 104

6.3 $MAE_{room,w}$ and correlation for different windows 115

6.4 Relative error metrics before and after calibration for each sensor, the sensors are sorted based on their distance from the front facade. 119

B.1 Results of the normality test (p-value); normal distributions with p-values higher than 0.05 are marked with (*). 143

C.1 TAI [Mlx.hr/year] 145

C.2 UDI_i [%] 145

C.3 UDI_a [%] 146

C.4 UDI_e [%] 146

D.1 Summary of spatial TMRB values. 147

E.1 Estimated RGB values for each sample grouped by Ground Truth (GT). 149

1 Introduction

1.1 Overview

Obtaining desired levels of daylight is crucial for a healthy building design. Low exposure to daylight hinders the functioning of occupants and can lead to symptoms of depressive disorder and seasonal affective disorder (Tregenza and Wilson, 2013). Sufficient daylight has also been shown to mitigate the progression of childhood myopia (Chakraborty et al., 2018). This is even more critical in buildings where occupants are confined indoors and do not have free access to the outdoors, *e.g.*, hospitals (Tregenza and Wilson, 2013). On the flip side, excessive exposure to daylight can cause discomfort, glare and increase the risk of overheating. Optimising daylight levels in building design can significantly enhance well-being, regulate the circadian rhythm, and improve productivity while mitigating issues associated with inadequate or excessive exposure to natural light Heschong (1999, 2006); Lee et al. (2022); Knoop et al. (2020).

To predict the daylight performance of buildings at the design stage, numerical evaluation of daylight provision and occupant comfort based on digital models of the design has become an indispensable part of the design process. This has been recognized by national and international standardisation entities such as the European Committee for standardisation (CEN) (CEN, 2018) and building certification programmes such as Leadership in Energy and Environmental Design (LEED), Building Research Establishment Environmental Assessment Method (BREEAM), and WELL (USGBC, 2014; Building Research Establishment (BRE), 2023; International WELL Building Institute (IWBI), 2023). They all mandate acceptable levels of daylight to ensure environmental sustainability and to meet occupants' comfort, increasingly relying on annual metrics calculated with Climate-based daylight modelling (CBDM) as a reliable daylight simulation technique.

Simulation models are not only predictors of newly designed interiors, but they can also be instrumental in Post-occupancy Evaluation (POE) of buildings. POE studies aim to provide evidence from existing buildings to improve the design of future buildings and serve as a basis for testing various retrofit strategies. Retrofitting existing buildings provides a significant opportunity to improve building performance and reduce their energy use by up to 84% (Regnier et al., 2018). Besides, the

replacement of existing buildings by newly constructed ones is very low. In the UK, for instance, this turnover is less than 1% per year (Roberts, 2008). It is estimated that more than 90% of the energy consumption of the buildings after 2050 will be from buildings built before 2000 (IEA, 2011). Thus, retrofitting the existing building stock is one of the main ways to achieve higher levels of occupant satisfaction while minimizing energy consumption in the built environment, which has attracted considerable attention from policymakers and building owners.

To achieve that goal, physically-based simulations are crucial tools for practitioners. With daylight as a key performance aspect of indoor spaces, several researchers implemented simulation as a retrofit decision support tool to optimize the design of different elements within the indoor space. These elements include skylights (Bian et al., 2021), inner windows (Koh et al., 2020), partitions (Abdollahzadeh et al., 2020), and louver systems (Hashemi, 2014), or electric lighting systems (Zhou et al., 2015). Jradi et al. further proposed retrofit packages rather than focusing on one component of the space (Jradi et al., 2017).

Daylight models are also implemented as part of the buildings' digital twins and for active Model Predictive Control (MPC) systems. Digital twins consist of five main parts: (1) a physical part that is the real-world object or space being represented virtually using the (2) virtual part, alongside the (3) connections which require data transfer from the physical part to the virtual representation with a non-mandatory feedback component, (4) data, and (5) services, *i.e.*, the action of controlling building elements (Jiang et al., 2021). In the case of daylight models, this includes simulation and control decision-making for shading system and electric lighting control systems.

A physically based daylight model requires five key inputs: (1) a 3D model of the indoor environment, (2) optical properties of its interior surfaces, (3) a 3D model of the outdoor context, and (4) optical properties of the outdoor context, together with (5) the sky luminance distribution. The first two are, unlike 3, 4, and 5, building-specific and cannot be characterised and reconstructed on a large scale. This makes the whole modelling resource-intensive and time-consuming.

This dissertation proposes definitions and techniques for daylight modelling in existing indoor spaces, with an emphasis on models whose performance remains stable and reliable across a wide range of conditions.

This dissertation primarily targets the automation of these two essential inputs for daylight simulation—the reconstruction of indoor 3D geometry and the characterisation of material optical properties. However, even when these inputs are defined with high fidelity, systematic discrepancies often remain due to factors such as sun–sky conditions and exterior obstructions. Consequently, a calibration workflow is included as an often necessary step to align simulations with field measurements and improve reliability.

1.2 Research Outline

The dissertation focuses on automating the reconstruction of indoor geometry and the characterisation of material properties, which constitute the two principal inputs of daylight simulation. Yet, accurate inputs alone do not guarantee perfect agreement between simulated and measured light levels; residual errors commonly persist (*e.g.*, from sky/solar variability and exterior obstructions). Accordingly, calibration is treated not as an optional add-on but as a supporting and frequently necessary step to align simulated and measured outcomes and enhance the applicability of the resulting digital models.

The remainder of this section introduces the research problems and gaps (Section 1.2.1) and the aim and objectives (Section 1.2.2).

1.2.1 Problem statement and research gaps

The absence of standardised frameworks for acquiring, processing, and representing required inputs limits scalability and hinders large-scale building performance analyses based on evidence from the existing built environment. This research addresses these challenges by identifying and addressing five key gaps in material characterisation and geometric reconstruction, with the first two related to material characterisation, other two to geometrical reconstruction, and one regarding the calibration of spectral daylight models.

- ***Gap 1****: There is no standardised classification of the refinement in geometrical details necessary for indoor daylight applications.*
  Urban Levels of Detail (LoD) definitions balance reconstruction cost and application needs, and several indoor extensions target other domains (*e.g.*, disaster management, area determination, route visualisation) (Kemec et al., 2012; Boeters et al., 2015; Hagedorn et al., 2009). These do not address indoor daylight requirements, limiting informed decisions during 3D model construction. A fit-for-purpose framework for standardised classification of the refinement in geometrical details would align reconstruction possibilities with data requirements for daylight simulations and support automated pipelines.
- ***Gap 2****: Uncertainty from inaccurate material definitions in daylight modelling is underexplored.*
  Although optical properties strongly influence daylight assessment outcomes, the uncertainty introduced by different measurement techniques or simplifying reality via assumptions remains insufficiently quantified. Quantifying input uncertainty will guide researchers and practitioners in selecting appropriate measurement

techniques and in conducting uncertainty analyses of daylight performance metrics.

- ***Gap 3**: Current techniques for modelling of indoor daylight require extensive manual labour to reconstruct 3D models for daylight applications.*
  As-built daylight models depend on field measurements and reconstruction of main surfaces (walls, ceilings, floors), windows, and furniture. Common practice relies on point-by-point measurement or manual surface modelling from point clouds as raw geometric data (Quek and Jakubiec, 2021), which is time-consuming and labour-intensive, especially in geometrically complex spaces. New methods are needed to automate this step.
- ***Gap 4**: There is no low-cost, automated workflow for characterising opaque surface properties for daylight simulation.*
  Traditional approaches (*e.g.*, albedo via luminance/illuminance readings or reflectance spectrophotometers) require expensive equipment and substantial on-site effort. Consequently, practitioners often select materials from pre-existing datasets, which can introduce mismatches and subjectivity (*e.g.*, in colour selection). Developing automated, accessible alternatives would enable large-scale application and improve modelling accuracy across diverse contexts. Applying computer vision and image processing techniques have been found effective in estimating reflectance and texture directly from photographs on sample scale (Bodart et al., 2008; Jakubiec, 2022; Mardaljevic et al., 2015, 2021; Ferwerda, 2018; Luo et al., 2024; Kavoosighafi et al., 2024). These methods can provide scalable and low-cost alternatives to traditional measurements, enabling material characterisation from imagery collected with consumer-grade cameras.
- ***Gap 5**: Calibration of indoor spectral daylight simulation/ipRGC-influenced light (IIL) is underdeveloped.*
  In contrast to building energy simulation, where calibration practices and error metrics are well-established, the calibration of daylight and spectral irradiance modelling lack a systematic approach. Existing efforts are limited to validating individual tools or tuning multiple parameters in ad hoc ways. Regardless of how accurate the on-site measurements are, uncertainties remain beyond the control of the expert with access to the room, particularly in terms of sun–sky conditions, exterior/context obstructions, and window spectral transmittance. These factors significantly influence the accuracy of simulated spectral irradiance, yet are not consistently accounted for in current calibration practices.

1.2.2 Research Aim and Objectives

Bridging the identified research gaps enables the development of reliable indoor daylight models that can be generated with reduced cost, effort, and time. Accordingly, the overarching aim of this research is to: *Develop and evaluate (semi-)automatic workflows for the creation, characterisation, and calibration of digital indoor daylight models.*

This aim is addressed through five specific research questions:

- **RQ1:** How sensitive are CBDM results to geometric levels of detail?
- **RQ2:** What are the uncertainties caused by inaccurate material definition in CBDM results?
- **RQ3:** How can indoor geometries be efficiently reconstructed to meet the requirements of daylight simulation models?
- **RQ4:** To what extent can image-based material characterisation techniques be applied to simulated indoor daylight models?
- **RQ5:** How can simulated spectral indoor models be calibrated to account for uncertainties in scene reconstruction?

1.3 Outline of this dissertation

This dissertation aims to develop workflows for daylight modelling in existing indoor spaces. To achieve this, the dissertation addresses the five research gaps introduced in Section 1.2.1, which fall into three thematic clusters (see Fig. 1.1): geometrical reconstruction (Gaps 1 and 3), material characterisation (Gaps 2 and 4), and calibration (Gap 5).

The first two chapters explain the importance of daylight modelling and quantify the errors caused by inaccurate input definitions. Chapter 2 addresses Gap 1 by evaluating the sensitivity of CBDM results to different GLoDs. It introduces formalized levels of detail for representing indoor geometry—Geometrical Level of Detail (GLoD)—and assesses how the accuracy of CBDM outcomes changes with changing geometrical levels of detail. Chapter 3 then quantifies the uncertainty in CBDM results caused by inaccuracies in the characterisation of material optical properties. Together, Chapters 2 and 3 establish what degree of alignment between the actual room and the digital model is relevant for daylight-dependent analyses. The actual answer to this question is presumed to be project-dependent—*i.e.* on budget, daylight priority, and application requirements—and a one-to-one correspondence between these discrete levels of representation and specific design applications would require further policy-making and standardisation, which is beyond the scope of this work.

The second set of chapters proposes methods to reduce manual labour and time in preparing daylight models, addressing Gaps 3 and 4. Chapter 4 addresses Gap 3 by developing a semi-automatic workflow for reconstructing the permanent geometry of indoor spaces from point cloud data. Although numerous scan-to-Building Information Modelling (BIM) workflows have been proposed in recent decades, few satisfy daylight simulation requirements—specifically watertightness and inclusion of window boundaries. The proposed method automates this essential step of

generating GLoD0 geometry, which remains invariant to furnishings, while incorporating reduced user input to ensure correctness and completeness of reconstructed window boundaries.

Chapter 5 responds to Gap 4 by validating image-based material characterisation and uplifting techniques for existing indoor spaces. This provides a scalable alternative to expensive on-site measurements and subjective material definitions that are prone to unknown errors. Three image-based techniques and one uplifting technique are validated, and their accuracy and limits are quantified for photopic and spectral daylight simulations.

Finally, Chapter 6 addresses Gap 5 by developing a calibration workflow for indoor spectral daylight simulation. This workflow aligns simulated and measured spectral irradiance, extending the scope of conventional three-channel validation toward spectral and circadian-relevant performance metrics. It addresses uncertainties that are often beyond the daylight expert's budget and access when modelling daylight in indoor spaces.

Chapter 7 concludes the dissertation by summarizing the findings and identifying opportunities for future work.

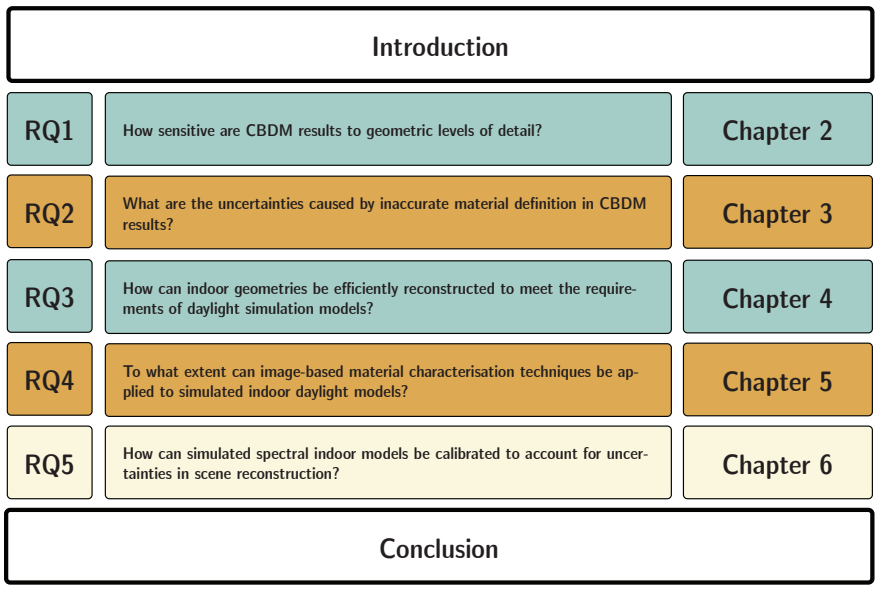

FIG. 1.1 Structure of this dissertation.

Introduction		
RQ1	**How sensitive are CBDM results to geometric levels of detail?**	**Chapter 2**
RQ2	What are the uncertainties caused by inaccurate material definition in CBDM results?	Chapter 3
RQ3	How can indoor geometries be efficiently reconstructed to meet the requirements of daylight simulation models?	Chapter 4
RQ4	To what extent can image-based material characterisation techniques be applied to simulated indoor daylight models?	Chapter 5
RQ5	How can simulated spectral indoor models be calibrated to account for uncertainties in scene reconstruction?	Chapter 6
Conclusion		

2 Sensitivity of CBDM results to Geometrical Levels of Detail

ABSTRACT

This chapter defines Geometrical Level of Detail (GLoD) for indoor daylight simulation and quantifies how the degree of geometry completeness affects climate-based daylight metrics. A semantically agnostic GLoD scheme tailored to interior spaces is introduced: GLoD0 includes only permanent shells (walls, floor, ceiling, windows), while GLoD1–GLoD3 add non-permanent objects by size thresholds derived from the Oriented Bounding Box (OBB) area distribution across nine spaces; GLoD4 contains all objects found in those real spaces. Six case-study rooms are simulated with *Radiance* using a daylight coefficient approach; performance is evaluated with Total Annual Illumination (TAI), spatial Root Mean Squared Error (RMSE), and computation time.

Gradual exclusion of non-permanent objects increases TAI error from GLoD4 as follows: GLoD3 $\approx$ 1.08%, GLoD2 $\approx$ 6.55%, GLoD1 $\approx$ 11.21%, and GLoD0 $\approx$ 18.05% on average across rooms, with higher errors around furniture objects. Errors concentrate around furniture due to local occlusion/reflectance effects, while computation time drops substantially (up to $\sim$3× faster at GLoD0). In practice, GLoD2 (removing objects with OBB$<2.4\,\mathrm{m}^2$) limits average daylight availability error to <10–15% with large speed increase, offering a pragmatic balance for early analyses; higher GLoDs are advisable for detailed design or dense furnishings. The GLoD framework enables application-specific acquisition/reconstruction pipelines—as exemplified in Chapter 4—and provides standardised references to assess (semi-)automatic geometry pipelines for daylight simulation.

This chapter is published as part of the peer-reviewed journal article: Forouzandeh, N., Brembilla, E., Nan, L., Stoter, J., & Jakubiec, A. (2024). *Influence of geometrical levels of detail and inaccurate material optical properties on daylight simulation*. Energy and Buildings, 306, 113924. https://doi.org/10.1016/j.enbuild.2024.113924.

Part of this work is published in the conference paper: Forouzandeh, N., Brembilla, E., Stoter, J., & Nan, L. (2023). *Impact of geometrical resolution on long-term climate-based daylight metrics*. In *Proceedings of Building Simulation 2023: 18th Conference of IBPSA*, pp. 698–704.

A developed and formalized definition of GLoD is currently under review: Forouzandeh, N., Grobe, L., & Brembilla, E. (2025) *Geometrical Levels of Detail for Indoor Daylight Simulation*.

2.1 Introduction

In the early planning phase of a building, many details about the indoor configuration remain undefined. This uncertainty arises from factors like the flexible nature of interior layouts and the evolving needs of clients and future occupants. As a result, constructing an accurate and detailed geometrical model at this stage is inherently challenging. In contrast, after a building is built, acquiring its 3D model becomes a fundamental step for different types of analysis, simulations, or interventions.

In all the building life-cycle stages, and regardless of the desired application of the daylight model, a 3D model with an 'optimal' Levels of Detail (LoD) is necessary. This could refer to (1) the most detailed model available, (2) a balanced 3D data acquisition strategy that aligns reconstruction costs with the intended application, or (3) a combination of both. As it will be described in more detail in Section 2.2, finding this optimal LoDs has been a more urgent problem in the urban data domain, given the importance of efficient representation and, as importantly, the manual acquisition that highly detailed models require. Therefore, researchers in this domain have developed and proposed the concept of Levels of Detail to balance acquisition and reconstruction with the final application.

This work extends the understanding of the impact of Geometrical Levels of Detail (GLoDs) on Climate-based daylight modelling (CBDM) results within indoor spaces. The novelty of this research lies in the proposal of a tailored definition of GLoD specifically designed for indoor daylight applications. This will be later complemented by the introduction of the concept of Material Classes of Precision (MCoPs) in Chapter 3.

2.2 Literature review

The idea of GLoD has been extensively studied and applied in urban-level 3D modelling of buildings to balance the acquisition and reconstruction costs concerning the desired application requirements (Biljecki et al., 2016; Kutzner et al., 2020). Five LoDs are defined in CityGML2.0 as LoD0: 2.5D building footprints and/or roof edge polygons, LoD1: Extruded footprints, LoD2: Simple models with differentiated roof structures and semantically enriched boundary surfaces, LoD3: Detailed architectural models with openings, and LoD4: models with similarly detailed indoor geometries of buildings.

The influence of modelling different LoDs has been investigated in the exterior domain. Sadeghi and Mistrick modelled the exterior geometry in six different LoDs by the inclusion of different semantics based on size at each LoD (Sadeghi and Mistrick, 2022). Biljecki et al. studied the propagation of positional errors in the estimation of the solar irradiation of building roofs based on TU Delft's LoDs jointly with varying XY/Z accuracy levels to realistically model 3D models using different acquisition techniques with varying accuracy levels (Biljecki et al., 2016).

There have been multiple attempts to extend these definitions to the interior domain:

- Kemec et al. define three new LoDs to improve the standard LoDs 1, 2, and 3 for disaster management. This includes LoD1.5 with storeys, LoD2.5 with indoor buildings parts, and LoD3.5 with apartments (Kemec et al., 2012).
- Boeters et al. propose a joint exterior and indoor LoD definition for indoor area determination (Boeters et al., 2015).
- Hogedorn et al. propose four LoDs for indoor navigation, where LoD1 includes building's access points, outer shell, building parts, LoD2 includes various spaces, indoor routes, and 2D floor plans, LoD3 shows space height, shape of doors and windows, and LoD4 includes all interior and exterior details of buildings, at the highest degree of realism (Hagedorn et al., 2009).
- Benner et al. break indoor LoDs into semantic and geometric. They define four indoor LoDs, with LoD0 as the 2D and 2.5D representation, LoD1 as vertical solid extrusion, LoD2 as generalized real geometry, and LoD3 as the exact real geometry (Benner et al., 2013).
- Billen et al. propose three internal LoDs. In their work, LoD1 includes one or more internal PPSS generalized by polyhedra. LoD 2 are all the internal PPSS represented according to some geometric generalization and the openings linking the internal sub-spaces are represented. And LoD3 being identical to level 2 without geometrical generalization and with the addition of openings on the outside (Billen et al., 2012).

Existing definitions in such studies are low in resolution when indoor daylight is the desired analysis. For example, in the CityGML model only in LoD3 do the openings

appear, and in LoD4 indoor objects are included. This makes it impossible to study the impact of indoor geometrical resolution on CBDM results.

To address this, Agarwal et al. introduced LoDs for façade representations (Agarwal et al., 2024) to study the uncertainties associated with different façade representations at the concept-design stage. More specifically for the indoors, Grobe and Jakubiec defined semantic definition of LoDs with the following specifications (Grobe and Jakubiec, 2023):

- LoD4 The detailed model including furniture and shading devices, with measured reflection properties. Such LoD is typically possible only in a post-occupancy study.
- LoD3 as LoD4 without furnishing and a low wall reflectance of 0.20 to compensate for that. This information is expected to be available in an advanced planning phase.
- As LoD4 but without furnishing, with original wall reflectance and shading.
- As LoD2 but without any shading devices, reflecting LoD at earlier planning phases.

However, currently there is no semantically agnostic geometric definition of indoor LoDs. This definition can be particularly helpful when the indoor model is not semantically labelled and enriched. To address this, a GLoD framework is defined in this chapter to better study the influence of geometry completeness on daylight availability calculations without the need for semantic information.

GLoD and LoD are not completely distinct concepts. In the context of this dissertation, GLoD is used to refer to the concept that is missing in daylight literature and the definition that is developed in this research to address that. This is to prevent confusion with other definitions of LoD that might also account for topological, semantic, or other types of information.

2.3 Data and Methods

2.3.1 Geometrical Level of Detail (GLoD)

In this work five GLoDs are defined by size-wise inclusion of non-permanent indoor objects. GLoD0 contains only the permanent objects, i.e., walls, windows, floor, and ceilings. These objects are the elements crucial for any type of indoor daylight simulation. In this framework, the most complete GLoD is the GLoD4, which contains all the indoor objects regardless of size and mobility. Three in-between GLoDs are

defined by including objects greater than certain thresholds. These thresholds are determined as the surface area of Oriented Bounding Box (OBB) corresponding to the 25^{th}, 50^{th}, and 75^{th} percentiles of the cumulative distribution of the non-permanent indoor objects across all of the case-study spaces.

An OBB represents the smallest rectangular box that completely encompasses an object while allowing for arbitrary rotations in three-dimensional space. Unlike an Axis-aligned Bounding Box (AABB), which is fixed to the coordinate axes, an OBB can be rotated to match the orientation of the object it encloses. OBB area was chosen instead of its volume because, in the input geometrical data, some of the indoor objects like desk surfaces are modelled as single surfaces instead of three-dimensional volumes. While the volume for these objects is zero, they influence the daylight results and thus should be represented with a non-zero value. This measure is chosen for both its relative accuracy and generalisability. An example of four different bounding geometries in 2-dimensional space is shown in Fig.2.1.

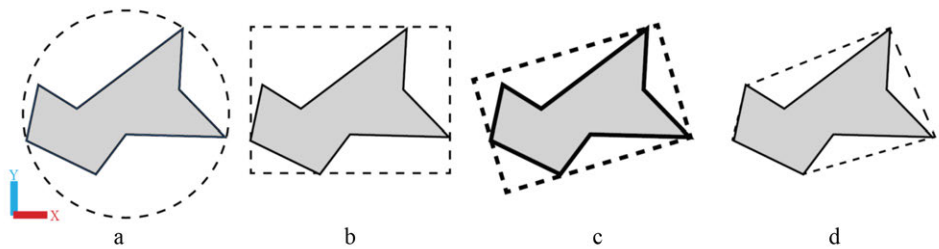

FIG. 2.1 Bounding geometries. From left to right: (a) Surrounding Sphere, (b) Axis-aligned bounding box, (c) OBB, and (d) Convex hull.

A statistical summary of object sizes in the case study spaces is presented in Fig. 2.2. According to this data, the threshold OBB area values for the in-between GLoD1, GLoD2, and GLoD3 are 3.0, 2.4, and $0.5\,\mathrm{m}^2$, respectively. This means that, for instance, an object with OBB size of $2.2\,\mathrm{m}^2$, appears in GLoDs 3 and 4, but not in 2, 1, and 0.

2.3.2 Case study spaces and input preparation

Six teaching and office spaces are included in this study. The general information and the 3D representation of the spaces are presented in Table 2.1 and Table 2.2, respectively. The spaces are sampled from common university spaces with varying sizes in two different geographical locations. Geometrical information was acquired using multiple Light Detection and Ranging (LiDAR) scans for each scene, followed by the registration of all scans and the manual reconstruction of surface models for each space.

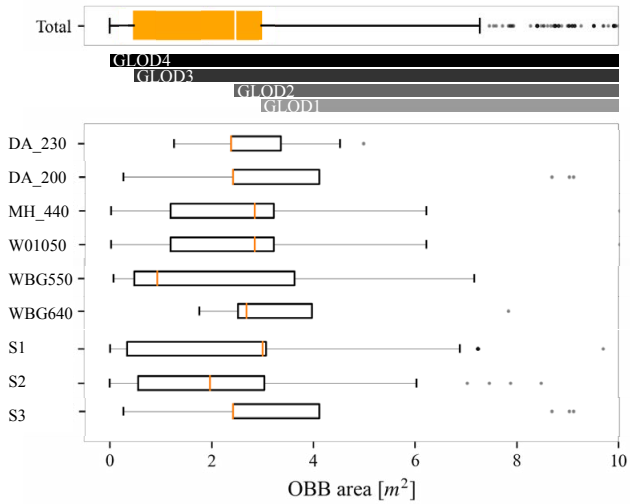

FIG. 2.2 Summary of object sizes in the case study spaces.

TABLE 2.1 Descriptions of the case study rooms.

Space ID	Location	Space type	Dimensions [m*m*m]	Window-to-Floor Ratio (WFR) [%]	Manual surface model	Registered 3D scan	Material spectral measurement
WBG550	Delft, NL	Open office	12×9.8×5.8	29.4	Yes	Yes	No
W01050	Delft, NL	Meeting room	5.8×4.4×5.8	9.1	Yes	Yes	No
WBG640	Delft, NL	Meeting room	7.2×3.4×2.6	40.9	Yes	Yes	Yes
DA_200	Toronto, CA	Classroom	16.6×10.6×3.5-6.7	9.1	Yes	Yes	Yes
DA_230	Toronto, CA	Classroom	14.5×9.7×3	9.6	Yes	Yes	Yes
MH_440	Toronto, CA	Classroom	11.7×8.3×4.0	14.1	Yes	Yes	Yes

To increase the generalisability of this geometrical definition, three additional interior spaces are included in the case study spaces that are only used for GLoD definition. These spaces are introduced in Table 2.3 and Fig. 2.3. These spaces are reused from another study done by Queck and Jakubiec on the calibration and validation of climate-based daylighting models based on one-time field measurement (Quek and Jakubiec, 2021).

TABLE 2.2 Case study Rooms – 3D representation.

WBG550	W01050	WBG640
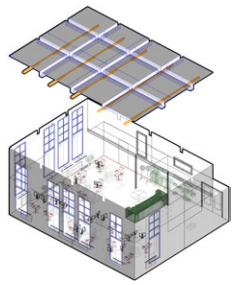	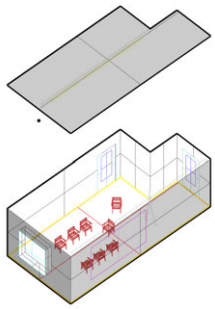	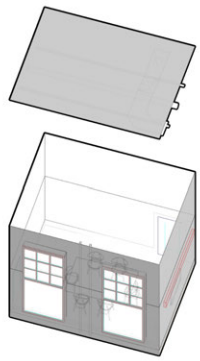
DA_200	**DA_230**	**MH_440**
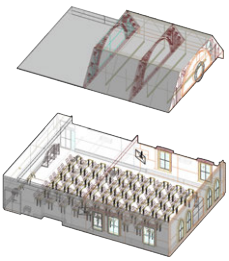	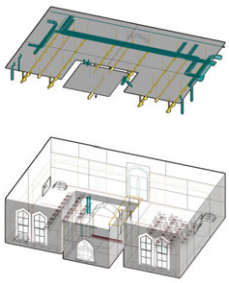	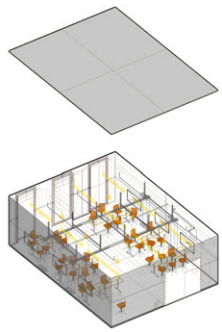

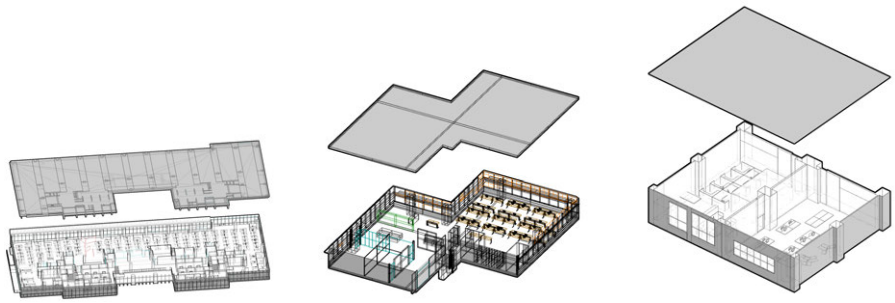

1 *S1* 2 *S2* 3 *S3*

FIG. 2.3 Additional case study spaces for GLoD definition – 3D views.

TABLE 2.3 Additional case study spaces for GLoD definition—general information.

Space ID	Location	Space type	Dimensions [m]	WFR [%]
S1	Singapore, SG	Open office	$35 \times 94 \times 4.5$	10.6
S2	Singapore, SG	Open office	$26 \times 30 \times 3.3$	33.1
S3	Singapore, SG	Open office	$20.9 \times 15.7 \times 4.7$	8.6

2.3.3 Simulation setup

Radiance was used to conduct the indoor annual daylight simulation (Larson and Shakespeare, 1998). *Radiance* is a physically-based rendering system that is implemented in several building daylight simulation tools and is validated against measurements in many empirical studies (Geisler-Moroder et al., 2016; McNeil et al., 2013). In a validation study done by Mardaljevic it is shown that *Radiance* predictions have a mean relative error of 5.6% with a standard deviation of 3.4% (Mardaljevic, 1995)). Dynamic Daylight Simulation (DDS) was used, which is based on the daylight coefficient method and consists of the following steps (Subramaniam, 2017)):

1. Performing annual daylight coefficient simulation ($C_{dc}S$).
2. Performing annual direct-only daylight coefficients simulation ($C_{dcd}S_d$).
3. Performing annual sun-coefficients simulation ($C_{sun}S_{sun}$).
4. Combining the results using the Eq. 2.1 to calculate the illuminance matrix (E).

$$E = C_{dc}S - C_{dcd}S_d + C_{sun}S_{sun} \tag{2.1}$$

Total Annual Illumination (TAI) was calculated as the performance indicator for each run as shown in Eq. 2.2 . This is calculated as the average illuminance value across the space throughout the occupied times in the entire simulation year. The occupancy hours are assumed between 9:00 and 17:00. Eq. 2.2 shows how TAI is calculated.

$$TAI = \frac{1}{1000 * G} \sum_{i=1}^{G} \sum_{j=1}^{H} (E_{ij}) \tag{2.2}$$

Where:

TAI Total Annual Illumination in klx.hour/year

E_{ij} Illuminance value at point i at time step j

G Number of grid points

H Number of simulation hours

These calculations were conducted on DelftBlue (Delft High Performance Computing Centre DHPC, 2024). Each annual computation iteration was performed on a single CPU with 12GB of memory.

2.3.4 Error calculation

The model evaluation uses three metrics, namely Percentage Error (PE), Root Mean Squared Error (RMSE), and simulation time. PE and RMSE are defined in Appendix A.

2.4 Results

2.4.1 Definition of GLoDs

The 3D representation of three example spaces in multiple GLoDs is shown in Fig. 2.4. Some semantic elements first appear in different GLoD across different interior spaces. This is because of the variation in the size of instances within that semantic. For instance, chairs appear first in GLoD3 for space *W01050* and *DA_230*, but in *MH_440* and *WBG640* they appear in GLoD2. This is because their OBB sizes in these spaces are slightly larger than the former ones. A general pattern can be derived from the analysis of the nine indoor spaces included in this study, revealing the common semantic features found in each GLoD. This is illustrated in Fig. 2.5.

2.4.2 Influence of varying GLoDs

Effects of varying GLoDs are shown in terms of PE and RMSE in Fig. 2.6 and Fig. 2.7, respectively. According to these results, on average, gradual exclusion of non-permanent objects in GLoD3 to GLoD0 results in 1.08, 6.55, 11.21, and 18.05 % errors in the final TAI, respectively. The influence of geometrical resolution on annual daylight results is summarized in Table 2.4. Moreover, the spatial distribution of errors is plotted in Fig. 2.8. It shows that the results grid points around the furniture pieces have the highest deviations from the ground truth with varying GLoDs. This can only be due to the effective obstruction of the daylight falling onto the adjacent

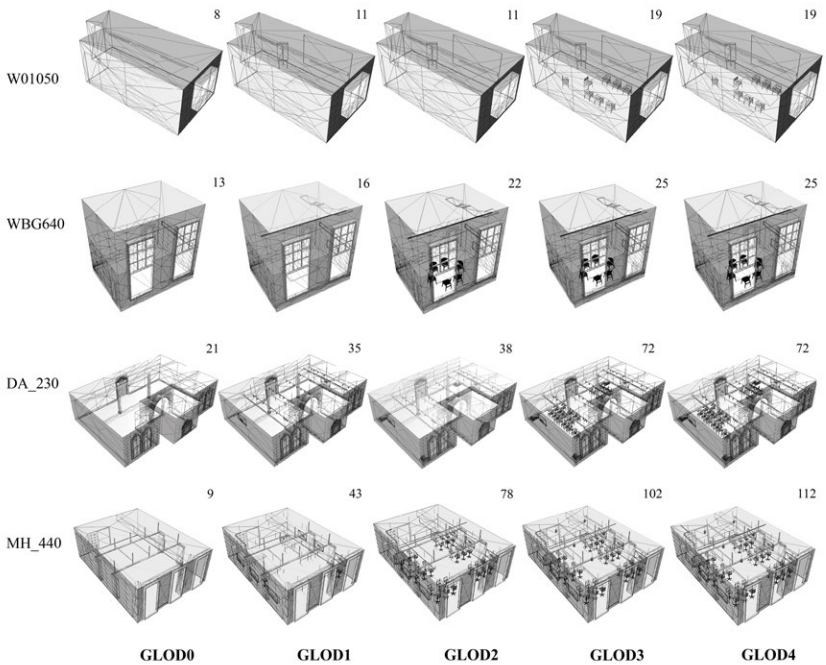

FIG. 2.4 3D representation of spaces in multiple GLoDs. The number of objects is indicated above each GLoD.

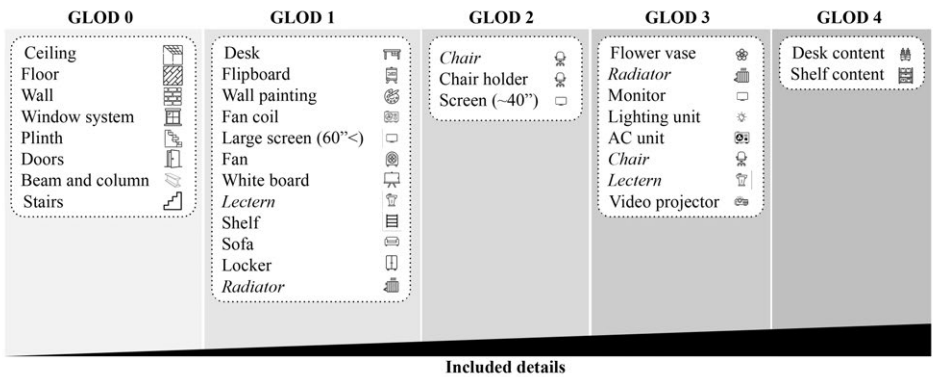

FIG. 2.5 The GLoD where each semantic first appears in the models. Some of the semantics appear in different GLoDs for the first time, which are indicated in *italics*.

grid points and not because the grid points fall within the objects, since those points were excluded from the grid points by intention.

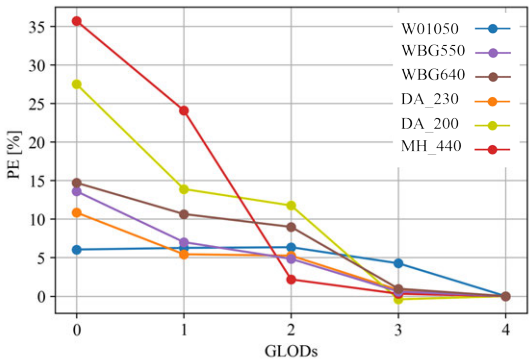

FIG. 2.6 Influence of geometrical resolution on annual illuminance predictions (PE [%])

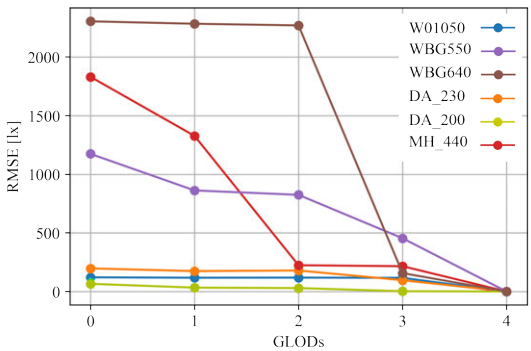

FIG. 2.7 Influence of geometrical resolution on annual illuminance predictions (RMSE [lx]).

The errors correlate with the number of removed furniture pieces. The highest error happens in *DA_200* and *MH_440* with 27% and 36% respectively. This is due to the relatively higher furniture density in these spaces. The least errors are seen in *W01050* and *DA_230* with 7% and 11% respectively. An average error of 18% was observed across the six datasets when non-permanent objects were completely removed from the model. This mean error is less than 5% in GLoD3 when desk and shelf content are not included in the model. In GLoD2, the errors are on average less than 10%. In these models, indoor objects including flower boxes, small radiators, monitors, lighting fixtures, AC units, chairs, lecterns, and video projectors are excluded along with desk and shelf content. The resulting mean error in GLoD1 is around 15%. A steep increase in error can be seen in this step in space *MH_440*, which is possibly due to the high density of chairs that are removed in this GLoD (see Fig.2.6). A similar slope is seen in GLoD2 for space *DA_200*, where chairs are removed, and in GLoD0 where a high number of desks are removed from the model.

The impact of geometrical resolution on computation time was also measured. As shown in Fig. 2.9, an increase in calculation time is evident across all the case study

TABLE 2.4 Influence of geometrical resolution on annual daylight results - RMSE and PE.

	GLoD0	GLoD1	GLoD2	GLoD3
		PE $[\%]$		
min	6.04	5.42	2.16	0
max	35.67	24.07	11.75	4.25
mean	18.05	11.21	6.55	1.08
		RMSE $[lx]$		
min	57	894	50	44
max	949	51	876	841
mean	320	302	292	279

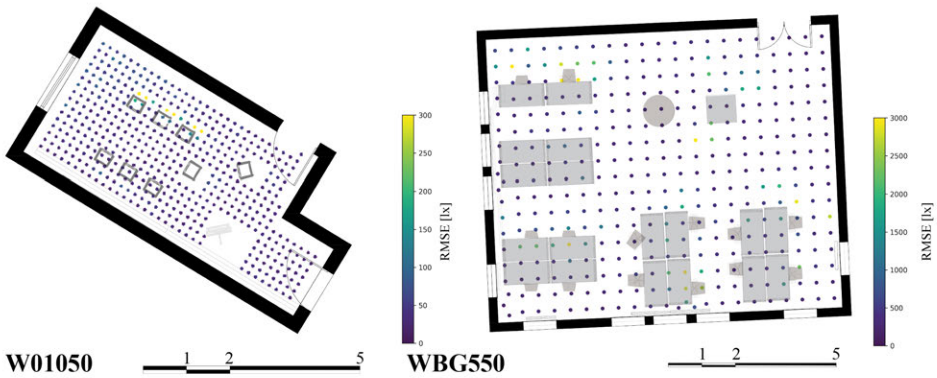

FIG. 2.8 Influence of geometrical resolution on annual daylight results - GLoD0 and GLoD4

spaces. Simulation time is a function of complexity in the model which is partly due to the number of non-permanent objects included and partly due to the complexity of the object mesh. In all the spaces a decrease can be seen in the simulation time when this complexity is decreased. Between 25% (in *W01050*) and around 200% (in *DA_200*, *WBG550*, and *WBG640*) was seen in the change in simulation time. Two different slope patterns can be seen here, firstly those of *DA_200* and *WBG550*, with a high slope on GLoD3, and that of the rest. This again can be attributed to the discrepancy in complexity of the models among the two groups.

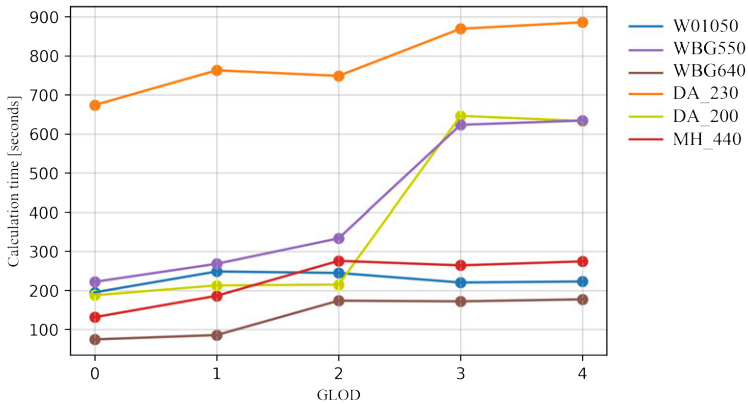

FIG. 2.9 Influence of geometrical resolution on simulation time

2.5 Discussion

During the post-occupancy phase of a building's life cycle, the fundamental structures of the space, such as walls, windows, ceilings, and floors, remain unchanged, while non-permanent objects can be modified as needed. Therefore, the focus in this study was on these non-permanent objects when defining the Geometrical Levels of Detail (GLoDs) in geometry. This may also provide insights into the impact of the geometry of permanent objects. The GLoD definition was based on data-driven size thresholds, determining which objects to include or exclude. The results indicate that GLoD2 models result in less than 15% error in daylight availability simulations. This suggests that removing objects with an OBB size smaller than 2.4 m^2 will have a minimal negative impact on the CBDM results. Such objects may include desks, shelf contents, Air Conditioning (AC) units, certain chairs and lecterns, small radiators and flower boxes, and video projectors (refer to Fig. 2.5).

There are mainly two ways of defining GLoDs, one being the gradual inclusion of non-permanent objects, and the other being a reduction of geometrical complexity using mesh simplification techniques such as reduction, collapsing, or amalgamation. In this study, the former approach is followed since it is more probable to be chosen by practitioners. However, mesh complexity is likely the reason why no correlation can be observed between TAI PE and the drop in the simulation times (see Fig.2.7, Fig.2.6, and Fig. 2.9).

The OBB size of the non-permanent objects was chosen as the primary basis for the definition of the GLoDs in this study. This quantity was used as a criterion to gradually remove objects from the 3D scene and calculate the errors that resulted from this incomplete model. The fundamental motivation for employing this value

was that it could be applied to other geometrical data, including point clouds of objects that exhibit excessive geometric details. It is a constrained definition, though, as it ignores factors like object orientation and proximity to windows. It is observed that objects of the same semantics appear in multiple GLoDs because of variation in object sized of the same semantics. An improved GLoD framework may include both size and semantics for a higher robustness.

The definition of GLoDs in this study is uni-dimensional, *i.e.* only based on the Oriented Bounding Box (OBB) size of the non-permanent objects. This definition could be more complete if other descriptors of the objects, *e.g.* their semantic information were considered. Moreover, only non-permanent objects are considered for defining discretized GLoDs, and the accuracy in modelling the main structures of the space, *e.g.*, walls, floors, ceilings and more importantly windows is not studied.

2.6 Conclusion

In this study, the influence of incomplete geometrical modelling on annual daylight predictions is quantified. Geometrical Level of Detail (GLoD) was defined for this study, derived from measurements of in-use university and office spaces.

Exclusion of non-permanent objects in GLoD3-GLoD0 causes on average 1.08, 6.55, 11.21, and 18.05 % errors in the output TAI values respectively. The errors are highest around the location of non-permanent objects in the room. Excluding the non-permanent objects is shown to make the simulation run up to threefold faster.

The results of this study are useful for evaluating novel methods of geometrical reconstruction in daylight simulation, because they give insights into the potential propagation of errors caused by (semi-)automatic geometrical reconstruction.

Proper GLoD can be determined according to the available acquisition and computational resources and the acceptable accuracy for a particular application. This research lays the groundwork for a quantitative assessment of potential errors for novel geometrical reconstruction methods. In general, for coarse daylight assessments of buildings, such as at a regional or urban level, lower GLoDs could be deemed acceptable. However, for specific indoor design decision-making problems, higher GLoDs will result in more reliable solutions.

In future studies, it is essential to continue exploring and refining automation in these processes to enhance the efficiency and accuracy of daylight simulations using digital building models.

Introduction		
RQ1	How sensitive are CBDM results to geometric levels of detail?	Chapter 2
RQ2	**What are the uncertainties caused by inaccurate material definition in CBDM results?**	**Chapter 3**
RQ3	How can indoor geometries be efficiently reconstructed to meet the requirements of daylight simulation models?	Chapter 4
RQ4	To what extent can image-based material characterisation techniques be applied to simulated indoor daylight models?	Chapter 5
RQ5	How can simulated spectral indoor models be calibrated to account for uncertainties in scene reconstruction?	Chapter 6
Conclusion		

3 Sensitivity of CBDM Results to Material Classes of Precision

ABSTRACT

This chapter develops a standardised definition of of Material Class of Precision (MCoP)[1] and quantifies how uncertainty in characterisation of optical properties propagates to annual daylight metrics. Based on 106 paired measurements (Average Hemispherical Reflectance (AHR) versus spectrophotometer) of opaque materials, error distribution statistics are derived and four MCoPs (normal distributions with $\sigma \in [0.05, 0.20]$) are defined applicable to opaque and, by extension, to transparent materials. MCoPs are combined with five geometric Geometrical Levels of Detail (GLoDs) to run Monte Carlo CBDM across six rooms to quantify the combined errors caused by inaccurate material definition and incomplete geometry reconstruction.

Results show that (i) output error distributions are symmetrical but generally non-normal, which indicates a non-linear transformation of input uncertainty; (ii) uncertainty in Total Annual Illumination (TAI) grows approximately linearly with MCoP in all spaces and GLoDs; (iii) for the most complete geometry (GLoD4), median uncertainty spans ∼10–35% depending on space (∼10–30% in most rooms; 5–15% in one case with high Window-to-wall Ratio (WWR)); (iv) spatial error concentrates near glazing, which identifies window transmittance as the dominant contributor to uncertainties, compared to surface reflectance.

This chapter is published as part of the peer-reviewed journal article: Forouzandeh, N., Brembilla, E., Nan, L., Stoter, J., & Jakubiec, A. (2024). *Influence of geometrical levels of detail and inaccurate material optical*

[1] In the publication derived from this and the preceding chapter, the input material uncertainty model was referred to as material classes of accuracy. With growing insight, the term MCoP was adopted instead as it better describes the random uncertainty concept used in this chapter.

properties on daylight simulation. Energy and Buildings, 306, 113924. https://doi.org/10.1016/j.enbuild.2024.113924.

3.1 Introduction

Regardless of the final application, daylight simulation models involve uncertainties due to inaccurate definitions of different model components including end-user interactions with building elements (Lee et al., 2012), the sky model, geometry, and material optical properties (Kunwar et al., 2021). As more aspects of building design and operation rely on virtual models, the robustness and reliability of such models become an essential requirement.

In Chapter 2 the influence of geometrical modelling on Climate-based daylight modelling (CBDM) was studied. Material optical characterisation is another key element when (re)constructing a 3D model for daylight assessments. Only after characterising the material properties, one can build a valid daylight representation of indoor spaces. Therefore, analysing either geometry or material properties in isolation provides an incomplete understanding.

The development of Geometrical Levels of Detail (GLoDs) enabled the conduct of the Sensitivity Analysis (SA) in the previous chapter. Introducing a similar framework for material properties can help quantify the impact of their inaccurate definitions. This chapter focuses on developing and applying such a framework.

3.2 Literature review

A material definition in computer graphics describes how a material redirects light as a function of wavelength, direction, and position. For daylight availability and glare assessments, since only visible (il)luminance at various points in the room is considered, indoor material properties are typically simplified as an averaged visible albedo. This approach overlooks both the directionality and spectral properties of surfaces.

Brembilla et al. investigated the sensitivity of CBDM results to the reflectance of different semantics, *e.g.*, walls and floors (Brembilla et al., 2018). They implemented the method of Morris to rank the influence of each element relative to the others and evaluated the non-linear effect associated with each. According to Pang et al. in their review on sensitivity analysis in the building performance field Pang et al. (2020), this is the only SA study focused on daylight availability metrics.

The Non-image forming (NIF) influences of daylight, however, have been studied more extensively. Bellia et al. studied the influence of different combinations of wall colour and lighting Correlated Colour Temperature (CCT) on the five human photoreceptor responses (Bellia et al., 2017). In another study, Fani et al. examined the impact of interior design parameters, such as wall colour and desk arrangement, on the circadian lighting conditions of a conceptual design studio in two different locations. These are some examples of studies examining the influence of indoor element colours on occupants NIF responses (Potočnik and Košir, 2020; Hartman et al., 2014; Küller et al., 2006; Köse et al., 2022).

Although albedo is a more compact material representation and therefore computationally simpler, there are fewer studies that quantify its impact on daylight availability metrics. Besides, there are no studies that focus on formalizing the representation of the materials for daylight availability. This chapter aims to address these gaps.

3.3 Data and methods

3.3.1 Case study spaces

DA_230, *DA_200*, *MH_440*, *W01050*, *WBG550*, and *WBG640* are included in this study as described in Section 2.3.2.

3.3.2 Material Class of Precision (MCoP)

There are several material characterisation techniques used in daylight modelling practice. The most accurate one is the use of reflectance spectrophotometers. This method is not always feasible due to high instrument costs, leaving practitioners with other less accurate techniques for characterisation, including luminance-illuminance

reads, known as Average Hemispherical Reflectance (AHR), printed colour charts, and suggested properties based on standards (CEN, 2018). As for the transmittance of transparent materials, manufacturers typically provide designers with optical properties. However, a maintenance factor should be considered, as the actual transmittance can significantly deviate from the manufacturer's suggested value. This deviation is context- and configuration-dependent (CIBSE, 1999). Thus, an onsite measurement is suggested for accurate analysis.

To quantify the uncertainty associated with common measurement methods, a total of 106 building materials were measured using both AHR and a reflectance spectrophotometer as ground truth. The AHR measurements were carried out using a Konica Minolta T-10A illuminance meter and a Konica Minolta LS-150 luminance meter. The ground truth measurements are done using a Konica Minolta CM-2600d reflectance spectrophotometer. Typical indoor materials, *e.g.*, walls, floors, and interior furniture are included in these measurements under natural or electric lighting conditions.

A normal distribution was fitted to the results of the measurement errors. Based on that, four different Material Classes of Precision (MCoPs) are defined as incremental standard deviations. This was done so that the results of the study are generalisable to other material characterisation techniques.

The AHR measurement errors are plotted in Fig. 3.1. The errors are normally distributed with a standard deviation of 0.18 and a mean of 0.1. Reflectance and transmittance information were chosen as the key material optical properties for uncertainty quantification. Specifically, four material classes of precision were defined as normal distributions with four spreads, represented by different standard deviations, from 0.05 to 0.2 as shown in Fig. 3.2. These four accuracy levels were selected to make the results of this study generalisable to any future approaches and scenarios with common optical properties of opaque and transparent surfaces.

3.3.3 Monte Carlo simulation

For each space, five different GLoD as described in Section 2.3.1 and four MCoPs as defined in Section 3.3.2 were generated. This results in a matrix of 20 models with different levels of material and geometrical detail and accuracy.

For each of the cells in the GLoD-MCoP matrix, a Monte Carlo experiment was run. This type of experiment includes a number of iterations with randomised material properties from a given distribution, *i.e.* the MCoPs. This allows for a numerical imitation of the stochastic nature of inaccuracies associated with an on-site characterisation techniques. Each experiment included 500 iterations. The number of simulations was determined based on a convergence test. For this Percentage Error (PE) was calculated for each run compared to the results corresponding to the

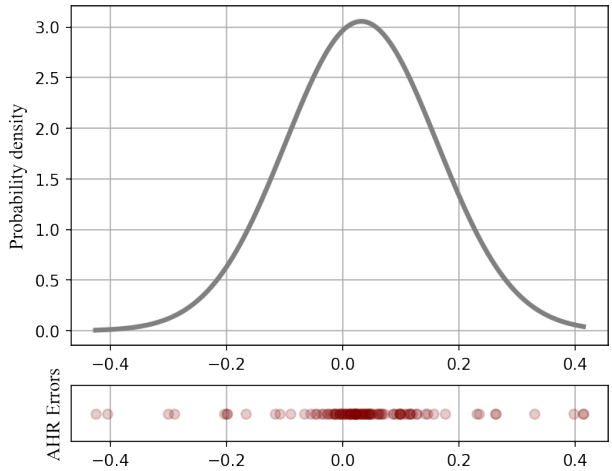

FIG. 3.1 Bell curve fitted to AHR errors compared against measurements from a reflectance spectrophotometer.

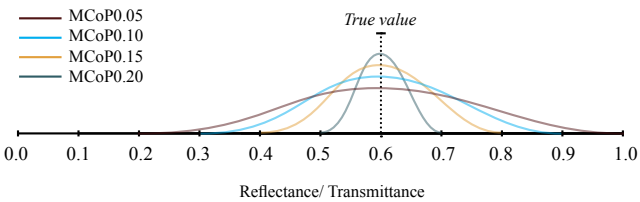

FIG. 3.2 An example of four MCoPs used in the Monte Carlo simulation. In this example the ground truth is 0.6.

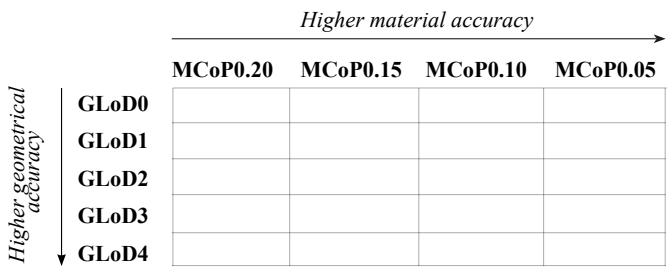

FIG. 3.3 The GLoD-MCoP matrix.

model with error-free material properties. A normal distribution was then fitted to all the simulated cases. After each new run, the goodness of fit was tested using the Kolmogorov-Smirnov method and logged (Stephens, 1974). It is observed that the

goodness of fit converged to the range of 0.50-0.52 for *WBG640* (MCoP0.2, GLoD4) after 500 simulations as depicted in Fig. 3.5. This space was selected because of its small size, resulting in a lower computation load. The choice of MCoP and GLoD was done such that the highest complexity and input variability are accounted for in this experiment. The same number was used for other spaces, GLoDs, and MCoPs.

In total, 10000 iterations were run for each case study, with 500 for each of the cells in the GLoD-MCoP matrix (Fig. 3.3), summing up to 60000 for all the spaces. The normality of the error distributions was tested with D'Agostino and Pearson's normality test, which combines skewness and kurtosis to produce an omnibus test (D'agostino and Pearson, 1973). The overall workflow is depicted in Fig. 3.4.

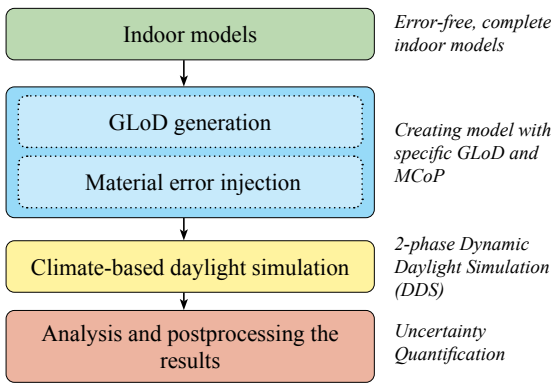

FIG. 3.4 Workflow of the uncertainty quantification study.

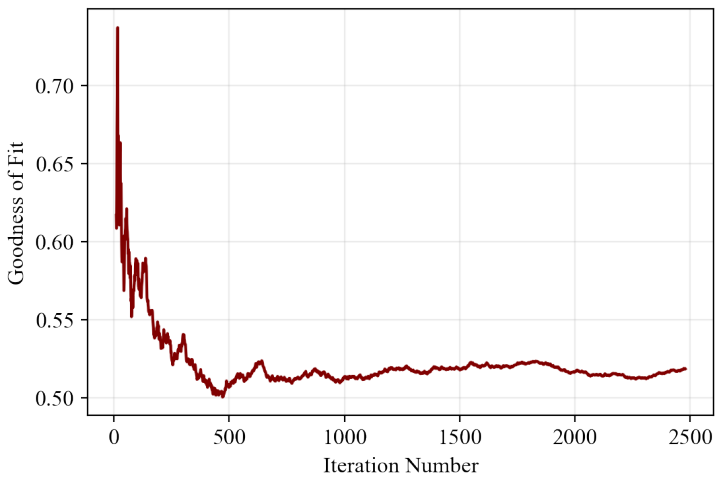

FIG. 3.5 Convergence experiment to determine the sufficient number of simulations — for room *WBG640* (MCoP0.2, GLoD4)). 500 simulations is considered sufficient.

3.3.4 Simulation setup

The CBDM simulations are done and the annual Total Annual Illumination (TAI) metric is calculated are done as described earlier in Section 2.3.3.

3.3.5 Error calculation and uncertainty measures

The following quantities were computed as errors, and the corresponding equations are stated in Appendix A.

- PE for TAI. This quantity is used for convergence study and determining the sufficient number of Monte Carlo simulations (Section 3.3.3). Moreover, it was used to study the distribution of the uncertainties in Section 3.4.2.
- Mean Absolute Percentage Error (MAPE) for TAI. This is used for quantifying the influence of MCoP uncertainty in Fig. 3.9 as calculated in Eq. A.2.
- Root Mean Squared Error (RMSE) of the time-series annual simulation data averaged across the simulation results for each GLoD-MCoP combination. This measure was used for studying the linearity of uncertainty when MCoP varies (Section 3.4.2), to quantify the influence of varying GLoD (Section 2.4.2), the spatial distribution of the uncertainties (Fig. 3.10), and for isolation of error caused by transmittance and reflectance (Fig. 3.11).

3.4 Results

3.4.1 Annual simulation results

Annual simulation results for the six indoor case study spaces are summarised in Fig. 3.6. The results from the model with the most accurate material definition (MCoP0) and the most complete GLoD (GLoD4), median TAI ranges from 50 in *DA_200* to 1100 klx. hour/year in *WBG550*. This is due to differences in orientation and WFR. In *DA_200*, the WFR is 9.5 % and windows are mostly oriented towards the North, while in *WBG550*, the WFR is 29.4 % and the windows are oriented towards the South and West. TAI values in other spaces fall within the results values in the spaces mentioned above.

The distribution of the results appears symmetrical across all space variations with aligned medians within each space when varying MCoP. Thus, the median TAI does not vary noticeably. Moreover, the spread of the TAI results increases consistently by an increase in uncertainty in the definitions of material in spaces.

Besides TAI, Useful Daylight Illuminance (UDI) with 300-3000 lx thresholds (well-lit) was calculated for all grid points within each space. This is visualized in Fig. 3.7. According to this figure, higher daylight availability occurs in the grid points that are closer to the windows. In *WBG550* and *WBG640* those points receive higher levels of light than 3000 lx for the most portion of the occupancy hours. This is why these points are depicted in darker colours in these two case studies.

3.4.2 Influence of varying MCoPs

Fig. 3.8 shows the distribution of simulation errors, as defined in Eq. A.1, for *DA_200* under GLoD4 and four different MCoPs. While the error distributions appear symmetric, they generally do not match the input reflectance distributions. According to the normality test results (see Appendix B), the majority of these output distributions deviate from normality. This indicates that the simulation process introduces non-linear transformations, meaning that even normally distributed input uncertainties do not necessarily result in normally distributed output errors.

Fig. 3.9 shows the uncertainties as calculated in Eq. A.2 in all the six study spaces and GLoDs. The benchmark GLoD is GLoD4 for this error calculation. In the most complete model (GLoD4) in *W01050*, *DA_230*, and *DA_200* the uncertainty ranges from 10% in MCoP0.05 to 35% in MCoP0.2. This range is slightly narrower in *WBG550* and *WBG640* (10%-30%). In contrast, in MCoP0.05 to MCoP0.2, the range extends from 8% to 30%. In *MH_440*, a different trend is observed and the errors range from 5% for MCoP0.05 to 15% in MCoP0.2. The only difference in the geometry in this space is the presence of high windows, although in WFR terms the values are average (see Table 2.1).

Generally, the uncertainty in predicting the annual daylight simulation results increases linearly with material uncertainty across all spaces and GLoDs. This was also observed in Fig. 3.6.

Fig. 3.10 shows a spatial analysis of the errors, from which it can be seen that the illuminance estimation uncertainty is larger around the glazing. This suggests the hypothesis that uncertainties in defining transmittance contribute significantly more to overall errors than uncertainties in reflectance.

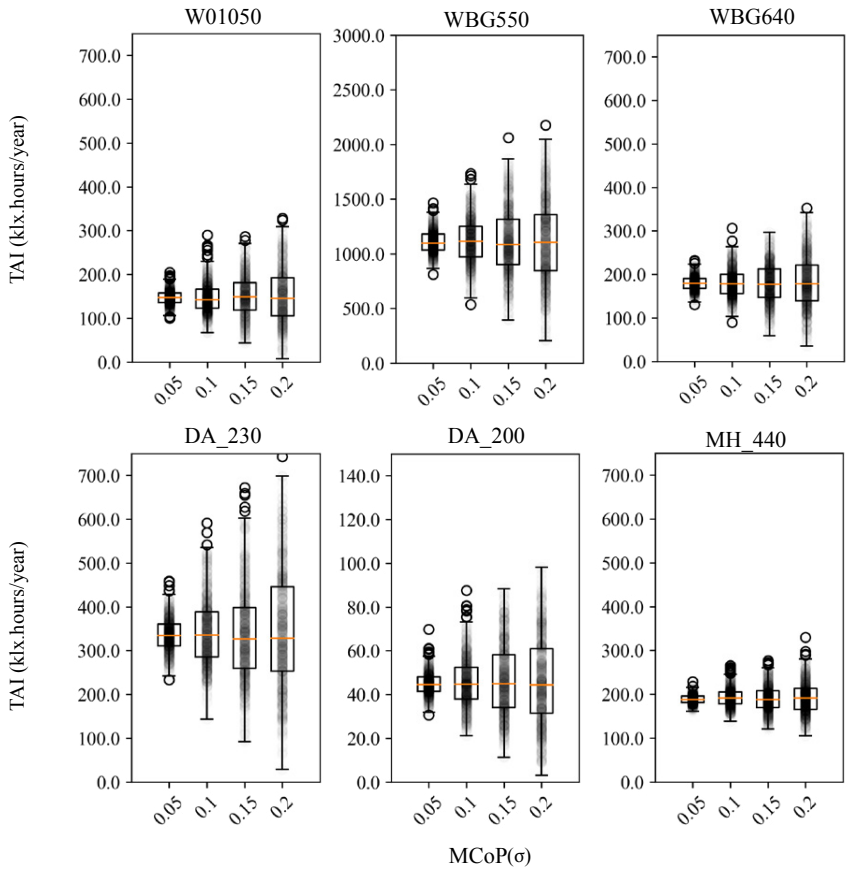

FIG. 3.6 TAI results for GLoD4. Box plots show the inter-quartile ranges for each GLoD-MCoP combination. The highest and lowest 5 percentiles are considered and visualized as outliers. Note that the scales in the y-axis differ for *DA_200* and *WBG550* for better readability.

3.5 Discussion

The optical properties of materials were defined as a randomly picked value from a normal distribution centred around the ground truth. Four different distributions were used to represent four classes of material accuracy (MCoP). This definition is based on 106 measurements of opaque materials using the AHR technique. Other common techniques for characterising opaque materials, for example, using reflectance spectrophotometer, illuminance-proxy (Forouzandeh Shahraki et al., 2022; Mardaljevic et al., 2015), and Chartered Institution of Building Services Engineers (CIBSE) colour charts are assumed to fall within comparable ranges. The

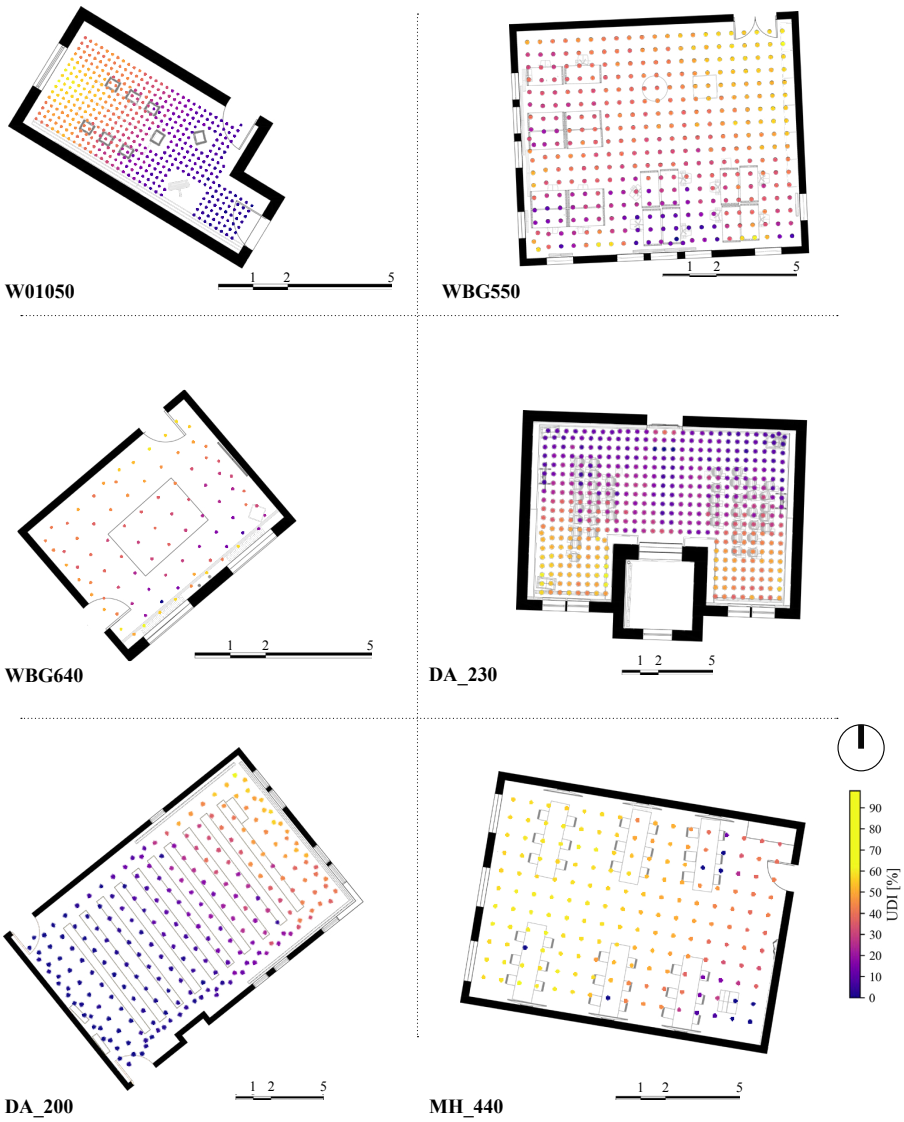

FIG. 3.7 UDI maps for the six spaces. The considered UDI range is 300-3000 lx.

distribution shape of the errors in the outputs did not fully match that of the inputs. According to the normality test, it was not normal, although symmetrical.

The results obtained for these opaque surfaces were generalised to transparent

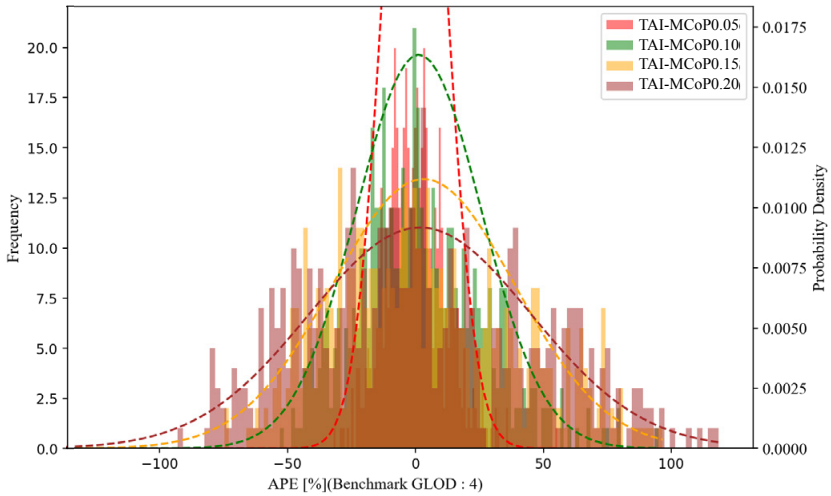

FIG. 3.8 Distribution of errors in the estimation of the TAI for space DA_200 with the four different MCoP and the fitted normal probability density functions for each one (*DA_200*).

materials. The optical properties of transparent materials are commonly characterised by manufacturers' data. However, depending on the context of the building, it is necessary to apply a maintenance factor to the nominal transmittance information (CIBSE, 1999). Since the data on the transparent materials and the potential inaccuracies caused by different characterisation methods and incorrectly assumed maintenance factors were limited, the material definition of the opaque surfaces were consistently applied to transparent ones. In reality, the characterisation of transparent and opaque materials is typically done using independent methods. If similar measured databases were accessible, it would allow for better modelling of precision classes for transparent materials.

The spatial distribution of the uncertainties suggested a dominant importance of defining transmittance compared to reflectance. This was supported in two more spaces but not in the third one, *i.e. MH_440*. This space has higher windows compared to other spaces, although the WFR is average. This difference cannot be attributed to material properties, since the ground truth reflectance and transmittance values for similar semantics (*e.g.* walls, windows) are defined equally in all spaces.

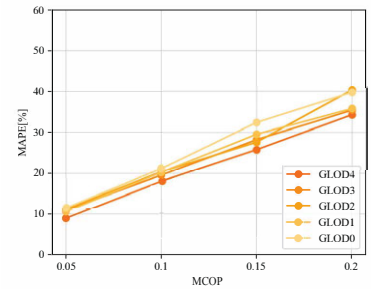

1 *W01050*

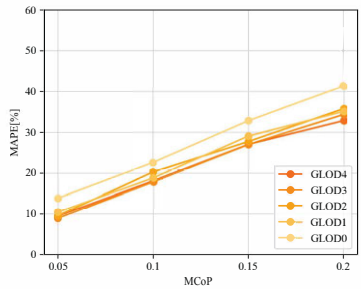

2 *DA_230*

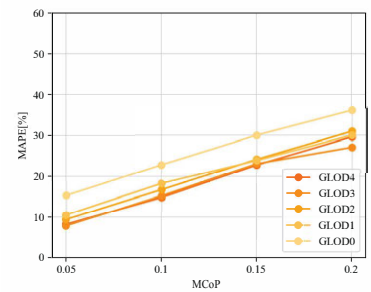

3 *WBG550*

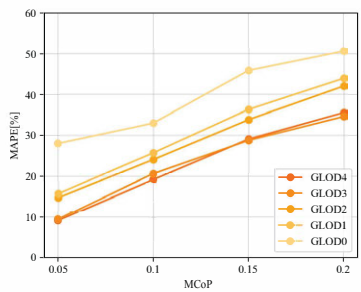

4 *DA_200*

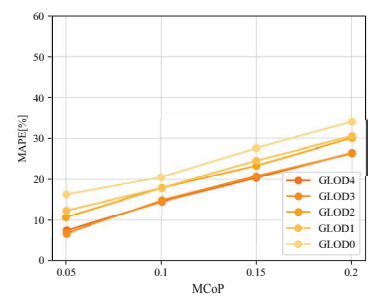

5 *WBG640*

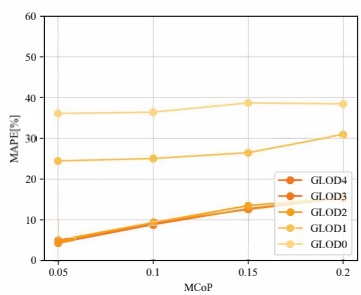

6 *MH_440*

FIG. 3.9 Influence of varying MCoP.

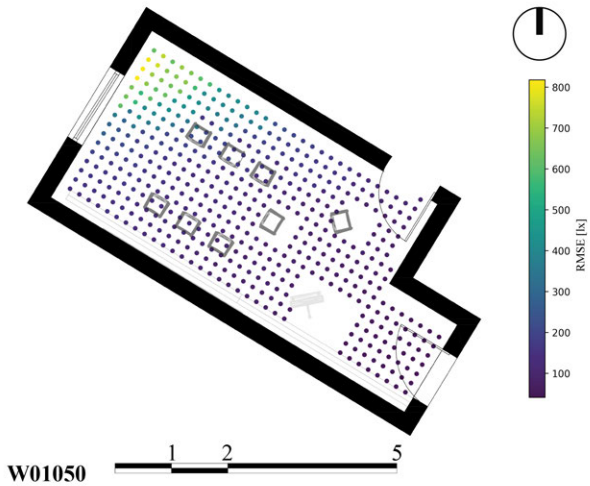

FIG. 3.10 Spatial distribution of prediction errors caused by inaccurate material definition (MCoP0.2-GLoD4–W01050).

3.6 Conclusion

In this study, the influence of inaccurate material definitions on annual daylight predictions is quantified. For this, a concept of MCoP was developed which is derived from measurements of in-use university and office spaces.

The errors arising from inaccurate measurement of material optical properties generally follow a normal distribution. Additionally, the uncertainty in measurements increases linearly with input material uncertainty, ranging between 10% and 30%, depending on the space. Notably, higher uncertainty occurs around the openings, primarily due to the significant influence of material transmittance variability.

The results of this study are useful for evaluating novel methods of material characterisation in daylight simulation, since they give insights into the potential propagation of errors caused by inaccurate modelling of key daylight simulation inputs, such as material optical properties.

The appropriate MCoP can be determined based on the available resources and the required accuracy for a specific application. This research provides a foundation for quantitatively assessing potential errors arising from novel material characterisation methods. In general, for broad daylight assessments of buildings, such as at regional or urban scales, a lower MCoP may be acceptable. However, for detailed indoor design decisions, higher MCoP values will yield more reliable results.

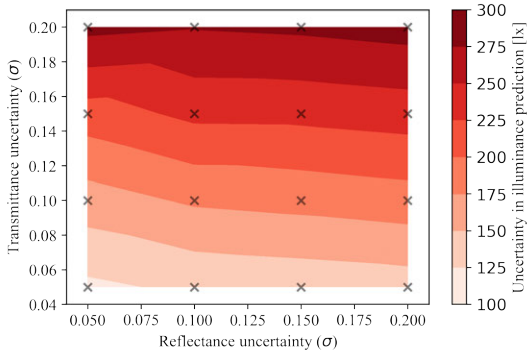

1 *W01050* (WFR: 9.1%)

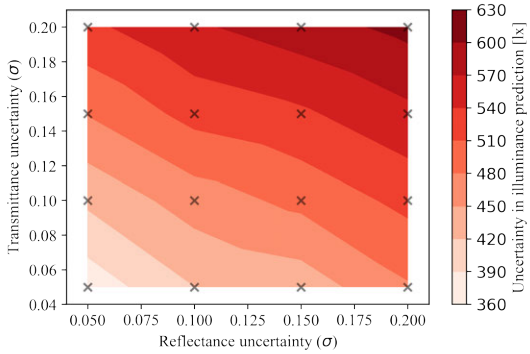

2 *MH_440* (WFR: 14.1%)

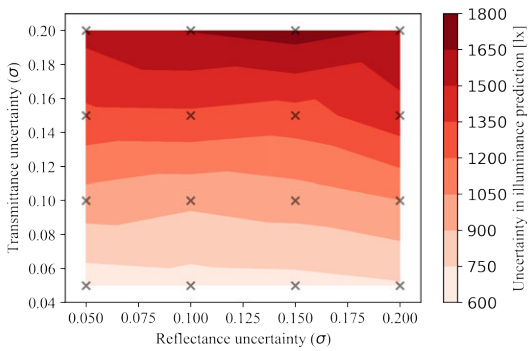

3 *WBG640* (WFR: 40.9%)

FIG. 3.11 Uncertainty in the calculation of annual grid-based illuminance values. Crosses represent the uncertainty as calculated in Eq. A.3. Gradient colours represent the interpolated uncertainty across the 2D domain of 0.05–0.20 reflectance–transmittance independent uncertainties.

The accuracy classes for materials were primarily defined based on measurements of opaque surfaces. Conducting similar detailed measurements for transparent surfaces would further strengthen the proposed framework.

In future studies, it is essential to advance automation to improve the efficiency and accuracy of daylight simulations using digital building models.

Introduction		
RQ1	How sensitive are CBDM results to geometric levels of detail?	Chapter 2
RQ2	What are the uncertainties caused by inaccurate material definition in CBDM results?	Chapter 3
RQ3	**How can indoor geometries be efficiently reconstructed to meet the requirements of daylight simulation models?**	**Chapter 4**
RQ4	To what extent can image-based material characterisation techniques be applied to simulated indoor daylight models?	Chapter 5
RQ5	How can simulated spectral indoor models be calibrated to account for uncertainties in scene reconstruction?	Chapter 6
Conclusion		

4 Semi-automatic reconstruction of room geometry

ABSTRACT

This study presents a semi-automatic pipeline for reconstructing indoor geometries from point cloud data for daylight simulation. The pipeline generates watertight models of permanent architectural surfaces with window boundaries through three steps: (1) preprocessing, (2) permanent structure reconstruction, and (3) window boundary extraction. The pipeline was evaluated in four rooms of varying complexity against manually reconstructed models using visual and geometrical comparisons, and by comparing daylight availability and glare metrics calculated from *Radiance* results. Geometric deviations in terms of Chamfer Distance (CD) were found to be smaller than one centimetre for regular rooms and up to 51cm for complex rooms. Across annual daylight metrics, spatial Daylight Autonomy (sDA) and Annual Sunlight Exposure (ASE) showed less than 6% bias, while UDI_a exhibited spatial biases ranging from approximately -2% to 40%, and the mean TAI bias remained below 16% in all rooms. The Daylight Glare Probability (DGP) error remained under 4%, and the modelling time did not exceed 5 minutes for any scenario. The approach enables rapid generation of simulation-ready models with acceptable accuracy for Climate-based daylight modelling (CBDM).

This chapter is published in the peer-reviewed journal article: Forouzandeh, N., Huang, J., Nan, L., Brembilla, E., & Stoter, J. (2026). *Semi-automated indoor geometry reconstruction for daylight simulation*. Building and Environment. https://doi.org/10.1016/j.buildenv.2025.114045.

4.1 Introduction

Although simulation-based design methodologies and pipelines are well-developed, studies on real buildings with occupant participation remain limited (De La Barra et al., 2025). Simulated models of advanced façades systems show significant potential for energy savings and occupants' comfort (Tabatabaei Manesh et al., 2025), yet alignment with real-world performance is often lacking. Obtaining accurate digital daylight models for existing buildings can substantially reduce the effort required for reliable monitoring and, therefore, building management. As building-control algorithms advance rapidly, efficient methods to generate valid digital representations of existing buildings are essential to align simulations with real-world performance.

Indoor geometry is an essential input for those digital models. It can be modelled in different Geometrical Levels of Detail (GLoDs) as proposed in previous work (Forouzandeh et al., 2024). In such a framework, GLoD0 only contains the permanent objects of an indoor space and is the basis for simulation-based decision making. Permanent objects determine the daylight potential of the room and remain constant irrespective of short-term changes, *e.g.*, redecoration, and long-term interventions, *e.g.*, retrofit actions. Higher GLoDs 1-4 include non-permanent objects with size thresholds that incrementally get smaller. On average GLoD0 introduces errors of 18.05% on Total Annual Illumination (TAI) although it halves the simulation time.

Unlike newly-built buildings, where geometrical properties are digitally defined at the design stage and can be used for daylight assessments, modifying existing buildings requires reliable geometrical models that are acquired on-site. This is often done manually, requiring substantial on-site labour. Laser scanning technology was invented to address this in the 1960s, and it became popular in engineering applications by the late 1990s. Since then, various on-site scanning workflows have evolved beyond passive scanning of scenes or objects–some of which are described later more in detail in the section 4.2. These workflows include scanning combined with physical manipulation of objects, active scene illumination, and the integration of LiDAR sensor data with other sensor information, all aimed at achieving a geometrically accurate representation of objects, better suited to their physical characteristics (Ye et al., 2015). These methods provide users with dense and redundant geometric information about the scene, including at least a point cloud that contains the 3D coordinates of points.

Daylight simulation, like other simulations, requires a detailed surface model, rather than raw point cloud data. Surface models can be reconstructed from points manually using Computer-aided design (CAD) interfaces (Quek and Jakubiec, 2021), but the downside is significant manual labour. Several surface reconstruction algorithms and techniques have been proposed in the literature to automate all or parts of the workflow to reconstruct surfaces from point clouds (Tang et al., 2010). In general, developing an efficient reconstruction pipeline for indoor applications,

often referred to as ‘scan-to-BIM’ in the Architecture, Engineering, Construction, Operation (AECO) industry, is fully dependent on the final application. For indoor daylight simulation, this pipeline typically involves the reconstruction of three key components: (1) a watertight structure of permanent surfaces, which is a closed set of surfaces representing the room shell (*i.e.*, walls, floor, and ceiling), (2) window boundaries, and (3) furniture.

In this chapter, a three-step semi-automatic indoor geometry reconstruction pipeline is developed to generate the window-containing geometry of the rooms from raw point cloud data with reduced user interactions, which includes (1) preprocessing, (2) reconstruction of a window-less watertight indoor model, and (3) reconstruction of windows. This GLoD0 geometry of the room provides a stable representation of the room. In most refurbishment and retrofit projects, furniture layouts are typically undecided whereas permanent elements are not, and excluding furniture reduces processing time and user input while representing the room’s overall daylight potential

This work offers an open-source and practical middle-ground solution between manual and fully automated scan-to-BIM methods. Unlike manual modelling, which is labour-intensive and time-consuming (often requiring hours per room), the proposed pipeline reduces modelling time to under five minutes per room. Unlike so-called fully automated techniques, which often rely on rigid geometric priors and can fail under partial occlusions or noisy scans, the proposed approach includes reduced user input to guide and validate window detection.

This approach has practical relevance for building retrofit projects, where accurate digital geometry is needed for retrofit actions such as lighting upgrades or envelope interventions (Ma et al., 2012). It is also applicable in facility management contexts, where reliable 3D models can inform the design and control of daylight systems, improve visual comfort, and reduce energy consumption (Ghansah, 2024). Finally, the method supports post-occupancy evaluation studies (Li et al., 2018) by enabling rapid creation of simulation-ready models that can be used to link measured performance with simulations.

4.2 Literature review

Synchronous survey of light and geometrical properties of indoors has been approached using both High Dynamic Range (HDR) and Light Detection and Ranging (LiDAR) data. Kim and Tzempelikos (2021) proposed a semi-automated technique to reconstruct the luminance distribution within the occupant’s field of view by reprojecting HDRs luminance maps onto a three-dimensional model. In a

subsequent and related study, the same authors experimentally validated this approach under controlled laboratory conditions, demonstrating that the DGP error of the re-projected luminance maps remained within acceptable limits (Kim and Tzempelikos, 2022). Rodrigue et al. (2022) conducted surveys of actual buildings using HDR imaging for luminance capture and LiDAR scanning as a complementary source for acquiring geometric data. Kurkela et al. (2021) applied photogrammetry techniques to reconstruct three-dimensional luminance point clouds of indoor spaces, relying solely on HDR imaging. In another study, they utilized LiDAR technology in combination with colour targets to measure indoor luminance directly from geometry (Kurkela et al., 2022). Finally, Cai (2013) performed synchronous measurements of indoor luminance and geometry using HDR imaging techniques. These studies are limited to a single point-in-time analysis—corresponding to the time when the survey campaign takes place—although they give a measure of both geometry and light.

Another approach is to use point cloud data from geometric surveys as input for daylight simulations, previously proposed by Bognár *et al.* (Bognár et al., 2021) on urban domain. Indoor surface reconstruction is applied in building physics and simulation domains, including indoor acoustics simulation (Markovic et al., 2013), and energy simulation (Garwood et al., 2017; Valero et al., 2021; Adán et al., 2023). Although there are not many studies dedicated to simulating daylight or other building physics applications, many of them are relevant when addressing the above key requirements, *i.e.*, watertight permanent structure, including window boundaries. Those studies are presented in this section with an emphasis on permanent structure and window boundaries and a summary of reconstruction algorithm steps in those studies is presented in Table 4.1.

- *Permanent structure*. Real-world building surfaces are typically planar. Many building surface reconstruction algorithms leverage this assumption to segment points on the ceiling, wall, and floor prior to surface reconstruction. This geometric pattern informs the reconstruction pipeline and allows the use of planar segmentation algorithms like Principal Component Analysis (PCA) and Random Sample Consensus (RANSAC) for detecting points belonging to these surfaces (Assi et al., 2019; Díaz-Vilariño et al., 2014; Tang et al., 2010).
- *Window boundaries*. Daylight simulation results are highly sensitive to the accuracy of window boundaries, making their precise reconstruction critical. Various studies have approached this, in most of which, windows are assumed to be rectangular holes within wall point clouds. This prior is commonly used to identify potential openings. Edge points of such openings are detected using alpha shape or Canny edge detection algorithms (Smit, 2022; Wei et al., 2023; Michailidis and Pajarola, 2017; Li et al., 2020), followed by clustering to form regions as candidate openings (Michailidis and Pajarola, 2017; Shi et al., 2018; Tang et al., 2019). To distinguish actual openings from other types of occlusions, shape priors are employed. For instance, Smit (2022) and Jung et al. (2018) apply rectangle fitting, while Michailidis and Pajarola (2017) use RANSAC-based line fitting.

  Beyond rule-based methods, artificial intelligence techniques have been adopted for differentiating between the two types of openings, *i.e.*, windows and doors (Fotsing et al., 2024; Ochmann et al., 2016). More advanced approaches leverage semantic

and instance segmentation using deep learning networks such as YOLO (Zhong et al., 2022; Pan et al., 2022). The output of these networks is then used to reconstruct window geometries either through bounding box fitting (Kellner et al., 2023), projection of detected masks onto wall geometry (Wong et al., 2025), or by replacing them with pre-modelled window objects from libraries (Mehranfar et al., 2024).

TABLE 4.1 A summary of the reconstruction algorithms. The listed works are not applied to daylight simulation.

Reference	Algorithm
Wei et al. (2023)	(1) Extraction of alpha shape for the opening-containing wall to extract edge points, (2) Regularization of edge points with Semantic-constrained optimization.
Xiaojuan et al. (2021)	(1) Detection of the occlusion area on the wall segment by constructing scanning rays, (2) Extraction of wall edge points, (3) Extraction of the feature line of the wall according to the point density, (4) Forming a cell complex by the intersection of feature lines, (5) Extraction of the doors and windows by graph cut based on Ford Fulkerson.
Michailidis and Pajarola (2017)	(1) Alpha shape computation of wall segment, (2) RANSAC line fitting, (3) Mean-shift clustering, (4) Forming a cell complex, (5) Graph-cut cell segmentation.
Li et al. (2020)	(1) Wall Surface Detection, (2) Extraction of candidate opening boundary points with alpha shape, (3) Opening Edge Fitting, (4) Opening Reconstruction.
Previtali et al. (2018)	(1) Extraction of holes in planar wall segments, (2) Filtering false positives using geometric constraints, (3) Refine the opening boundaries using edge detection or histogram projection, (4) Assign opening types (*e.g.*, windows, doors) based on position, size, and semantic rules, (5) Reconstruction of openings as bounded voids in wall geometry or as separate mesh components.
Jung et al. (2018)	(1) Rectangular hole extraction from the segmented wall point segments, (2) Refinement.
Shi et al. (2018)	(1) Gridding 2D projected data to identify low-density areas, (2) Applying region growing to group empty areas and pruning occlusions, (3) Extracting geometric and density-based features for each cluster, (4) Formulating an object-based graph cut problem, (5) Minimizing an energy function combining data term (point density likelihood) and smoothness term (area, floor-ceiling proximity, and shape linearity), (6) Classifying resulting objects into windows, doors, or virtual openings.

Continued on next page

Reference	Algorithm
Tang et al. (2019)	(1) Tagging RGB-D frames near openings based on camera trajectory and scan timestamps, (2) Segmentation of vertical planes from tagged frames, (3) Computing the convex hull of each segmented plane and filling it with synthetic points, (4) Comparing original and filled planes using octree-based KNN search to detect vacant regions, (5) Clustering vacancy regions using Euclidean distance, (6) Reconstructing each opening by combining 3D boundary data with 2D line fitting.
Assi et al. (2019)	(1) Transform planar wall point segments to 2D image, (2) Image cleaning, (3) Clustering regions with region growing, (4) Calculate energy function with geometric terms (*e.g.*, proximity to ceilings, size, and proportions) to determine openings.
Smit (2022)	(1) Calculate Euclidean distances, (2) Mercator Projection, (3) Point cloud $\rightarrow$ 3D Histogram $\rightarrow$ 2D image, (4) CLAHE, (5) Canny edge detection, (6) Contour Extraction, (7) Rectangle validation, (8) Cluster ROIs to deduce window regions.
Pan et al. (2022)	(1) Semantic segmentation, (2) Applying voxel growing, (3) Classification of voxels into void and non-void, (4) Fitting rectangles on empty voxels corresponding to openings.
Zhong et al. (2022)	(1) Instance segmentation network to separate elements (doors, windows), (2) Hierarchical grouping of points to merge semantically segmented points into multi-scale groups.
Kellner et al. (2023)	(1) Computing geometric features (*e.g.*, planarity, linearity, surface variation) for points, (2) Using networks (PointTransformer, RandLA-Net, KpConv) for semantic segmentation, (3) Bounding box fitting for each opening.
Fotsing et al. (2024)	(1) Extraction of holes from wall segments based on point density in a grid fitted to wall points, (2) Classification separating windows and doors via deep learning.
Mehranfar et al. (2024)	(1) Detection of door and window bounding boxes in open, semi-open, and closed states with YOLOv8 trained on 214 RGB images and 89 projected wall images, (2) Replacement with 3D models from a library.
Wong et al. (2025)	(1) Semantic segmentation using YOLOv8 to acquire pixel-wise class information of building elements from video frames (HBD dataset), (2) Projection of the mask onto the wall.
Ochmann et al. (2016)	(1) Determination of ray intersections with walls emitted from scanner location, (2) Clustering of intersection points, (3) Classification of openings as windows or doors with supervised learning.

Díaz-Vilariño et al. (2014) propose a reconstruction pipeline for indoor daylight

simulation. To reconstruct opaque surfaces, the authors use PCAs and region growing to detect the surface planes and later intersect them. For openings, by assuming a low density of points in the openings, they use PCAs for linear edge detection. The labelling of the openings on the walls is achieved through user interactions. Their technique is not validated against manually reconstructed models. Therefore, the error associated with their geometrical modelling is not known.

Although these methods rely on hardcoded or learned priors, they do not guarantee complete reconstruction of window boundaries. For daylight simulations, geometric accuracy must be verified before use. Therefore, rather than depending on fully automated pipelines, the approach proposed in this chapter incorporates reduced user input to guide the workflow and validate window geometry.

In summary, existing approaches either demand extensive manual effort or depend heavily on assumptions that may not hold in practice. This work introduces a pipeline that reduces modelling time without sacrificing geometric reliability. It produces watertight, window-containing room models suitable for daylight analysis.

4.3 Methodology

The proposed methodology addresses the difficulty in reconstructing watertight window-containing surface models from point cloud data, suitable for daylight simulations. This work integrates existing methods to create a semi-automated pipeline for generating simulation-ready geometry with reduced user interaction to ensure complete window detection. The key contribution is in the introduction of a three-step pipeline for daylight simulation studies. The method is tested on five rooms of varying size and surface properties, and validated against manually reconstructed room geometries across several performance metrics relevant to daylight simulations.

4.3.1 Reconstruction pipeline

The reconstruction pipeline, as shown in Fig. 4.1, includes three key steps: (1) preprocessing, (2) reconstruction of the permanent structure, and (3) reconstruction of window boundaries, each described in separate subsections, followed by a description of geometrical and daylight comparison methods.

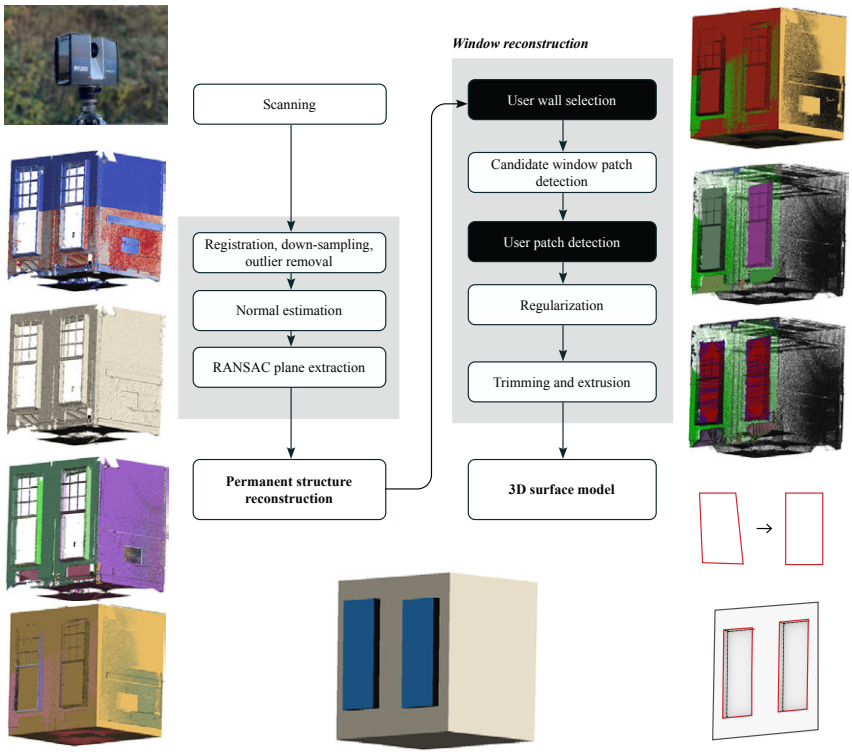

FIG. 4.1 Reconstruction pipeline. Manual steps are shown in black, and automated steps are shown in white. Visual examples beside each block illustrate the corresponding stage of the process, from raw scanning to final 3D model generation.

4.3.1.1 Preprocessing

After registering the scans, the outlier points, *i.e.*, the ones outside the room, are manually deleted. Next, the point cloud is randomly down-sampled to reduce the processing time in the subsequent steps. Afterwards, the point normals are estimated with a neighbour size of 16. In this context, the neighbour size refers to the number of nearby points used to locally estimate the surface orientation required by the RANSAC plane detection. This is followed by a RANSAC plane extraction, whose hyperparameters are listed in Table 4.2. Such values are listed for repeatability. More explanations about the RANSAC process and its hyperparameters are laid out by (Fischler and Bolles, 1981). This point cloud is then used as input for *PolyFit*—a surface reconstruction algorithm that generates watertight polygonal models by fitting planar segments to point cloud data using optimization (Nan and Wonka, 2017).

TABLE 4.2 RANSAC parameters used in this work for plane extraction

Parameter	Value
Minimum support	1,000–4,000
Distance threshold	0.005
Bitmap resolution	0.02
Normal threshold	0.8
Overlook probability	0.001

4.3.1.2 Permanent structure reconstruction

This step reconstructs the watertight permanent structure, *i.e.*, walls, ceiling, and the floor of the room, using *PolyFit* (Nan and Wonka, 2017). An example is shown in Fig. 4.2.

4.3.1.3 Window reconstruction

As the first step of the window reconstruction pipeline, *i.e.*, the *wall selection* step, the user is asked to select the surfaces containing windows with a single click per window-containing wall (Fig. 4.2). The program stores these selected walls with their corresponding planes and points from the previous step.

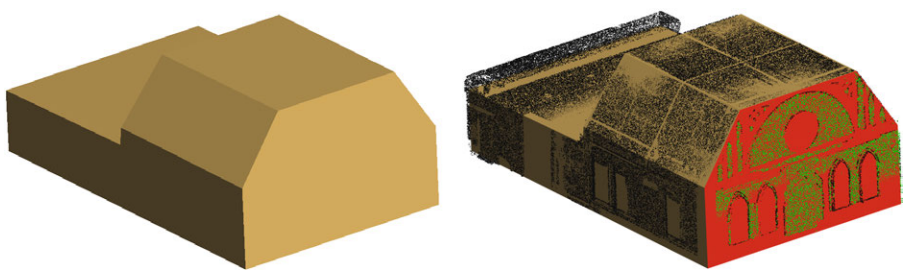

FIG. 4.2 An example of permanent structure reconstructed using *PolyFit* (left) and user wall selection (right).

During *candidate window patch detection*, for each of the picked walls, the corresponding points are first mapped onto its underlying plane, and then a Delaunay triangulation is applied to these 2D points to establish local connectivity between neighbouring samples. In this triangulation, points are connected into non-overlapping triangles such that no point lies inside the circumcircle of any triangle. This is followed by automatic detection of *hole*s, *region*s, and *candidate window patches*. A *hole* is defined as a face in the Delaunay triangulation where all

edges have lengths greater than a specified threshold. This threshold is empirically set to 8 cm. A *region* is a connected group of *hole* faces from the previous step, where each *region* is assigned a unique label. The detection process involves grouping adjacent *hole* faces into distinct *region*s. *Candidate window patch*es are *region*s that meet a user-specified area criterion (10 cm^2 in this work). *Region*s with an area smaller than this threshold are excluded from being *candidate window patch*es (Fig. 4.3).

The edge-length threshold of 8 cm defines the minimum gap size considered as an opening. Edges shorter than this value are considered as part of opaque wall surfaces rather than holes. Likewise, regions with an area smaller than 10 cm^2 are excluded from window detection, as they typically result from occlusions, missing data near edges, or measurement noise. These thresholds makes the visualisation algorithm ignore small, non-window gaps so the user can focus on identifying actual openings during *user window patch selection*. The values were determined empirically based on the scan resolution and building dimensions in this study, assuming that windows are much larger than 10 cm^2. Both parameters are adjustable in the program to match different room types and scan qualities.

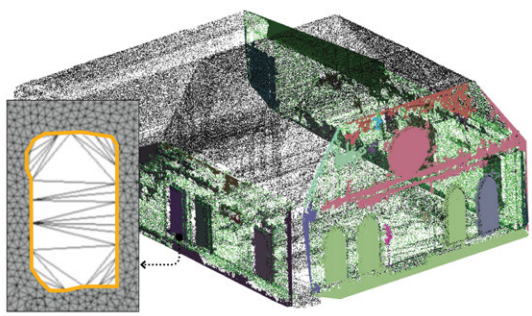

FIG. 4.3 Candidate window patch detection workflow. Triangles exceeding the edge-length threshold from the Delaunay triangulation are classified as *holes* (white faces), while the remaining faces are non-hole faces (grey faces). Connected hole faces are grouped into labelled *regions*, and regions that satisfy the area criterion are identified as *candidate window patches (yellow edge)*.

Next, during *user window patch selection*, the faces corresponding to one window are picked with a lasso tool in separate stages per wall. The lasso tool allows the user to freely select a region on the desired faces.

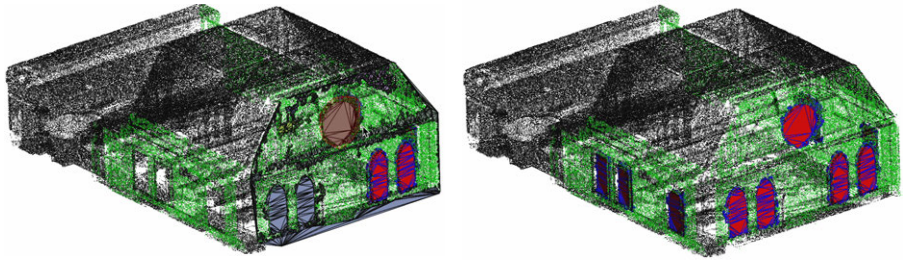

FIG. 4.4 User window patch selection, while user draws the lasso tool (left) and completed selection (right).

As the initial extracted window boundaries are inevitably irregular, a *window boundary regularization* proposed by Huang et al. (2023) is adopted. Lastly, during *trimming and extrusion*, the regularized boundaries are trimmed from the corresponding walls and defined as the window boundary layer, and a user-defined extrusion is applied to carve the windows from the walls. The final 3D surface model is then used directly for daylight simulation, as the polygonal mesh representation sufficiently describes the planar geometry of the reconstructed rooms.

4.3.2 Implementation

The pipeline is implemented in C++. Core geometry processing, visualization and user interaction are done using the *Easy3D* library (Nan, 2021). A screenshot of the program interface during user interaction is shown in Fig. 4.5. Watertight surface reconstruction is performed using *PolyFit* (Nan and Wonka, 2017). The software follows a modular architecture, separating components for permanent-structure reconstruction and window-boundary extraction. The *CGAL* library is employed for Delaunay triangulation and related geometric operations (Fabri and Pion, 2009).

The pipeline uses 3D point cloud data as its primary input. Raw point clouds are stored as PLY files containing XYZ coordinates and normal information for each point, estimated during preprocessing. After plane detection, the processed point clouds are saved as BVG files, which include segmented planar regions and associated metadata required for surface reconstruction. The data are acquired using terrestrial laser scanning, capturing dense spatial samples of indoor environments. All input point clouds are subsampled to approximately 100,000 points to reduce processing time while preserving sufficient geometric detail for accurate surface reconstruction and window detection.

All reconstructions were performed on a MacBook Pro (13-inch, Apple M1 chip, 16 GB RAM) running macOS Sequoia 15.7.1.

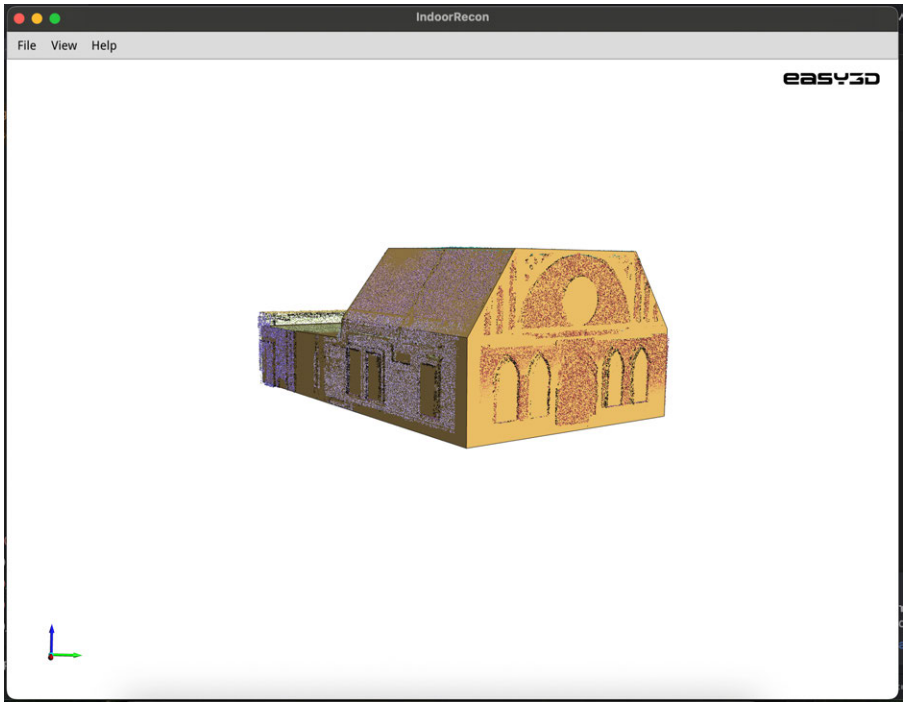

FIG. 4.5 A screen shot of the program during the user interaction.

4.3.3 Use case rooms

In this study, individual rooms are used as the unit of analysis for both reconstruction and simulation. A room is defined as a single enclosed indoor space bounded by permanent architectural surfaces (walls, floor, ceiling) and containing window openings that connect it to the exterior. This focus allows for consistent comparison across cases and ensures that the reconstructed geometry represents the primary spatial enclosure relevant to daylight performance.

Five rooms with varying sizes, shapes, and window complexity were chosen to cover both typical and challenging room geometries for reconstruction. The rooms are shown in Fig. 4.6 and described in Table 4.3. The test set includes three office/meeting spaces (*W01050*, *WBG640*, *WBG550*) with orthogonal envelopes, rectangular windows, and moderate window–floor ratios; one classroom (*DA200*) with non-rectangular openings and non-orthogonal geometry; and one large public hall (*OrangeHall*) with a large size, lots of clutter, and a complex form.

TABLE 4.3 Description of the rooms

Space ID	Location	Room use	Dimensions [m*m*m]	WFR [%]
W01050	Delft, NL	Meeting room	5.8×4.4×5.8	9.1
WBG640	Delft, NL	Meeting room	7.2×3.4×2.6	40.9
WBG550	Delft, NL	Open office	12×9.8×5.8	29.4
DA200	Toronto, CA	Classroom	16.6×10.6×3.5-6.7	9.1
OrangeHall	Delft, NL	Faculty public hall	33×30×13	40

4.3.4 Generation of ground truth models

The ground truth models were constructed manually in *Rhinoceros 3D*. First, the registered point clouds—identical to those used in the semi-automatic pipeline—were imported. The surface model of each element was then created either by snapping rectangle endpoints to corner points or by drawing polylines and extruding them. This manual modelling was performed independently of the user-interaction steps in the semi-automatic workflow; however, both are carried out by the author.

4.3.5 Performance evaluation

Visual comparisons. All rooms have been reconstructed using the proposed semi-automatic approach and are qualitatively compared to the manually reconstructed models.

Geometrical accuracy. To quantitively complement the visual comparison and assess the geometric fidelity between the manually and semi-automatically reconstructed meshes, the geometric differences between the manually and semi-automatically reconstructed models are measured using two symmetric metrics:

1. *Chamfer Distance (CD)* compares the two meshes in both directions by averaging the squared nearest-neighbour distances between uniformly sampled point sets on each mesh (manual→reconstructed and reconstructed→manual).
2. *Hausdorff Distance (HD)* captures the worst-case deviation as the maximum of the two directed nearest-neighbour distances.

Each mesh was uniformly sampled to 80,000 points; nearest-neighbour queries were evaluated with k-d trees.

Daylight availability. To quantify the simulation error associated with manual and

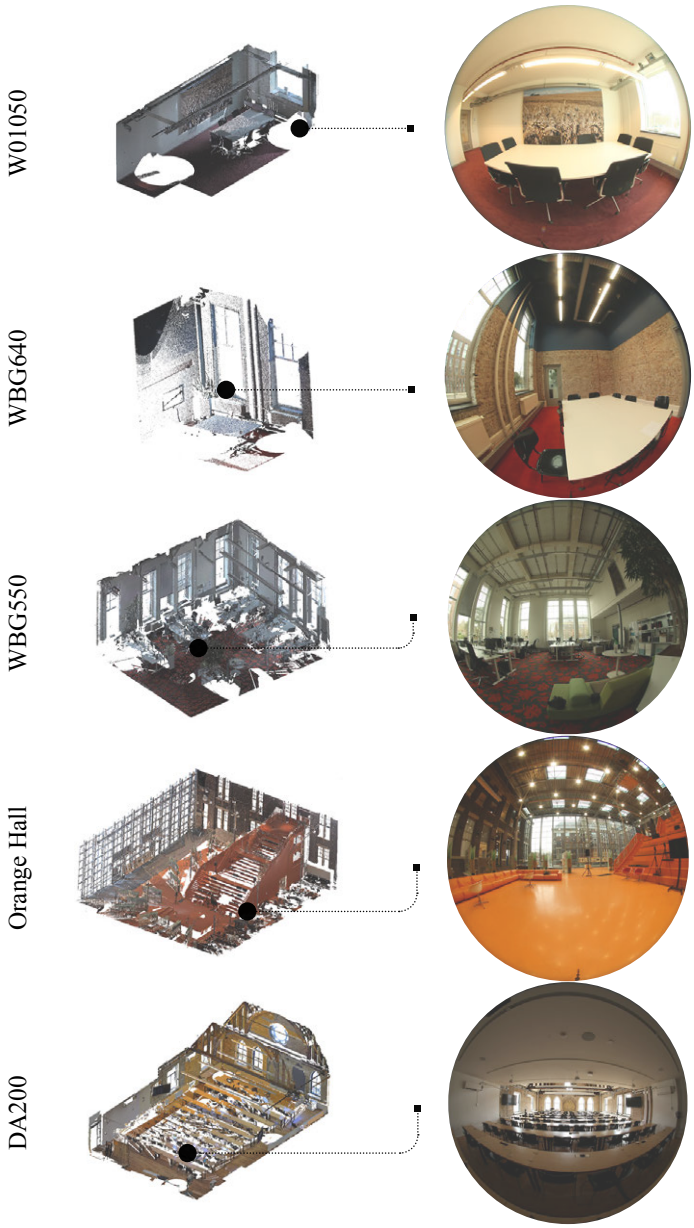

FIG. 4.6 Point clouds and an indoor view from the five rooms used for this study.

semi-automatic reconstruction pipelines, the annual illuminance values are compared in terms of:

1. spatial Daylight Autonomy (sDA) percentage of the floor area that receives at least 300 lx of daylight for at least 50% of occupied hours over the year
2. Annual Sunlight Exposure (ASE) percentage of the floor area exposed to direct sunlight exceeding 1000 lx for more than 250 hours per year. These two metrics are widely used in daylight-related certification schemes such as LEED for evaluating daylight performance.
3. Per-point Total Annual Illumination (TAI) as described in Eq. 4.1. TAI is used as a cumulative indicator of illuminance bias at each sensor location.

$$\mathrm{TAI}_g = \sum_{t=1}^{H} (E_t) \tag{4.1}$$

Where TAI_g is the Total Annual Illumination in lx.hour/year at point g, E_t is illuminance value at time step t, and H is the total number of sun-up hours in the simulation.

4. UDI for time-aggregated annual performance, with 300 lx and 3000 lx as thresholds to divide the three UDI ranges: insufficient, autonomous, and exceeding. The choice of the thresholds is based on the most recent updates from the original author of this metric, now implemented in recent simulation tools (Mardaljevic et al., 2012; Mardaljevic, 2015; Solemma LLC, 2025). In contrast to sDA and ASE, UDI provides a more comprehensive view of annual performance by capturing both underlit and overlit illuminance hours within a single framework.

   Temporal bias is defined here as as the illuminance Relative Bias (RB) across all annual time steps as in Eq. 4.3.

$$RB_t = \frac{E_{t,\text{semi-auto}} - E_{t,\text{manual}}}{E_{t,\text{manual}}} \times 100 \tag{4.2}$$

$$\text{TMRB} = \frac{1}{N_{\text{sun}}} \sum_{t=1}^{N_{\text{sun}}} RB_t \tag{4.3}$$

Where $E_{t,\text{semi-auto}}$ and $E_{t,\text{manual}}$ are the illuminance values at time step t from the semi-automatic and manual simulations, respectively, and N_{sun} is the number of sun-up hours.

A reflectance value of 0.5 is assumed equally across the three colour channels for opaque surfaces and a transmittance of 0.75 for glazings. The choice of the same reflectance value for all surfaces is not realistic, but was deliberately made to isolate the errors associated with only the geometrical differences as much as possible.

Work-plane illuminance was simulated on a grid with 0.30–1.00 m spacing in both perpendicular directions at a work-plane height of 0.80 m for both the automatically and manually reconstructed geometries. Simulations were performed by *Honeybee* which uses the *Radiance* engine , which has been validated against on-site

measurements (Subramaniam, 2018). The *Radiance* parameters of "-ad 2048 -as 1024 -aa 0.5 -ar 1024 -ab 6" and the Perez All-Weather sky model were selected. Hourly annual simulations assuming a full occupancy—with 4397 and 4400 sun-up hours for Delft and Toronto, respectively—were done by weather data retrieved from *Climate.OneBuilding.org* for the stations closest to Delft and Toronto (Crawley and Lawrie, 2019). [1]

Visual comfort. A sitting head pose was chosen for each use case as shown in Fig. 4.7. DGP was calculated using *evalglare* (Wienold and Reetz, 2004) from fisheye HDR renderings generated with the *Radiance* engine. Each rendering used the same parameters as the work-plane illuminance simulations, with a hemispherical fisheye view (`-vth`) at 180° horizontal and vertical field of view, and a resolution of 1000×1000 pixels. The default glare source identification (`-r 0.2 -b 2000`) was used without applying peak extraction thresholds or task area definitions. DGP was computed for 9 AM, 12 PM, and 3 PM on both solstices and equinoxes under a standard CIE clear sky, resulting in 12 time steps per room.

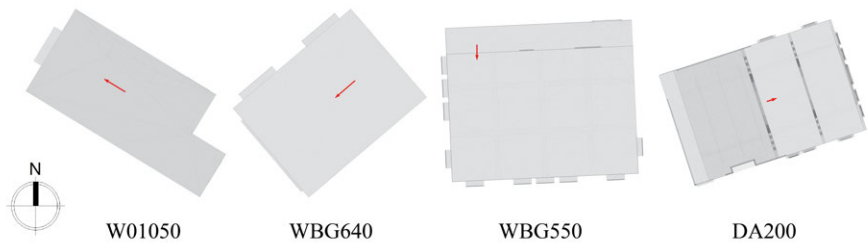

FIG. 4.7 Selected views for glare analysis

4.4 Results

Successful planar reconstruction was achieved using *PolyFit* for four out of five rooms, with both intermediate and final geometries presented in Fig. 4.8. Reconstruction of the *OrangeHall* was not successful due to its geometrical complexity as illustrated in Fig. 4.9. Specifically, this room contains big stairs with a unique and irregular shape in the middle and many large exhibition objects. There are a large number of points on these surfaces and therefore are picked by the optimization step in *PolyFit* (see Fig. 4.6).

For all successfully reconstructed cases, the total modelling time, comprising both

[1] EPW file names: `NLD_ZH_Rotterdam.The.Hague.AP.063440_TMYx.epw` and `CAN_ON_Toronto.City.715080_CWEC2016.epw`.

user interaction and automated processing, remained under 5 minutes.

4.4.1 Visual comparison

Manual and semi-automatically reconstructed rooms are visually compared in Fig. 4.10. The overall shape of the rooms aligns well with the ground truth–manually reconstructed–geometries. A similar level of agreement is observed for the windows, although mullions are not reconstructed in rooms WBG640 and *WBG550*. Additionally, the arched and curved geometry of the windows in room *DA200* is not fully captured by the reconstruction method.

4.4.2 Geometrical comparison

The geometric accuracy of the semi-automatic reconstructions was evaluated against the manually modelled ground truth using symmetric squared Chamfer (mean of directed terms) and HD (Table 4.4). Rooms *WBG640* and *W01050* show sub-centimetre mean deviations, which indicates close correspondence in walls and window boundaries. *WBG550* presents slightly higher deviations, and *DA200* exhibits the largest discrepancies.

TABLE 4.4 Geometric comparison between manually and semi-automatically reconstructed models (distances in metres).

Room	CD	HD
W01050	0.0041	0.157
WBG640	0.0014	0.169
WBG550	0.0187	1.015
DA200	0.5189	3.905

4.4.3 Daylight availability

Table 4.5 compares ASE and sDA between the manual and semi-automatic models. In *W01050*, sDA increases from 32% to 36%, while ASE rises from 0.57% to 2.46%. In *WBG640*, sDA stays at 100% for both models, with ASE increasing slightly

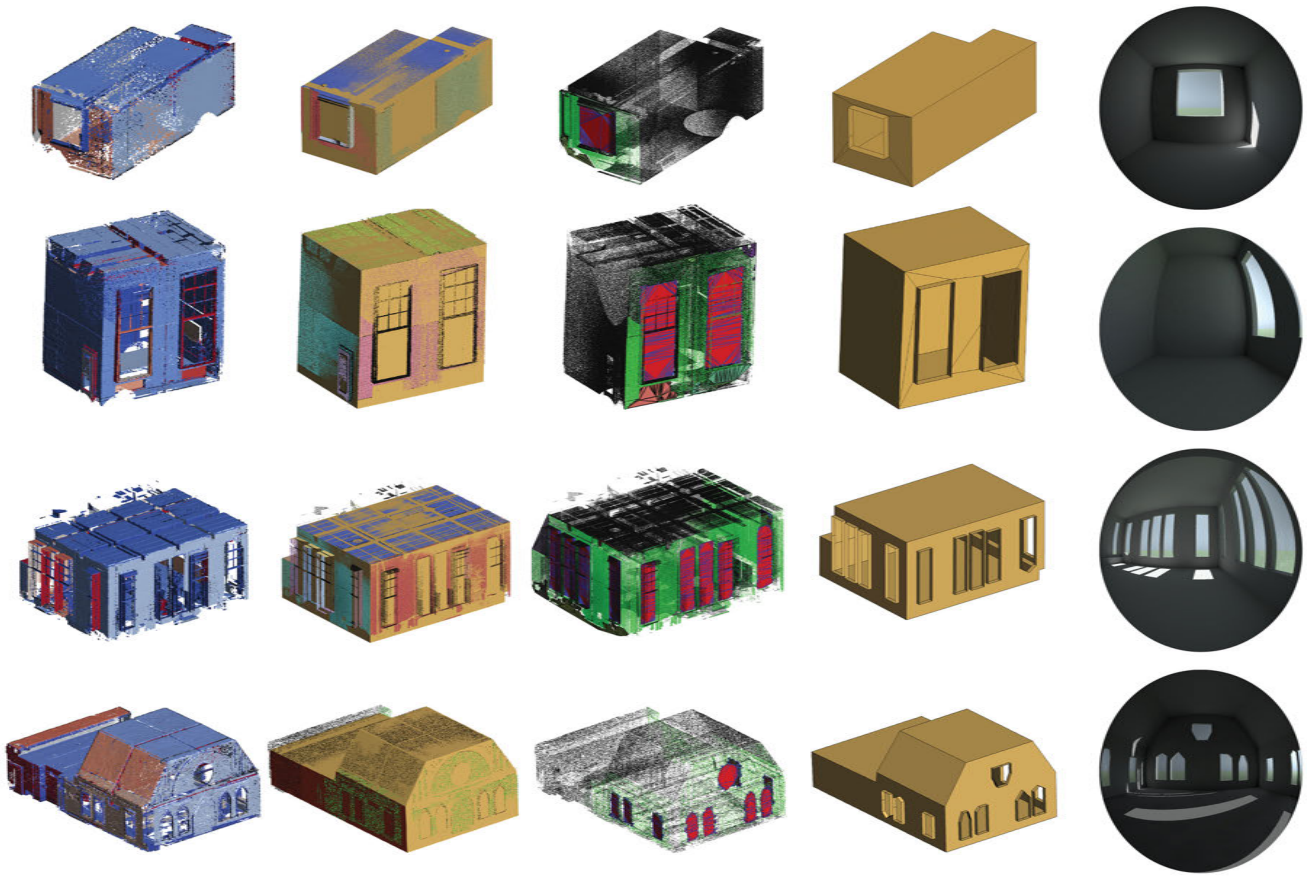

FIG. 4.8 Intermediate and final visualizations from the four successful reconstruction cases. From left to right: input point cloud, visible points and surfaces prior to user wall selection, user-marked window region, final 3D model, a fisheye render from the glare views corresponding to Fig. 4.7.

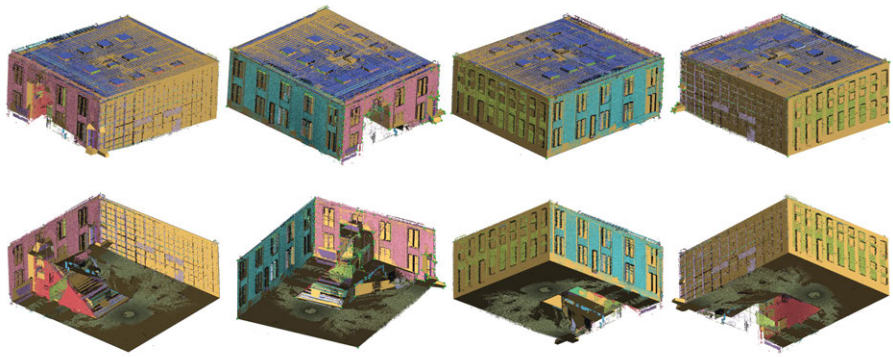

FIG. 4.9 A failure case. The *OrangeHall* contains a large number of points capturing interior objects, such as large exhibition objects and large staircases, resulting in undesired permanent structure reconstructed by *PolyFit*.

(0.30% $\rightarrow$ 0.89%). In *WBG550*, sDA remains 100%, while ASE increases by 6% (87.9% $\rightarrow$ 93.8%). In *DA200*, sDA increases from 52.0% to 54.0%, and ASE changes from 2.49% to 2.59%.

TABLE 4.5 ASE and sDA results

Room	ASE [%]		sDA [%]	
	Manual	Semi-auto	Manual	Semi-auto
W01050	0.57	2.46	32	36
WBG640	0.30	0.89	100	100
WBG550	87.94	93.82	100	100
DA200	2.49	2.59	52	54

The spatial relative biases of UDI are summarised in Table 4.6. UDI_i shows negative mean biases in all rooms, UDI_a exhibits large variation with mean biases ranging from approximately -1.5% to 40%, and UDI_e shows positive mean biases in every case. This indicates an overall tendency toward over prediction of daylight availability. The large standard deviations, particularly for *WBG550* and for UDI_a in *W01050*, indicate that these biases are not spatially uniform but are concentrated in specific regions of the sensor grid. The corresponding absolute UDI and TAI results are summarised in Appendix C.

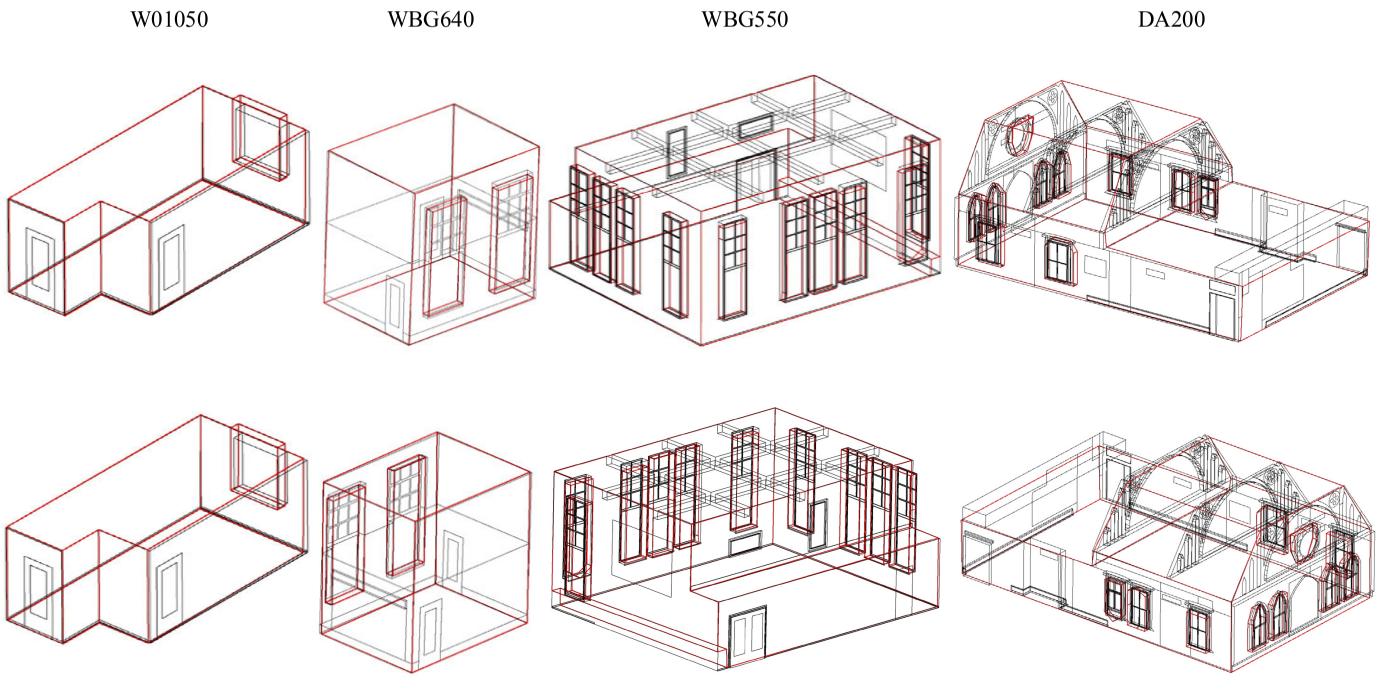

FIG. 4.10 Comparison of manually reconstructed (in black) with the proposed semi-automatic technique (in red).

TABLE 4.6 Spatial relative bias of UDI for (i)nsufficient, (a)utonomous, and (e)xceeding ranges.

Room	UDI_i		UDI_a		UDI_e	
	Mean [%]	Std [%]	Mean [%]	Std [%]	Mean [%]	Std [%]
W01050	-5.71	3.70	39.73	205.29	6.44	37.56
WBG640	-16.09	33.00	6.36	19.93	3.77	21.12
WBG550	-3.09	113.55	-1.54	45.32	25.84	42.11
DA200	-3.67	2.13	8.97	38.93	15.70	67.32

In terms of TAI, the mean and Standard Deviation (STD) values are summarised in Table 4.7. The results indicate a systematic over prediction across all rooms, primarily attributable to the larger reconstructed window areas and the omission of mullions in the semi-automatic models. The mean remains below 20% in all cases. The spatial distribution of this over prediction, shown in Fig. 4.11 (top row), shows that the bias is most pronounced near window regions, gradually decreasing with distance from the façade.

TABLE 4.7 Summary of spatial relative bias for TAI

Room	Mean [%]	STD [%]
W01050	15.97	3.39
WBG640	11.91	1.36
WBG550	14.93	7.34
DA200	9.52	2.49

Fig. 4.12 shows the annual variability of temporal RB values for a single sensor in the middle of each room along with the corresponding
Temporal Mean Relative Bias (TMRB). This analysis shows that the bias is highly variable throughout the year. In addition to the temporal analysis, spatial variability of TMRB values was also examined. However, no clear spatial trend was observed, and these results are therefore not presented. The spatial statistical summary for all rooms is presented in Appendix D.

FIG. 4.11 TAI heat maps for semi-automatic (bottom) and manual (middle) geometries, along with their bias (top).

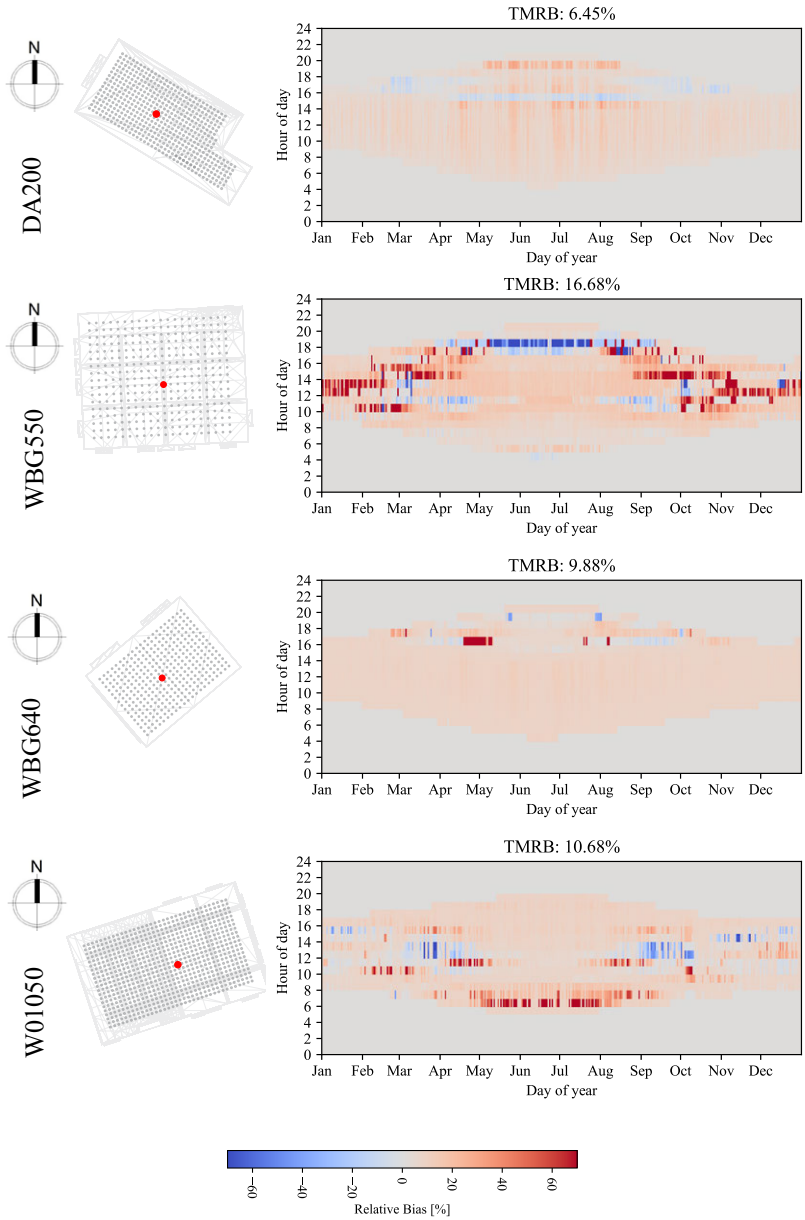

FIG. 4.12 Temporal illuminance relative bias across rooms. Left: sensor locations. Right: corresponding relative bias (RB).

4.4.4 Glare

Fig. 4.13 shows false colour luminance renderings for 21st of June on 15:00 under clear sky and Fig. 4.14 compares DGP from manual and semi-automatic models across all the rendered time steps. The RMSE values are 0.0399, 0.0034, 0.0152, and 0.0220 for *W01050*, *WBG640*, *WBG550*, and *DA200*, respectively.

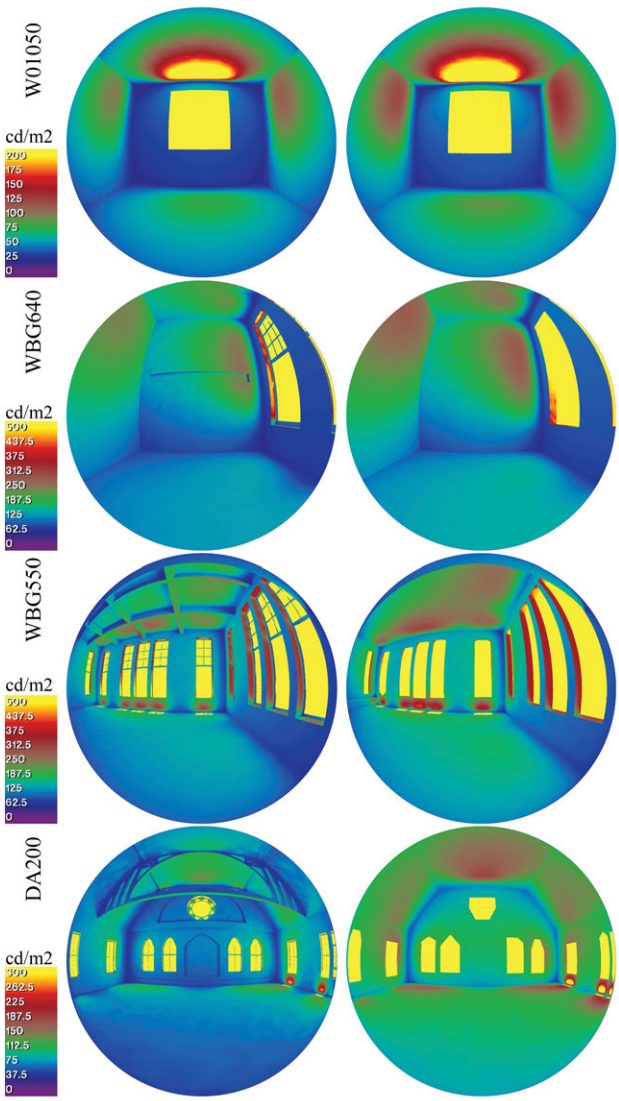

FIG. 4.13 False colour images of the summer solstice time step for manual (left) and semi-automatic (right) geometries.

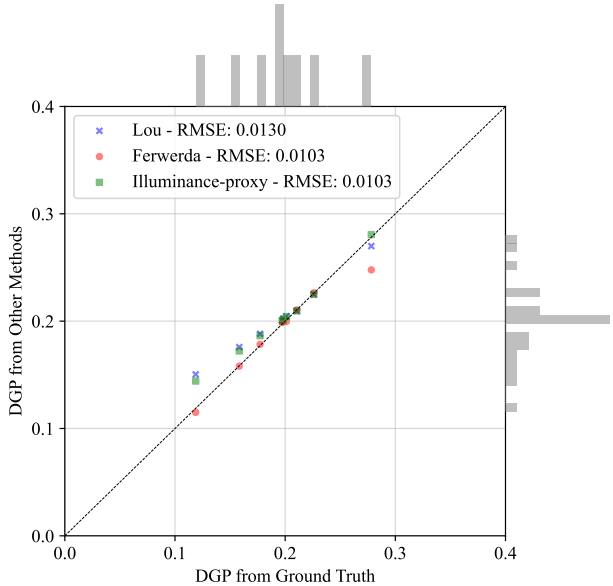

FIG. 4.14 DGP for manual and semi-automatic reconstruction pipelines

4.5 Discussion

4.5.1 Advantages

A key advantage of the proposed approach is the significantly reduced modelling time. For all four successfully reconstructed rooms, the total modelling time remained under 5 minutes. This is substantially shorter than the time required to manually model the rooms used as ground truth in this study. The manual modelling process took approximately 15 hours per room on average (including furniture), reconstructing only the GLoD0 would presumably take about half of that time, which still far exceeds the duration of the proposed pipeline.

A concurrent advantage of this small user interaction is that it mitigates the ambiguity introduced by the assumption that windows appear as holes in point clouds. Most of the fully automated methods reviewed in Section 4.2 rely on heuristics to identify window candidates, such as rectangularity, edge linearity, proximity to floor and

ceiling planes, and alignment patterns. These assumptions are not robust, particularly in the presence of occlusions or incomplete scans. By incorporating brief user input during the window selection stage, the proposed method reduces the risk of false detections and ensures that only valid window regions are processed, improving both the accuracy and robustness of the reconstruction pipeline.

A third advantage is the guaranteed water tightness. GLoD0 is the simplest resolution of indoor geometry for any type of daylight analysis, and remains unaffected by changes in indoor configurations. Water tightness is an important and basic requirement for indoor daylight models to ensure that simulated daylight has only permeated the room through the transparent surfaces. This requirement is assured by the design of the proposed algorithm.

A fourth advantage is the inclusion of window extrusion in the reconstructed models. Window details are critical for daylight simulation, *e.g.*, window frames or sills may cause glare or significant reflected luminance. This work has therefore included an extrusion of windows so that those effects are captured in the output. This is an efficient approach compared to extruding the whole wall, which potentially adds unnecessary complexity to the model.

A fifth advantage is that the proposed algorithm assumes that the windows are individually symmetrical. Unlike similar studies in the literature that take a more specific prior, *i.e.*, rectangularity of windows, the symmetric assumption is a more robust architectural prior, given that many windows in historic buildings are symmetrical and not rectangular.

The sixth advantage is the overall alignment between the semi-automatic and manual geometries, which is promising. The sDA results show less than 5% bias and ASE less than 6% bias, while TAI remains below 16% relative bias across all rooms. The geometric comparison also shows a close agreement for rectilinear cases, with CD of less than one centimetre in *W01050* and *WBG640*, and discrepancies of up to 51 centimetre in more complex rooms. Although UDI shows larger deviations (up to 39%) and higher variability, this behaviour is inherent to the metric due to its categorical binning.

Finally, the glare evaluation using DGP showed consistent performance. The RMSE of DGP values between the manual and semi-automatic models remained below 0.04 in all cases, indicating good agreement in predicting occupant visual comfort. This suggests that, despite geometric simplifications, the reconstructed models capture the primary geometric features that influence daylight availability and visual comfort in a sufficient manner.

4.5.2 Limitations

This study has limitations that highlight directions for future work.

The most fundamental assumption underlying the proposed reconstruction algorithm is that indoor surfaces are planar. This assumption originates from the reliance on the *PolyFit* method, which operates on planes extracted using RANSAC. While this is valid for most architectural elements such as walls, floors, and ceilings, it does not hold for spaces with curved or irregular geometries.

The reconstruction pipeline also inherits limitations from *PolyFit*. As noted by the original authors, this technique is suited to simple polygonal (piecewise-planar) surfaces and may encounter bottlenecks on large or complex geometries (Nan and Wonka, 2017). This was evident in the *Orange Hall* case, where geometrical and topological complexities produced an excessive number of candidate faces, causing the reconstruction to fail. Furthermore, the non-rectangular and arched window geometries in *DA200* challenged the boundary regularization step, increasing daylight-availability errors, though the impact on visual comfort remained minimal. Isolating the errors attributable to specific reconstruction shortcomings such as missing mullions and curved boundaries would be among the first steps toward remedies in future work.

Additionally, mullions—vertical or horizontal dividers within window frames—are not reconstructed. Their absence can lead to overestimated daylight entry areas and thus to higher simulated illuminance values. Similarly, the algorithm does not detect co-planar subsurfaces. In cases where surfaces share a plane but differ in material or reflectance (e.g., partially painted walls or embedded panels), users must manually define these areas if they significantly influence daylight distribution.

Furthermore, some other architectural elements, such as beams and columns, are not reconstructed. This choice aligns with the pipeline's focus on watertight room enclosures, but in rooms where such features obstruct light near window levels or cast prominent shadows, their absence may result in noticeable simulation errors. If such features are expected to affect daylight performance significantly, an additional manual modelling step may be necessary.

Besides, the current approach has been validated on individual, single-room point clouds. Its scalability to more complex configurations, such as multi-room layouts or multi-story buildings, remains untested.

Moreover, although a total modelling time of under 5 minutes is observed on one test machine, a formal timing study or a multi-user sensitivity analysis is not conducted to assess stability across users. This can be done by asking multiple users repeat the wall/window selection on identical scans and compare results to the manual ground truth using geometric error metrics (*e.g.*, Chamfer Distance, Hausdorff Distance) to establish expected error bounds and the variance attributable to user input.

Another limitation is that the algorithm does not detect co-planar subsurfaces. In spaces where surfaces share the same geometric plane but differ in material properties or reflectance—such as partially painted walls or embedded panels—this limitation may lead to inaccuracies in simulation. Users must manually define such subsurfaces if the reflectance contrast is expected to influence the daylight distribution significantly.

Lastly, in this work, points lying outside the target room were removed manually during preprocessing. While this is not always a strict input requirement–for instance, when acquisition already isolates the room or the reconstruction tolerates outliers–automating the room-isolation step would further reduce user effort and improve repeatability. The development and evaluation of such routines are left to future work.

4.6 Conclusion

In this chapter, a semi-automatic pipeline for reconstructing indoor geometries is presented, primarily aimed for CBDM. The method focuses on generating GLoD0 models, which represent the window-containing watertight enclosure of indoor spaces with reduced manual effort. The pipeline includes three main steps, *i.e.*, (1) preprocessing, (2) reconstruction of watertight surfaces, and (3) adding regularized window boundaries through reduced user interaction. This pipeline reduces the processing time to generate indoor geometry for daylight simulations significantly.

The reconstruction approach was evaluated across four rooms of varying complexity. Results demonstrate that the reconstructed models yield daylight availability and glare outcomes with promising accuracy for many applications: sDA shows less than 5% bias, ASE remains within 6%, and TAI stays below 16% relative bias across all cases. Although UDI shows larger deviations (up to 39%) due to its binning logic, glare predictions remain consistent, with DGP RMSE below 0.04. These findings confirm that the pipeline captures the dominant daylight-driving geometrical features despite geometric simplifications and assumptions.

Nevertheless, limitations remain. The method is constrained to planar surfaces, does not reconstruct mullions or co-planar subsurfaces, and has not been validated on multi-room configurations. While these constraints limit its stand-alone applicability in some cases, the approach can serve as an efficient initial step for global analysis. It enables rapid generation of baseline models, which can subsequently be refined using more detailed methods when higher accuracy is required.

Introduction		
RQ1	How sensitive are CBDM results to geometric levels of detail?	Chapter 2
RQ2	What are the uncertainties caused by inaccurate material definition in CBDM results?	Chapter 3
RQ3	How can indoor geometries be efficiently reconstructed to meet the requirements of daylight simulation models?	Chapter 4
RQ4	**To what extent can image-based material characterisation techniques be applied to simulated indoor daylight models?**	**Chapter 5**
RQ5	How can simulated spectral indoor models be calibrated to account for uncertainties in scene reconstruction?	Chapter 6
Conclusion		

5 Characterisation of material optical properties

ABSTRACT

This chapter investigates the potential for automating the on-site material characterisation and reducing its cost for both photopic and for spectral simulations. Three image-based techniques are evaluated for on-site material reflectance characterisation in daylight simulations: (1) Illuminance-Proxy, (2) Ferwerda's phone-based method, and (3) Luo's learned Spatially variant bidirectional reflectance distribution function (SVBRDF) estimation, and validates a spectral uplifting approach for non-visual simulations. A meeting room with diverse material finishes was measured using a reflectance spectrophotometer as the ground truth. The Illuminance-Proxy reconstructs wall reflectance maps from High Dynamic Range (HDR) luminance and sparse reference points; the other two techniques estimate tristimulus reflectance from phone images. Accuracy is reported with Mean Relative Bias (MRB), Root Mean Squared Relative Error (RMSRE), ΔE_{ab}, and room-scale metrics of daylight availability and visual comfort, *i.e.,* Total Annual Illumination (TAI), Useful Daylight Illuminance (UDI), and Daylight Glare Probability (DGP). For on-site photopic use, Ferwerda's method offers the best balance of accuracy and practicality. It relies only on a phone image, maintains stable performance across lighting conditions, and shows the lowest errors. Illuminance-Proxy is effective when calibrated HDR images and sparse reference points are available; it provides spatial reflectance maps and showed good per-point agreement in the 3-channel test, though it over predicted TAI by about 101%. Luo's learned SVBRDF estimation was least reliable, with the highest reflectance and colour errors and TAI overestimation up to 134%. All methods predicted low DGP values with negligible error. Spectral uplifting is shown reconstruct smooth, energy-conserving spectra with wavelength-wise relative errors of $< 20\%$ across all wavelengths and in Melanopic equivalent daylight illuminance (m-EDI) errors of $< 6\%$.

This chapter is currently under review: Forouzandeh, N., Nan, L., Stoter, J., Kim, D., & Brembilla, E. (2025). *Image-based characterisation of material optical properties for indoor daylight simulation*. Also it is partly

published in the conference paper: Forouzandeh Shahraki, N., Brembilla, E., & Jakubiec, J. A. (2022). *Image-based material characterisation for daylight simulation using illuminance-proxy and artificial neural networks*. In *Proceedings of the 14th European Lighting Conference (LUX EUROPA 2022)*, pp. 171–178.

5.1 Introduction

Optical properties of materials are among the key inputs for modelling daylight and lighting in buildings. A minimal definition of material optical properties in a typical indoor daylight availability and visual comfort project includes only diffuse reflectance, also known as Lambertian reflectance, which assumes the material has fully diffusing properties. Common techniques and workflows for material chatacterisation include:

- **Reflectance spectrophotometers**: These are the most accurate tools, as they are capable of measuring both diffuse and specular reflectance components spectrally.
- **Average Hemispherical Reflectance (AHR)**: This technique estimates the overall visible reflectance value, represented as a value in the range of 0 to 1. This approach relies on the synchronous measurement of illuminance falling onto a surface and the luminance reflected from it, followed by the application of Eq. 5.1, which relates reflectance to these two quantities. A key assumption of this method is that the surface behaves as a purely diffuse reflector.

$$\rho = \frac{(L * \pi)}{E} \tag{5.1}$$

- **User selection from measured datasets**: Another widely used method involves characterising the optical properties of a surface based on describing its semantics and colour, using a database of measured material information. An example of such a database is *Spectral DB*, which includes a large and regularly updated library of materials (Jakubiec, 2022). Unlike the previous two methods, this approach provides additional parameters such as specularity, spectral reflectance, and human-estimated roughness that makes it more complete to use in realistic simulations.
- **Colour charts**: This method offers a practical, albeit less precise, alternative. It involves matching the surface in question with the closest colour that has known optical properties. Two commonly used charts are the RAL K5 and the Chartered Institution of Building Services Engineers (CIBSE) colour chart. For RAL K5, both colour information and reflectance properties for each colour card are available on the *Radiance* website (Radiance, 2022). The CIBSE chart also provides reflectance

values for each colour, which makes it suitable for physically based daylight simulations.

Each of these techniques comes with one or more limitations that can affect their practicality and accuracy in real-world applications. Reflectance spectrophotometers, although highly accurate, involve high equipment costs and often require specialized training and setup. AHR is more accessible but can be time-consuming due to the need for precise, repeated measurements, and having luminance and illuminance metres is necessary. Database-driven approaches, such as picking an entry from *SpectralDB*, depend on the availability of a closely matching material and are sensitive to the user's choice. The same limitation applies to the colour chart technique in cases where the user has reduced colour sensitivity, such as being colour blind.

These limitations highlight the need for low-cost, lightweight, objective, and scalable alternatives. Using images can potentially resolve all these issues, given the wide availability of cameras. Several studies, both in built-environment research and computer graphics, address this topic. These works are reviewed in Section 5.2.

The three selected techniques therefore aim to estimate visible or tristimulus reflectance from images and are applied to daylight evaluations in real rooms. For hyper-spectral renderings and for studying the non-visual impacts of light, however, a spectral definition of material optical properties is necessary. Techniques to reconstruct spectra from tristimulus information are also reviewed in the next section.

Based on this literature, this chapter contributes in four ways: (1) it applies three image-based techniques in real rooms and compares them directly with spectrophotometer ground truth; (2) it reports the performance of Ferwerda's technique and its sensitivity to different lighting conditions under which the photos are captured; (3) it extends the illuminance-proxy from single-channel to three-channel calibrated High Dynamic Range (HDR) and quantifies how sample-level errors propagate to room-scale Total Annual Illumination (TAI), Useful Daylight Illuminance (UDI), and Daylight Glare Probability (DGP); and (4) it validates spectral uplifting against measured spectra and quantifies its effect on Melanopic equivalent daylight illuminance (m-EDI) in spectral simulations.

In Section 5.3, the methodology is described, including the case study room, the ground truth spectrophotometer measurements, and the implementation details of each image-based technique. In Section 5.4, the results are reported in three parts: first, the estimation of visible and tristimulus reflectance from images; second, the reconstruction of spectral reflectance through uplifting and its implications for non-visual daylight simulations; and third, the impact of the different techniques on daylight availability and glare performance at the room scale. The discussion of findings and their implications is presented in Section 5.5, followed by the conclusions in Section 5.6.

5.2 Literature review

Estimation of material properties is well established under lab settings. For existing buildings, however, a portable setup and lightweight techniques are needed. Bodart et al. (2008) compare four material characterisation techniques for in-situ daylighting evaluation: (1) AHR, (2) using a colorimeter (PerkinElmer Lambda 900 UV-VIS-NIR), (3) a luminance-based measuring technique involving reference cards (ENTPE), and (4) CIBSE colour charts. Their study shows that AHR provides the most accurate estimation of hemispherical reflectance after the colorimeter.

Beyond traditional in-situ methods, computer graphics and vision communities have explored a range of image-based approaches to infer material properties, often under more constrained or synthetic settings. Images are formed by four primary components: (1) view, (2) lighting conditions, (3) surface shape, and (4) reflectance properties, known as the image formation model (Luo et al., 2024). In building settings, where surface shapes are often known and approximately planar, estimating material properties remains underdetermined due to unknown or variable illumination. This contrasts with laboratory conditions, where controlled lighting and fixed setups enable accurate material characterisation (Naik et al., 2011; Chandraker and Ramamoorthi, 2011; Yoo et al., 2009; Zhang et al., 2017).

Mardaljevic, Brembilla, and Drosou estimate pixel-wise illuminance given sparse hemispherical reflectance points on an HDR image (Mardaljevic et al., 2015). They use Kriging interpolation to generate an illumination map. By rearranging the reflectance-illumination equation, they estimate a pixel-wise hemispherical reflectance of wall areas. Since this approach requires only a few known reflectance values per surface, it can reduce fieldwork while still producing high-resolution reflectance maps. Their technique is tested on single-channel HDR images and is extended to multi-channel HDR images as described in Section 5.3.1.2.

Ferwerda proposes a more lightweight technique using only an image captured by a phone (Ferwerda, 2018). Tristimulus hemispherical reflectance is estimated via two main steps: gamma correction and chromatic adaptation. Gamma correction aims to decode the non-linearity applied to brightness and pixel values. This is to compensate for the non-linear way that displays and imaging devices represent and process light, making the displayed image appear more natural and consistent with human perception. The aim of chromatic adaptation is to convert the reference white point of the phone to an equal energy output for consistency with the *Radiance* colour framework.

In contrast to these rule-based techniques, which rely on predefined assumptions about illumination and geometry, various studies in computer graphics aim to use learning algorithms to derive these priors from large synthetic datasets. A review of such data-driven techniques is presented by Kavoosighafi et al. (2024). A recent

algorithm of this type was proposed by Luo et al. (2024) and estimates Spatially variant bidirectional reflectance distribution function (SVBRDF) for planar surfaces. This network uses an architecture built on U-Net by Deschaintre et al. (2018). With this method, the input is the difference of initial predictions and the ground truth and is fed to three convolutional layers and two gated recurrent units. The first two convolutional layers use leaky ReLU and a hyperbolic tangent activation function. The output is used as input for the same architecture, and this process is repeated 6 times. Like many similar works, this technique is not validated against real measurements but against graphical datasets. This will be presented in 5.4.1.

In addition to colour characterisation, material spectral properties are used for hyper-spectral renderings and for studying the Non-image forming (NIF) effects of light in buildings. With the above techniques, it is feasible to characterise tristimulus but not the entire spectrum. Spectral uplifting is the process of converting tristimulus colour representations, like Red, Green, Blue (RGB), into higher-dimensional spectral representations. This is important for physically based rendering techniques and is particularly applied for modelling metamerism, the phenomenon where distinct spectra produce the same colour under a specific illumination. One approach to spectral uplifting is proposed by Jakob and Hanika (2019), which is based on the observation that the reflectance spectra of absorbing surfaces tend to be smooth functions in the visible light range and can be approximated by a low-dimensional parametric model. In a sigmoidal space, this method converts textures with tristimulus values into spectral reflectance data. The underlying assumption is that suitable reflectance spectra can be represented by a low-dimensional parametric model that is both smooth and energy-conserving.

In this chapter, the accuracy of three image-based material characterisation techniques is studied, namely illuminance-proxy and Ferwerda's, as well as a data-driven image-based SVBRDF estimation developed by Luo et al. (Luo et al., 2024). Furthermore, the uplifting technique proposed by Jakob and Hanika is validated against real-world measurements, and the resulting errors in spectral simulations are calculated.

5.3 Methodology

The studied room is a 5.8 m by 4.3 m meeting room located at the Faculty of Architecture in Delft, The Netherlands. The room is oriented towards North-West at a 45-degree angle from due South. Pictures from the room are presented in Fig. 5.1. This room was chosen due to its variety of material properties, consisting of red carpet flooring, blue-painted plaster, brown brick, white plaster, and grey-painted doors, with furniture of different colours. Electric lighting is provided by warm white

light-emitting diode (LED) lamps.

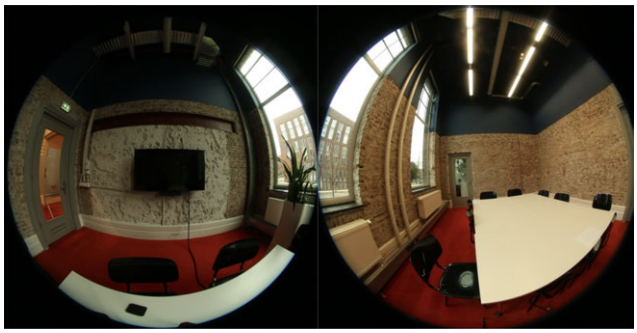

FIG. 5.1 Case study room as seen with a fisheye camera from two points and two directions.

5.3.1 Material data collection

5.3.1.1 Ground truth

Each surface was measured using a Konica Minolta CM-26dG spectrophotometer, following a standard measurement protocol that began with both zero and white calibration. For each material, measurements were taken in two modes: with the Specular component included (SCI) and with the Specular component excluded (SCE). The SCI mode captures both diffuse and specular reflectance, representing how the material appears under directional illumination. In contrast, the SCE mode suppresses the specular highlight, thus isolating the diffuse reflectance characteristics of the surface. This distinction is particularly important for materials with glossy or semi-glossy finishes, as it influences the resulting reflectance spectra and their interpretation in daylight simulations.

To process the raw output from the spectrophotometer, a script was developed. This script reads the exported files from the Konica Minolta CM-26dG and extracts the reflectance spectra for each sample under both SCI and SCE conditions. The instrument provides reflectance values across the 360–740 nm range at 10 nm intervals, reported in percentage. These values are parsed, converted to floating-point format, and re-indexed by wavelength.

For each material, both SCI and SCE spectra were extracted and converted to RGB values using the Commission Internationale de l'Éclairage (CIE) 1931 2° standard colorimetric observer under a D65 illuminant. The observer is defined in for Standardization (ISO), which provides the colour-matching functions $\overline{x}(\lambda)$, $\overline{y}(\lambda)$, and $\overline{z}(\lambda)$. The $\overline{y}(\lambda)$ function represents the photopic luminous efficiency of the human eye

and is proportional to the perceived luminance. Using these weighting functions, the spectral data were integrated to obtain the tristimulus values and converted to RGB components under the D65 reference illuminant.

The RGB values were then used to compute the visible reflectance using Eq. 5.2, which expresses the luminance-weighted combination of the three channels following the CIE 1931 photopic luminous efficiency function. The coefficients are derived from the relative contribution of the red, green, and blue components.

$$R_{\text{vis}} = 0.265 \cdot R + 0.670 \cdot G + 0.065 \cdot B \tag{5.2}$$

This provided a scalar approximation of visible reflectance for each mode. Specularity was computed as the difference between SCI and SCE visible reflectance.

FIG. 5.2 Ground-truth measurement setup: reflectance spectrophotometer and its calibration module.

5.3.1.2 Illuminance proxy

With this technique, HDR images of five main surfaces, *i.e.*, four walls and the ceiling, were captured. A list of sparse points of known reflectance values, measured with the AHR method, was created. A mask indicating the area of interest for all unique materials in each HDR image was created as the third input of this method. In Fig. 5.3, these inputs for calculating the mean reflectance in one of the walls are visualized. Knowing the luminance and reflectance, an illuminance map is generated. The resulting list of illuminance values and their pixel location is then fed into a Kriging interpolation algorithm, as previously proposed by Mardaljevic et al. (2021). The final hemispherical reflectance for the whole wall is calculated as an average of pixel

values for each separate mask with a unique material. An example set of masks for one of the walls is presented in Fig. 5.4.

The resulting illuminance map and the input luminance map are used to generate the reflectance map. Finally, the reflectance is calculated by averaging the pixel-wise reflectance values across the areas of interest, indicated by separate masks, *e.g.*, brick parts and plinth. An additional outlier removal step, which includes the removal of 0-5th and 95-100th percentiles is applied to the list of output reflectance values for one of the surfaces (*wall 3*). This was only done on this wall because it did not significantly change the result on other surfaces (less than 5%). Specularity and roughness are assumed to be zero in this characterisation scenario. For the definition of the floor, the ground truth reflectance is used when performing the daylight simulation comparison, since it was not possible to capture a full image of the floor.

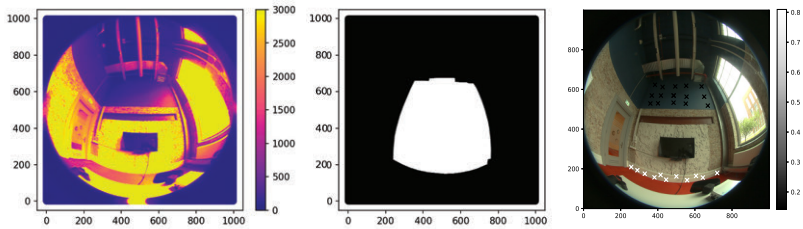

FIG. 5.3 Inputs for the illuminance-proxy method. From left to right: luminance map [cd/m^2], example mask indicating the area of interest for the whole wall, spots of known reflectance

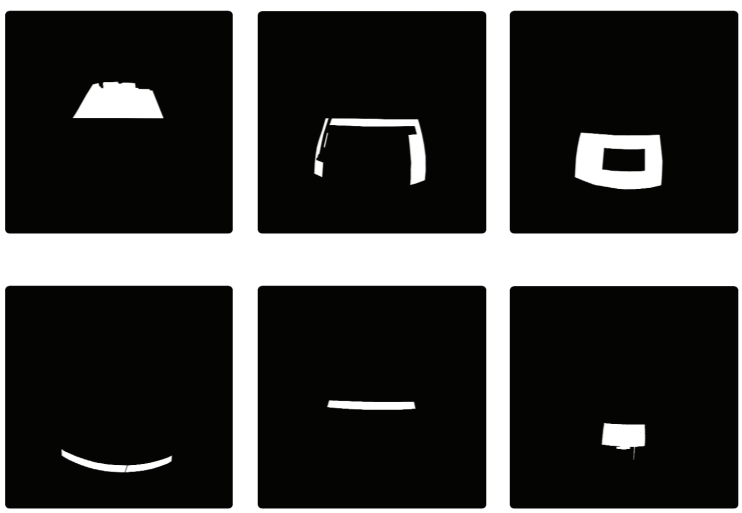

FIG. 5.4 Masks with a unique material for an example wall.

At the time of measuring the known reflectance points in the room, an accurate reflectance spectrophotometer was lacking. Therefore, the AHR technique was implemented using paired luminance and illuminance measurements. This potentially introduces some error to the result of the illuminance-proxy technique, which was initially applied only to visible reflectance without considering colours, again due to limitations with the available instrumentation (single channel HDR imaging camera). To address these gaps, the technique was later applied to a three-channel HDR image of a different test scene. First, a sample with brown and yellow spots on white paper—similar to the illuminance-proxy setup—was printed and measured using a reflectance spectrophotometer. The sample was then sent to the LIPID lab for HDR image captures, equipped with the 3-channel calibrated HDR camera calibrated by LMK (Fig. 5.5 and Fig. 5.6). The ground truth properties of the white, yellow, and brown regions were thus obtained, and the rest of the process repeated the single-channel illuminance-proxy steps for three data series (RGB) instead of one.

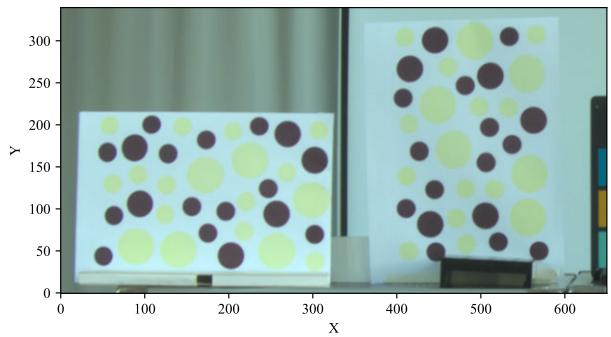

FIG. 5.5 Input HDR for three-channel illuminance-proxy. Courtesy of Dong Hyun Kim, captured at LIPID lab, EPFL, 2024.

5.3.1.3 Luo's method

Material capture using Luo's method was performed with an iPhone 12 under controlled conditions required for this technique. All samples were photographed with only the phone's built-in flash as the illumination source. To isolate the flash light and block ambient illumination, a custom phone cap was designed and 3D printed. The inner surface of the cap was coated with three layers of Musou Black paint (Koyo Orient Japan Co., Ltd.), which has an absorptivity of 99.4%, applied in three layers with two primer layers in between, to minimize internal reflections. This configuration is shown in Fig. 5.7.

The original paper does not explicitly recommend using an optical shield such as the

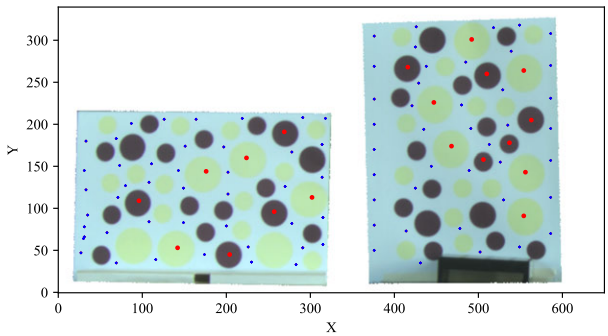

FIG. 5.6 Input region and points of interest for three channel illuminance proxy, blue diamonds are the points with known reflectance, red dots are the points of interest.

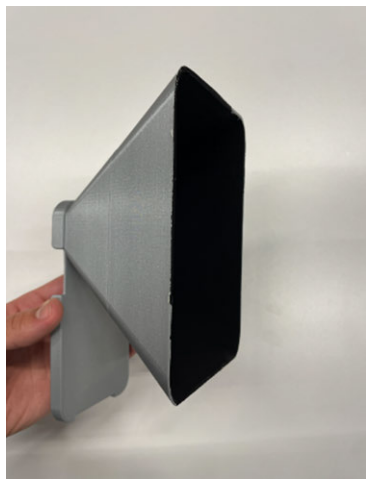

FIG. 5.7 Phone cap to block ambient light and prevent inter-reflections.

3D-printed cap; however, the controlled setup was designed to ensure consistency across samples and to replicate the lighting conditions under which the synthetic training data was made. Images were preprocessed by centre-cropping, resizing, and then passed to the pre-trained model published by the author. The output was a single image of size 1024×256 pixels, structured as four 256×256 sub-images corresponding to diffuse reflectance, specular reflectance, surface roughness, and normal maps, respectively, as shown in Fig. 5.8.

The diffuse mean RGB values were compared to the ground truth values obtained from spectrophotometer measurements. The CIE ΔE_{ab} metric was computed between the ground truth and estimated values as the colour difference metric.

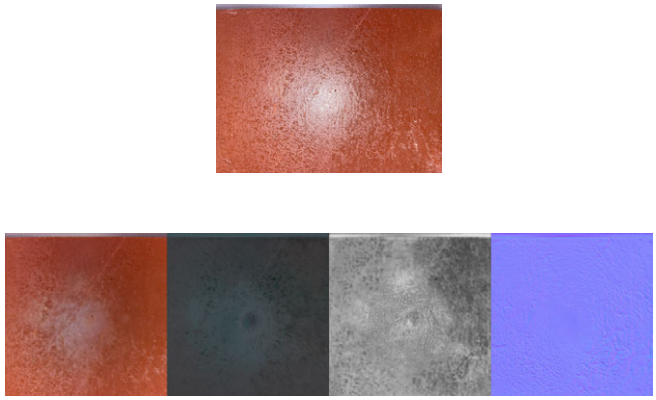

FIG. 5.8 An example original input image (left) and output from Luo's method (right), consisting of diffuse reflectance, specular component, roughness, and normal maps.

5.3.1.4 Ferwerda's method

This method takes a phone image taken under any illumination as its input. The samples were captured with the same iPhone 12, without flash, at 13:30 on the afternoon of 17 March 2025, under a clear sky. The exposure was set to auto, and the photo was taken 10–40 cm from the surfaces. To study the influence of different lighting conditions on its performance, photos of samples are captured under four different lighting conditions (see Fig. 5.9), namely (1) daylight, (2) electric lighting, (3) mixed daylight and electric, and (4) using the cap as shown in Fig. 5.7.

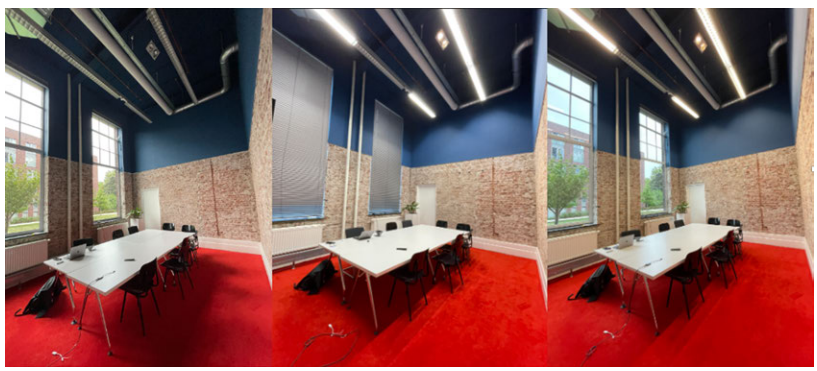

FIG. 5.9 Different lighting conditions for testing Ferwerda's technique: daylight only (left), electric lighting only (middle), and mixed daylight and electric lighting (right).

5.3.1.5 Spectral uplifting

As a separate analysis, following the comparison between methods to measure visible reflectance, a spectral uplifting procedure is implemented to obtain material spectral reflectance in the visible range from RGB data. As a reference, 801 samples were collected from the SpectralDB dataset (Jakubiec, 2022), representing materials in the built environment. These samples were from different surface types in that dataset, including *Ceiling*, *Door*, *Exterior*, *Exterior Building*, *Exterior Floor*, *Floor*, *Furniture*, *PV*, *Plant*, *Wall*, and *Window Mullion*.

First, the tristimulus data from the ground truth spectrum was extracted. This data was used as input for implementing Jakob and Hanika's technique for the uplifting (Jakob and Hanika, 2019). The overall performance was then calculated in terms of both Root Mean Squared Relative Error (RMSRE) and Mean Relative Bias (MRB) across different wavelengths.

To quantify the impact of uplifting errors on simulated Melanopic equivalent daylight illuminance (m-EDI) values, a seated head-pose m-EDI as shown in Fig. 5.10 was simulated using Radiance v6.0 with both ground truth and uplifted spectral properties in room WBG640 at four time steps near the summer solstice, with two fully overcast time steps and two clear sky ones. The ground truth material is picked from the *SpectralDB* based on the surface type and colour. The input for the uplifted spectrum was the tristimulus extracted from that original spectral colour. The Diffuse Horizontal Irradiance (DHI) and Direct Normal Irradiance (DNI) values are picked from representative climate data from Crawley and Lawrie (2019)[1], followed by the application of a luminous efficacy model proposed by Perez et al. (1990).

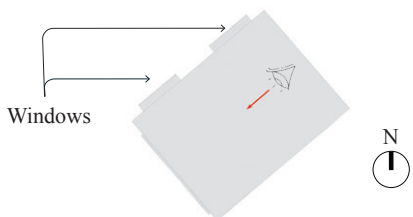

FIG. 5.10 Selected view for spectral simulation, same case study room as for previous analyses.

5.3.2 Performance evaluation

When comparing the reflectance estimation methods (illuminance-proxy, Ferwerda, and Luo), in addition to the range of reflectance difference ($\Delta\rho$) for each sample, the

[1] NLD_ZH_Rotterdam.The.Hague.AP.063440_TMYx.2009-2023

TABLE 5.1 DNI, DHI, Global Horizontal Irradiance (GHI), Direct Normal Illuminance (DNE), and Diffuse Horizontal Illuminance (DHE) values for the Summer solstice (June 21) at three times of day, used in the spectral simulations.

Date and time	DNI [W/m^2]	DHI [W/m^2]	GHI [W/m^2]	DNE [lx]	DHE [lx]
21 June – 13:00	636	307	866	62863	37364
21 June – 14:00	659	295	866	63774	36234
22 June – 09:00	0	155	155	0	17897
22 June – 11:00	1	240	241	101	28321

overall error magnitude and bias are represented by RMSRE and MRB respectively, as shown in Eq. 5.3 and Eq. 5.4.

$$\mathrm{RMSRE} = \sqrt{\frac{1}{N}\sum_{i=1}^{n}\left(\frac{X_{i,\mathrm{meth}} - X_{i,\mathrm{ref}}}{X_{i,\mathrm{ref}}}\right)^2} \tag{5.3}$$

$$\mathrm{MRB} = \frac{1}{N}\sum_{i=1}^{n}\left(\frac{X_{i,\mathrm{meth}} - X_{i,\mathrm{ref}}}{X_{i,\mathrm{ref}}}\right) \tag{5.4}$$

where:

- N is the number of samples,
- $X_{i,\mathrm{meth}}$ is the value from the method under evaluation for sample i,
- $X_{i,\mathrm{ref}}$ is the corresponding reference value for sample i.

Luo and Ferwerda's methods also estimate colour information. For these techniques, the error is represented also by ΔE_{ab} and absolute differences in RGB channel values. ΔE_{ab} indicates a colour difference in the $L^*a^*b^*$ colour space and is calculated as shown in Eq. 5.5. In theory, ΔE_{ab} is non-negative and unbounded above ($\Delta E_{ab} = 0$ means identical colours, and larger values indicate larger differences). If the $L^*a^*b^*$ values are constrained to the typical 8-bit encoding ($L^* \in [0, 100],\ a^*, b^* \in [-128, 127]$), the maximum possible ΔE_{ab} would be $\sqrt{(100)^2 + (255)^2 + (255)^2} \approx 374.2$. In practice, only Ferwerda's work reports ΔE_{ab} values. In their experiments, the observed range was 0–22, which is used here to compare the performance of the new techniques to those in Ferwerda's measurements.

$$\Delta E_{ab} = \sqrt{L^2 + a^2 + b^2}. \tag{5.5}$$

On the room level, the techniques are compared in terms of work-plane Total Annual Illumination (TAI) and Daylight Glare Probability (DGP) on a sitting view on 9 time steps at 9:00, 12:00, and 15:00 on an equinox and the solstices.

5.4 Results

The results are presented in three sections. The comparison between the three image-based techniques to estimate reflectance and colour is presented in section 5.4.1. The spectral uplifting from tristimulus information and its application in non-visual daylight simulations are presented in Section 5.4.2. Last, the impact of the reflectance-estimating techniques on room-level visible daylight evaluations is presented in section 5.4.3.

5.4.1 Tristimulus and reflectance estimations

Input HDR images, luminance maps, and reflectance maps for illuminance-proxy for a single channel applied on the use case room are shown in Table 5.2. The reflectance difference ($\Delta\rho$) for the single channel Illuminance-proxy in the use-case room, which is calculated as the average pixel value across separate regions–as shown in Fig. 5.4 for a single wall–ranges from 0.03 to 0.82.

The validity of the illuminance-proxy method is further tested with a calibrated three-channel HDR from Digital Single-lens Reflex [camera] (DSLR) camera. The resulting errors from a test scene and target points are shown in Fig. 5.11 and Fig. 5.12. The results indicate a reflectance difference ($\Delta\rho$) of less than 8% and an error of between 1% and 11% in RGB channels and across the 19 query points. Errors from the blue channel are more pronounced (2%–11%) than errors in the green (1%–9%) and red (0–4%) channels. The actual RGB values for all the target points are listed in Appendix E.

For Ferwerda's method, $\Delta\rho$ ranges from 0.05 to 0.49, while ΔEab—an indicator of colour differences—varies between 4 and 56. These values exceed the colour differences reported in Ferwerda's original work, which were between 12 and 22 on sample cards. For the Luo technique, $\Delta\rho$ spans 0.02 to 0.48, and ΔEab ranges from 4 to 62 (see Fig. 5.13 and Fig. 5.14). As shown in Fig. 5.13, Luo's method—and, to some extent, Ferwerda's—struggles to estimate higher reflectance values. The same figure also includes the results of the single-channel illuminance-proxy applied in the

TABLE 5.2 Interpolated illuminance map, reflectance map, and mean reflectance for five main surfaces of the studied room

Name	HDR map [cd/m²]	Illuminance map [lx]	ρ map [0-1]	ρ_{mean}
Wall1	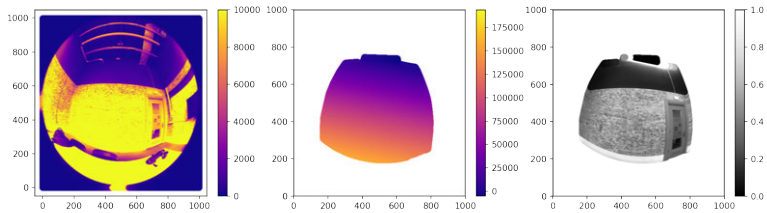			0.481
Wall2	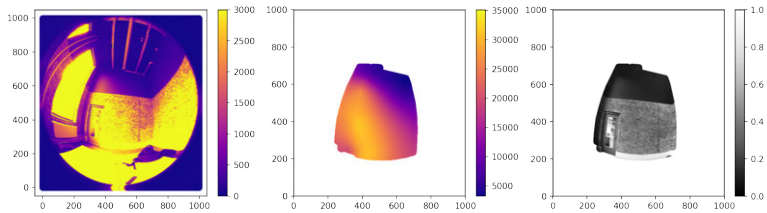			0.361
Wall3	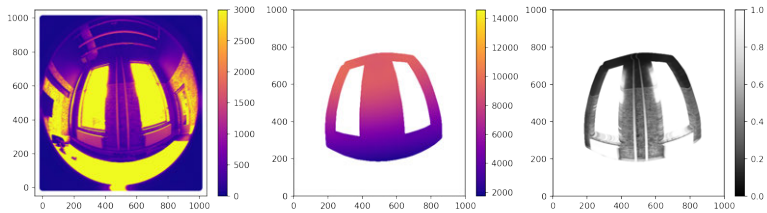			0.42
Wall4	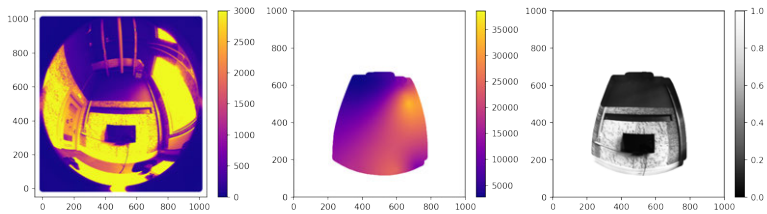			0.44
Ceiling	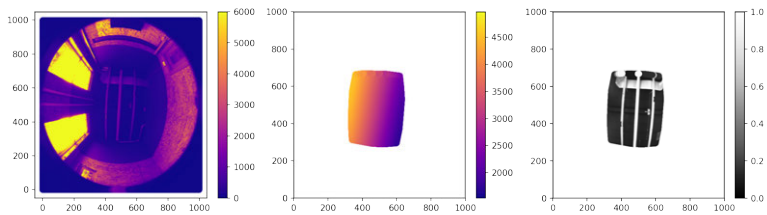			0.36

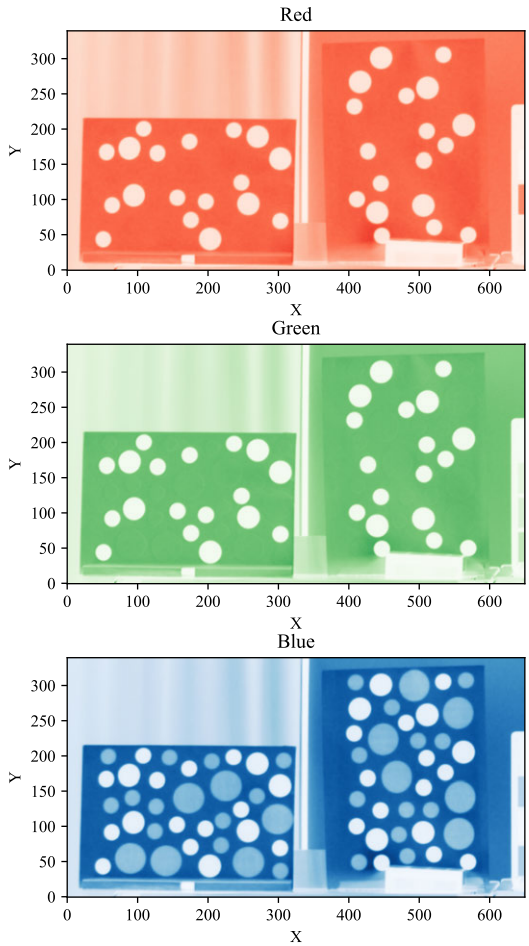

FIG. 5.11 Output reflectance map from three channel illuminance-proxy.

case-study room, which captures a wider range of values but exhibits the largest error at very low reflectances. Finally, the MRB and RMSRE for all three techniques in the case-study room are summarised in Table 5.3.

TABLE 5.3 Overall performance of illuminance-proxy, Ferwerda, and Luo for estimation of visible reflectance.

	Illuminance-proxy	Ferwerda	Luo
MRB [%]	18.75	13.06	25.16
RMSRE [%]	41.26	31.13	61.69

The sensitivity of Ferwerda's performance to differences in lighting conditions under which the images are captured is further assessed. The MRB and RMSRE are stable

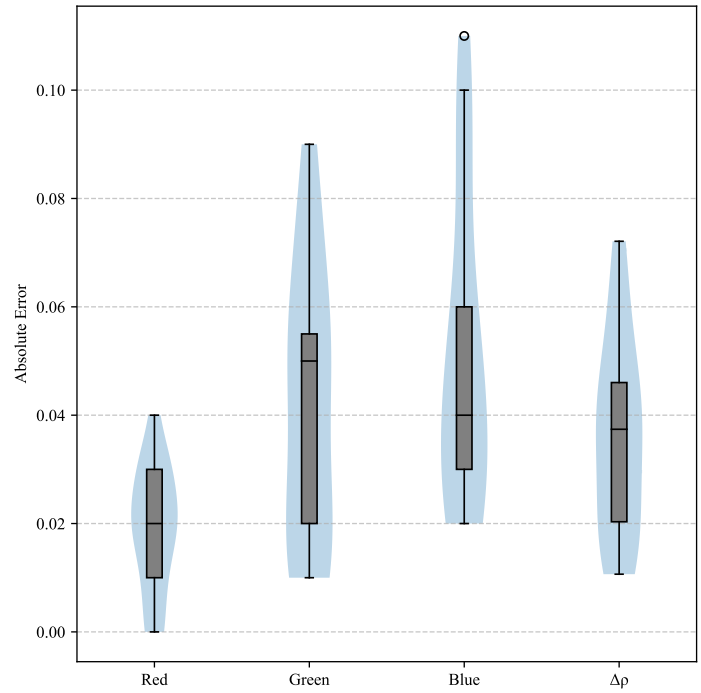

FIG. 5.12 Absolute RGB error values for 19 query points across the two samples for the three-channel illuminance-proxy.

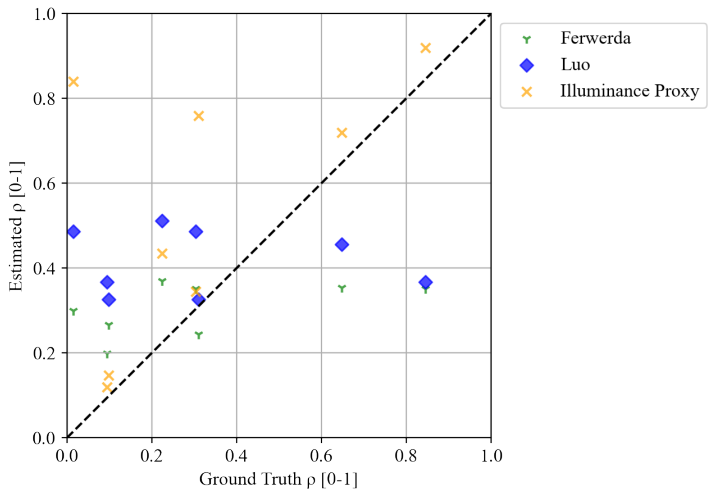

FIG. 5.13 Comparison of visible reflectance for Luo, Ferwerda, and illuminance-proxy.

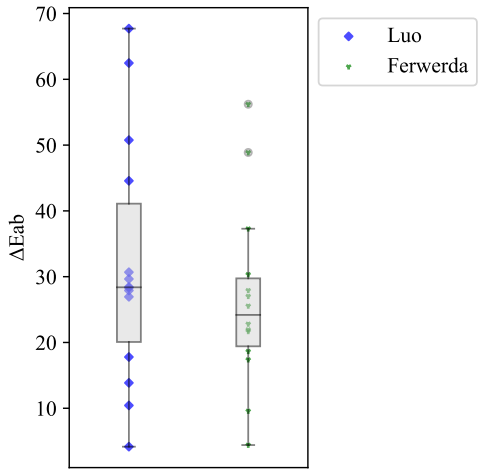

FIG. 5.14 Colour differences with ground truth in terms of ΔEab for Luo and Ferwerda.

and are in ranges of 12.46-15.66 and 30.78-37.98, respectively (Table 5.4). Median ΔEab ranges from 18 to 27 as illustrated in Fig. 5.15.

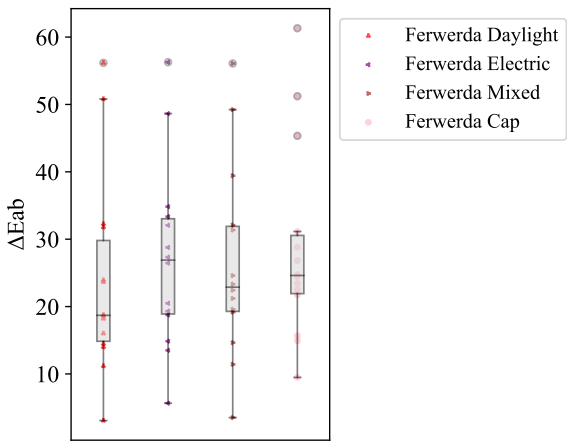

FIG. 5.15 Colour differences with ground truth in terms of ΔEab for Ferwerda's technique under different lighting conditions.

TABLE 5.4 Overall performance of Ferwerda's technique under different lighting conditions.

	Daylight	Electric	Mixed	Cap
MRB	12.46	12.63	12.96	15.66
RMSRE	30.89	30.78	30.95	37.98

5.4.2 Impact on daylight availability and visual comfort

The rendered images of the case study room using each of the three techniques are shown in Fig. 5.16, and those obtained with Ferwerda's method under different lighting conditions are presented in Fig. 5.17. In these renderings, the illuminance-proxy technique appears in black and white, as it operates on reflectance rather than separate RGB channels, in contrast to Luo and Ferwerda. Despite this, the luminance contrast in the Illuminance-proxy render closely resembles that of the ground truth.

Across all renderings, the red beam is consistently identified. However, the blue wall and ceiling surfaces are not clearly represented in Luo's technique and in Ferwerda's method under electric lighting. Highly specular black elements, such as the chairs and the screen, are subject to significant errors in all techniques. Notably, only Ferwerda's method under daylight conditions succeeds in accurately reproducing the black surfaces.

The white desk is characterised by variable reflectance levels across the techniques; however, it consistently appears greyish, similar in tone to the white plaster wall. The brick wall is rendered as beige in both Luo and Ferwerda, regardless of lighting conditions.

All three techniques show over-prediction of TAI, with percentage errors of 65%, 101%, and 133% for Ferwerda, Illuminance-proxy, and Luo, respectively (Table 5.5). The UDI results indicate that both Ferwerda and Illuminance-proxy predict (UDI_a) with an error of within 16%, whereas Luo produces the largest deviation, with $\Delta UDI_a = 16\%$ compared to the ground truth.

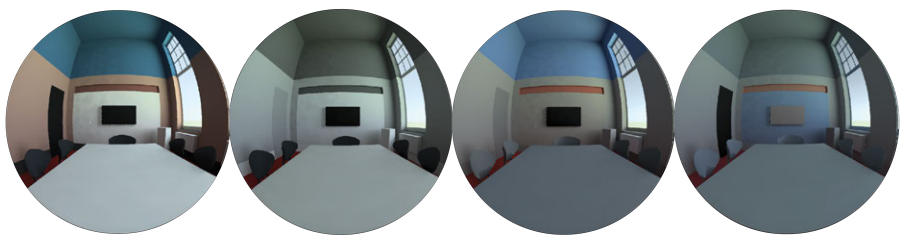

FIG. 5.16 A rendered view of the case study room with the four set of material properties from left to right: ground truth, illuminance-proxy, Ferwerda's, and Luo's.

The TAI percentage errors for Ferwerda's technique under different lighting conditions range between 33-57%, with the flash lighting under cap resulting in the smallest error, and mixed electric and daylighting conditions resulting in the highest error.

Comparison of DGP values for solstices and an equinox for different characterisation scenarios and for different lighting conditions are plotted in Fig. 5.18. These results show a negligible RMSRE error of less than 0.02 across all techniques and daylighting

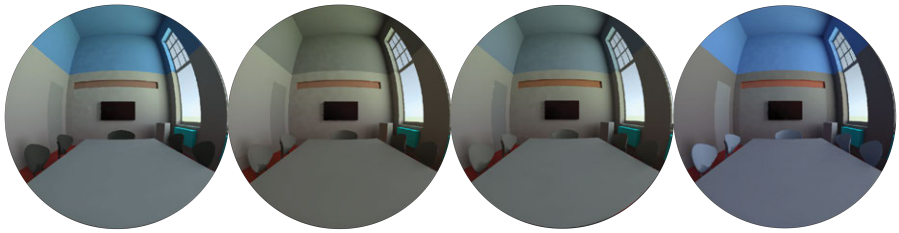

FIG. 5.17 A rendered view of the case study room with materials obtaind from the Ferwerda's technique under different lighting conditions, from left to right: daylight, electric, mixed, and cap.

TABLE 5.5 TAI values and corresponding Percentage Error (PE) for illuminance-proxy, Ferwerda, and Luo in use case room.

	Ground truth	Illuminance -proxy	Ferwerda	Luo
TAI [klx.hr/yr]	635	1279	1051	1495
PE_{TAI}	-	101%	65%	133%
UDI_n	94	84	89	78
UDI_a	5	15	10	21
UDI_e	0.02	0.18	0.07	0.20
Δ_{UDI_a}	-	10	5	16

TABLE 5.6 Overall performance of Ferwerda's technique under different lighting conditions.

	Ground truth	Daylight	Electric	Mixed	Cap
TAI [klx.hr/yr]	641	911	951	1009	853
PE_{TAI}	-	42%	48%	57%	33%

conditions. Note that none of the instances indicate the presence of discomfort glare.

5.4.3 Spectral uplifting

Following the comparison between methods to measure visible and three-channel reflectance, spectral uplifting is implemented to obtain spectral reflectance from RGB (tristimulus) data for non-visual daylight simulations. Fig. 5.19 shows that the MRB is within 20% for all wavelengths, with the two ends of the visible spectrum showing higher errors compared to the middle wavelengths.

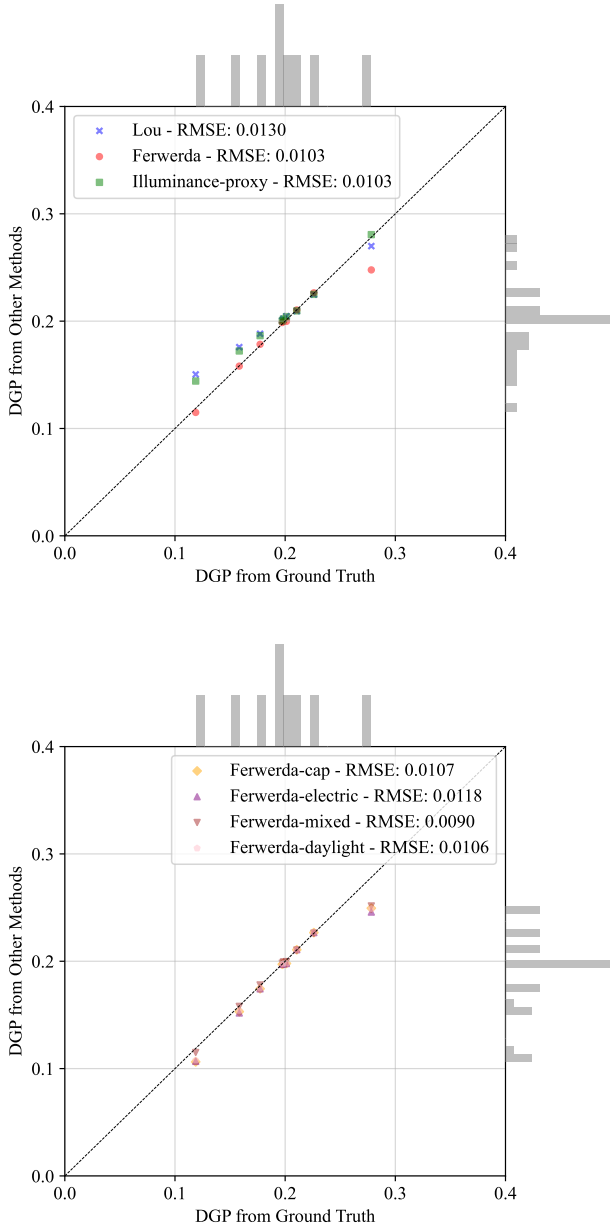

FIG. 5.18 Comparison of different characterisations (top), and influence of different lighting conditions for Ferwerda's method (bottom). The histograms on the top and right sides of the graphs show the frequency of occurring DGP results.

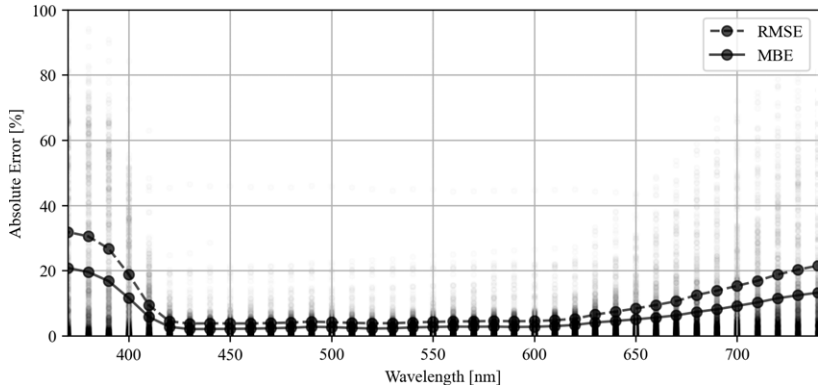

FIG. 5.19 Spectral Absolute Error (AE), RMSRE, and MRB across visible wavelengths for 801 samples.

The simulated m-EDI values for measured ground truth material properties and the uplifted ones are shown in Table 5.7. The differences range from 7 lx on the overcast June 21st at 13:00 to 86 lx on clear sky June 22nd at 11:00. The simulated spectral irradiance received at a vertical viewpoint inside the case study room is illustrated in Fig. 5.20. According to the spectral data, there is an overall predominant over prediction, with an MRB of 0.12 $W/m^2/nm$, and a RMSRE of 2.95% across different wavelengths and time steps.

TABLE 5.7 Simulated m-EDI with measured and uplifted spectral materials.

	Ground truth [lx]	**Uplifted** [lx]	**PE**[%]
June 21st – 13:00	1206	1148	4.8
June 21st – 14:00	1541	1455	5.6
June 22nd – 9:00	491	484	1.4
June 22nd – 11:00	765	748	2.3

5.5 Discussion

Evaluating reflectance estimation errors in terms of MRB and RMSRE as described in Eq. 5.3 and Eq. 5.4 allows comparison with three other techniques previously assessed by Bodart et al. (2008), namely CIBSE sample chart, ENTPE, and AHR. In terms of MRB, the order of techniques from the least to the most accurate one is CIBSE sample chart, Luo, ENTPE, Illuminance-proxy, Ferwerda, and AHR, as presented in Table 5.8. This highlights the potential of the three image-based

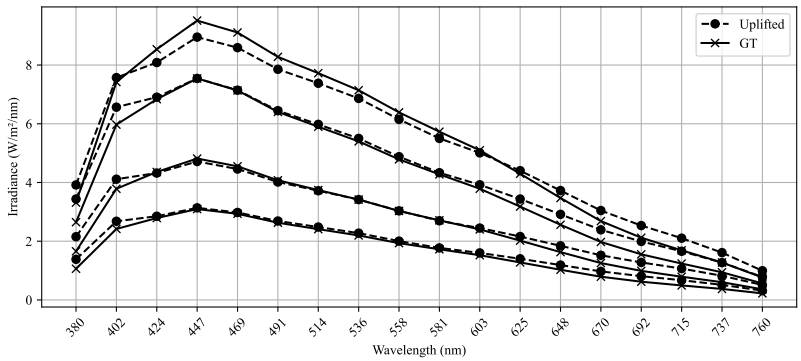

FIG. 5.20 Comparison of spectral irradiance simulated at a fixed viewpoint, using measured and uplifted spectral reflectance as input. From top pair to the bottom one: (1) June 22nd – 11:00, (2) June 22nd – 9:00, (3) June 22nd – 9:00, and (4) June 22nd – 11:00.

techniques.

TABLE 5.8 Comparison of different methods and corresponding MRB and RMSRE values. Results from AHR, ENTPE, and Sample chart are measured by Bodart et al. (2008).

Method	MRB	RMSRE
AHR	0.59	25.69
Ferwerda	13.00	31.00
Illuminance-proxy	18.00	41.00
ENTPE	19.28	36.58
Luo	22.00	54.01
Sample chart	32.00	54.49

In terms of annual daylight availability, the percentage errors on mean TAI are within 133% for Luo, 101% for illuminance-proxy, and 65% for Ferwerda. Ferwerda's technique performs better than others, irrespective of lighting conditions, as presented in Table 5.9. All the techniques have acceptable performance in predicting glare probability caused by daylight for low glare conditions, with RMSRE of less than 0.02 in the resulting DGP values.

Ferwerda and Luo techniques rely solely on smartphone cameras to provide inputs, making them low-cost, accessible, and easy to implement in a wide range of settings without requiring specialized equipment. They provide tristimulus colour estimation, which is useful for analysing the visual aspects of daylight. Despite their accessibility, these techniques demonstrate considerable errors in reflectance estimation, with Luo's $\Delta\rho$ reaching up to 0.48 and ΔE_{ab} exceeding 70, and Ferwerda's reaching $\Delta\rho$ of 0.49 and ΔE_{ab} of more than 50, when compared with spectrophotometer measurements. At a room-scale simulation level, both techniques result in overestimations in TAI, with errors ranging from 33% to 134%. According to

TABLE 5.9 TAI Percentage Errors for Different Methods

Method	TAI Error [%]
Cap	33%
Daylight	42%
Electric	48%
Mix	57%
Ferwerda	65%
IP	101%
Luo-cap	133%
Luo-no cap	134%

classification from Chapter 3, the spread in reflectance estimates aligns with MCoP0.2, indicating considerable uncertainty.

A lighting cap was primarily tested for Luo's technique, but also applied as a controlled lighting condition for Ferwerda's method. Interestingly, Ferwerda's results under the cap show a mismatch between sample-level and room-level performance: while the sample-level error is slightly higher (MRB = 16% versus 13%), the room-level TAI error is the lowest among all lighting conditions (33%). This discrepancy may be due to error cancellation in CBDM simulations, or because surfaces with larger errors occupy smaller areas in the room, thereby limiting their impact on the overall results. Based on these findings, using a cap is not essential for Ferwerda's method.

The choice of Luo's technique was motivated by its recent development and its suitability for planar surfaces, which are characteristic of building elements. It is also designed to perform under controlled flash lighting conditions. However, as reviewed by Kavoosighafi et al. (2024), alternative network architectures have been developed to operate under uncontrolled lighting and to estimate per-pixel material properties across entire scenes. Evaluating the applicability of these methods in daylight-related simulations remains a valuable direction for future research.

Illuminance-Proxy allows for the derivation of high-resolution reflectance maps from HDR images using sparse known reflectance points and surface interpolation. This enables reflectance estimation across large surfaces with minimal ground truth measurements, particularly beneficial in rooms with complex surfaces. Among the three, it is the only evaluated technique that attempts to reconstruct a full-field reflectance distribution using a physics-based approach. This method has three critical assumptions: planar surfaces, smoothly varying illuminance, and diffuse material behaviour. Deviations from these—such as the presence of specular surfaces (*e.g.*, metallic ducts, radiators) or sharp light gradients— will introduce unknown errors. The method is also device-dependent, requiring calibrated HDR cameras. Its performance on room-scale simulations yields a TAI error of

approximately 101%. Ground truth reflectance values are an essential input of the Illuminance-proxy method, making it dependent on specific devices compared to the other two. In this study, at the room level, the known input reflectance values were acquired using AHR due to the unavailability of a reflectance spectrophotometer during the measurement. Although relatively accurate, this technique is prone to errors (Bodart et al., 2008; Forouzandeh et al., 2024). This means that, given a more accurate input of known reflectance points, the results of the reflectance might be more accurate than the values reported in this work at the room level, as is shown in the 3-channel illuminance proxy test. This experiment showed a reflectance difference ($\Delta\rho$) of less than 0.08, significantly lower than the maximum error of 0.82 reported for the single channel.

Complex surfaces pose a challenge for on-site material characterisation. All three evaluated techniques—Ferwerda, Luo, and Illuminance-proxy—estimate pixel-wise reflectance. However, in this study, pixel-wise reflectance values are averaged, and comparisons are made against single-point ground truth measurements. For instance, brick surfaces in the studied scene exhibit high spatial complexity, yet the ground truth instrument, the Konica Minolta CM-26dG, samples an area of less than $2\,\mathrm{cm}^2$, which may not capture the full variation across mortar joints and brick colour gradients. This mismatch likely contributed to inaccuracies in the reported error values.

Spectral uplifting enables the reconstruction of a full spectral distribution from tristimulus reflectance, facilitating the simulation of non-visual lighting effects such as melanopic stimulus. Jakob and Hanika's method achieves smooth and energy-conserving spectral reconstructions, with errors generally within 20% for wavelengths above 400 nm. This results in relative errors of less than 6% in the estimation of m-EDI, with higher errors occurring under clear skies compared to overcast. This makes it suitable for applications that require spectral information, such as circadian lighting analysis and hyperspectral renderings. Even though the performance is promising, the choice of uplifting technique should be carefully considered in future implementations of spectral daylight simulations, as alternative methods also exist. For example, Van de Ruit proposes a fundamentally different approach by incorporating user interaction within a constrained spectral uplifting framework (Van De Ruit and Eisemann, 2023). This method acknowledges the fact that there is no one-to-one correspondence between tristimulus values and spectral distributions. Van de Ruit's work is the most recent at the time of writing, although other improvements in uplifting have been made since Jakob and Hanika's contribution (Peters et al., 2019; Tódová et al., 2021). As this project prioritizes automation, Jakob and Hanika's method—which does not rely on user interaction—was selected. However, the investigation of more recent uplifting techniques for spectral lighting evaluations is another promising research direction.

5.6 Conclusion

This chapter evaluated the accuracy and applicability of three image-based techniques— Illuminance-Proxy, Ferwerda, and Luo—for material reflectance chatacterisation in daylight simulations. In addition, Jakob and Hanika's spectral uplifting method was assessed for reconstructing spectral reflectance from tristimulus data, to enable simulation of circadian-driven non-visual impacts of light.

Ferwerda's technique emerged as the most balanced approach. It results in a relatively low mean bias error (MRB = 13%) and root mean squared error (RMSRE = 31%) in visible reflectance estimates. It also demonstrated stable performance under varying lighting conditions with minimal deviation in colour difference (ΔE_{ab}) and total annual illuminance (TAI) errors ranging from 33% to 65%, depending on the lighting under which the image samples were taken. This technique does not require a controlled lighting setup, making it practical for field use.

Luo's method, while fully automated and optimized for planar surfaces under flash, showed the highest error among the three approaches. Its $\Delta\rho$ reached up to 0.48, and ΔE_{ab} exceeded 70 in some cases. At the room level, this led to substantial overestimation in daylight availability, with TAI errors of 134%. These results suggest that its applicability for characterising daylight simulation remains limited.

The Illuminance-Proxy approach demonstrated moderate accuracy (MRB = 19%, RMSRE = 41%), with its key strength being the generation of pixel-wise reflectance values using only sparse ground truth data and HDR imagery. However, its accuracy and applicability depend on critical assumptions, including planar surfaces, diffuse reflection of materials, and smoothly varying illumination. Its performance decreases in the presence of specular or geometrically complex surfaces, as reflected in a 101% TAI overestimation. Moreover, it remains dependent on HDR-capable imaging and known reflectance values, which may limit scalability.

All three methods showed small errors in predicting glare probability, with errors below 0.02 in predicting DGP. Nonetheless, differences in daylight availability predictions are higher and up to 133% in the prediction of TAI.

Spectral uplifting using Jakob and Hanika's method reconstructed spectral reflectance with RMSRE below 20% across the visible spectrum (except at the edges below 400 nm). It resulted in an error of less than 6% in estimating m-EDI, which makes it suitable for circadian lighting and hyperspectral rendering applications.

In summary, image-based techniques offer accessible and scalable alternatives to traditional material measurement tools. Ferwerda's method provides the best overall

trade-off between accessibility and performance. Illuminance-Proxy is suitable for complex planar surfaces with diffuse materials. Spectral uplifting, when combined with these approaches, expands simulation capability into non-visual domains with negligible added error.

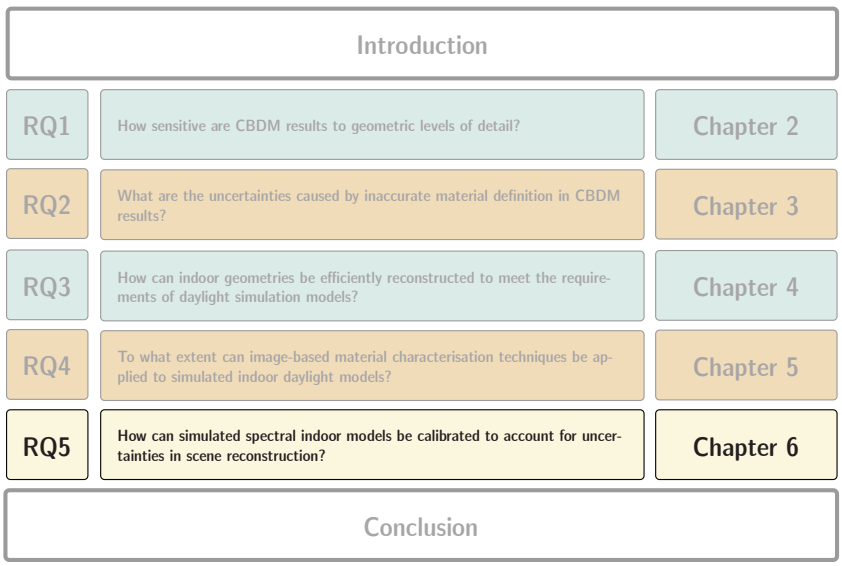
Introduction
RQ1
How sensitive are CBDM results to geometric levels of detail?
Chapter 2
RQ2
What are the uncertainties caused by inaccurate material definition in CBDM results?
Chapter 3
RQ3
How can indoor geometries be efficiently reconstructed to meet the requirements of daylight simulation models?
Chapter 4
RQ4
To what extent can image-based material characterisation techniques be applied to simulated indoor daylight models?
Chapter 5
RQ5
How can simulated spectral indoor models be calibrated to account for uncertainties in scene reconstruction?
Chapter 6
Conclusion

6 Calibration of a spectral daylight model

ABSTRACT

This chapter presents a calibration workflow for indoor spectral daylight simulation that focuses on external sources of uncertainty and restricts tuning to a single parameter: window spectral transmittance. The procedure generates transmittance options by scaling the measured spectrum up and down in fixed steps while preserving its spectral shape, and evaluates each option by comparing simulated and measured 18-channel irradiance values at a control sensor using a room-averaged mean absolute error metric. The best-performing option (*window_neg_3*) yields the lowest discrepancy ($\mathrm{MAE}_{\mathrm{room},w} = 0.0077\ \mathrm{W\,m^{-2}}$) with a spectral correlation of $r = 0.90$. Across all options, simulated–measured spectral shapes remain consistent (correlations 0.89–0.91). After calibration, the control sensor's systematic bias is substantially reduced for both photopic illuminance and m-EDI, with $\mathrm{MBE}_{\mathrm{rel}}$ improving from 290.42% to 1.36% for E_v and from 330.64% to 10.98% for m-EDI. Error magnitude and dispersion also decrease markedly ($\mathrm{RMSE}_{\mathrm{rel}} = 10.22\%$ for E_v, 14.33% for m-EDI; $\sigma_{\mathrm{rel}} \approx 10\%$). The melanopic/photopic ratio remains stable, showing only minor changes (errors $\sim 10\%$). Errors rise with increasing distance from the façade, indicating higher sensitivity to inter-reflections and local modelling as room depth increases. The analysis is limited to a single room and to measurements collected under overcast conditions. Overall, scaling window transmittance while preserving spectral shape provides an effective means to reduce simulation bias for E_v and m-EDI and to maintain consistent spectral behaviour.

This chapter is based on a manuscript currently under peer review: Forouzandeh, N., Jakubiec, A., Nan, L., Stoter, J., & Brembilla, E. *Calibration of simulated spectral daylight for existing indoor spaces*.

6.1 Introduction

After the discovery of intrinsically photosensitive retinal ganglion cells (ipRGCs) in the human eye in the early 2000s, several scientific fields became aware of the impact that lighting has on entrainment of the circadian system and therefore sleeping patterns and well-being (Brainard et al., 2001; Thapan et al., 2001). The responses of our bodies' ipRGC-influenced light (IIL) seem to be affected through a non-immediate indirect pathway that influences our internal clock, and an immediate direct pathway that impacts alertness and melatonin levels (Ámundadóttir, 2016; Soto Magán, 2021). This is influenced by light-related stimuli such as retinal irradiance, timing, duration, prior light history, and spectrum (Pierson et al., 2023).

The responses of our bodies' IIL seem to be affected through a non-immediate indirect pathway that influences our internal clock, and an immediate direct pathway that impacts alertness and melatonin levels (Ámundadóttir, 2016; Soto Magán, 2021). This is influenced by light-related stimuli such as retinal irradiance, timing, duration, prior light history, and spectrum (Pierson et al., 2023).

Building occupants spend around 90% of their time indoors (Klepeis et al., 2001). This marks a significant shift from our ancestors, who lived primarily outdoors and were exposed exclusively to natural light, making building design a critical determinant of key light-exposure factors. The widespread use of poorly designed electric lighting negatively affects our IIL and is potentially a source of well-being and health problems. To address these problems, recommendations on target illuminance levels are available in previous works, as summarized in Table 6.1 (Brown et al., 2022).

To implement those recommendations and make informed decisions as building designers and engineers, either for newly designed or existing buildings, an accurate model of the room is essential. This is why several software packages have been developed to simulate non-visual effects of light in buildings (Gkaintatzi-Masouti et al., 2021). These tools assist designers to optimally configure the room and its components with the IIL-related health issues of occupants in mind.

When validating those software tools, researchers account for all the factors that influence circadian responses. Therefore, controlled empirical experiments are set up to minimize the unknown parameters or the influence of uncertain environmental factors. Such experiments are typically performed in a room with small dimensions and controlled lighting, providing researchers with flexibility across different aspects of the experiment (Pierson et al., 2023; Mardaljevic, 1995).

A validated simulation tool, which remains valid irrespective of the use-case building, does not result in a valid digital model of the building per se. When analysing existing, often complex buildings, the sources of discrepancy between measurements and

TABLE 6.1 Lighting recommendations for different indoor environments (Brown et al., 2022).

Environment	Lighting Recommendation
Daytime light, indoor environments	Minimum m-EDI should be 250 lux at the eye level for at least four hours starting before noon. Daylight is preferred, if additional electric lighting is required, the polychromatic white light should ideally have a spectrum that is similar to natural daylight.
Evening light, residential and other indoor environments	During the evening, starting at least 3 hours before bedtime, maximum m-EDI should be 10 lux measured at the eye level. The white light should have a spectrum depleted in short wavelengths close to the peak of the melanopic action spectrum.
Nighttime light, sleep environment	The sleep environment should be as dark as possible. Maximum ambient m-EDI is 1 lux measured at the eye level. In case certain activities during the nighttime require vision, the maximum m-EDI is 10 lux measured at the eye level.

simulations are usually higher and sometimes beyond control. As listed in Fig. 6.1, there are four sources that explain this discrepancy: (1) Sun and sky, (2) building context, (3) indoor, and (4) Measurement and modelling factors.

Calibration workflows for visual daylight simulations have already been explored in the literature, including methods that tune model inputs against measured luminance and illuminance (Quek and Jakubiec, 2021). However, no equivalent workflow exists for indoor spectral or non-visual outcomes, despite the higher uncertainty and sensitivity of these simulations. This motivates the development of the present method.

The aim of this chapter is to develop and test a calibration workflow for indoor spectral daylight simulation that explicitly targets key, poorly controlled sources of simulation–measurement mismatch: (1) sun–sky conditions, (2) exterior/context obstructions, and (3) window spectral transmittance. The first two are typically beyond the practitioner's control during short on-site surveys, and the third is highly uncertain in real contexts (due to *e.g.*, dust, ageing, maintenance) yet has a substantial impact on indoor irradiance (Forouzandeh et al., 2024). The workflow tunes only the window transmittance—while preserving its spectral shape—using short in situ measurements, and evaluates performance with relative bias, error magnitude, and dispersion metrics for photopic illuminance (E_v) and Melanopic equivalent daylight illuminance (m-EDI).

To address the current lack of a standard calibration workflow for indoor IIL simulation, the chapter (Section 6.2) reviews related validation studies for spectral irradiance models and software, then (Section 6.3) introduces the study room, measurement setup, simulation model, and the proposed calibration procedure, and

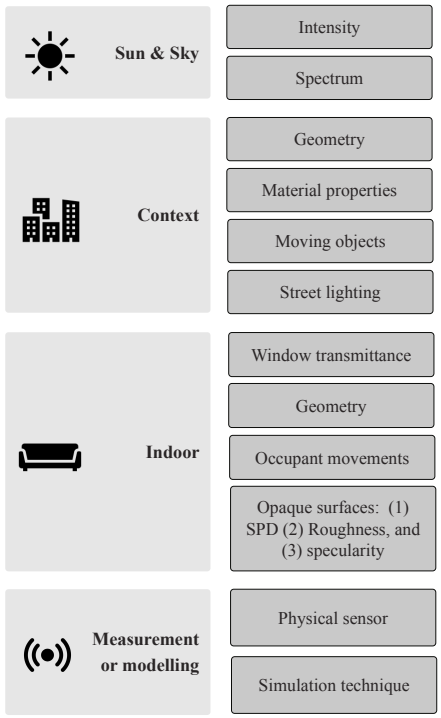

FIG. 6.1 Influencing inputs in indoor spectral irradiance simulation.

finally (Sections 6.4–6.6) reports errors, discusses findings, and concludes.

6.2 Literature Review

Compared to daylight simulation, the field of building energy modelling has developed more established practices for calibration. Coakley et al. (Coakley et al., 2014) provide a comprehensive overview of how energy models are commonly aligned with real-world measurements to improve accuracy. In their review, they describe both manual and automated calibration methods, ranging from hands-on adjustments and site audits to more advanced statistical techniques, such as sensitivity analysis, Monte Carlo simulations, and Bayesian approaches. Unlike daylight simulation, energy simulation has well-defined validation indicators, such as Mean bias error (MBE) and Coefficient of Variation of the Root Mean Square Error (CVRMSE), and

widely recognized guidelines, including American Society of Heating, Refrigerating and Air-Conditioning Engineers (ASHRAE) Guideline 14 (Guideline et al., 2014).

The discrepancy between the simulated and measured daylight values can be attributed to various sources (see Fig. 6.1). One likely source is the simulation engine itself. Mardaljevic conducted a validation of *Radiance* illuminance results against measurements taken in full-scale experimental rooms under real sky conditions for both overcast and clear skies. Relative errors for illuminance measurements were within 15% in illuminance predictions in all 4 case study rooms (Mardaljevic, 1995). To study the validity of spectral simulation tools, Pierson et al. compared the performance of *LARK* and *ALFA* with real measurements under different sky models in laboratory settings (Pierson et al., 2023). They reported a potential mean error of $\pm$20% for point-in-time indicators (m-EDI, MP ratio)for *LARK* model outputs when compared to laboratory measurements. For *ALFA*, the authors observed wider variability across the visible spectrum, with relative spectral irradiance differences ranging from 10% to over 30%, depending on the wavelength and sky conditions.

Tools, however, are not the only source of error when modelling full-scale rooms. Uncertainties and errors can also arise from an inaccurate characterisation of other inputs of the model (see Fig. 6.1). It is therefore necessary for a simulated model, before making any intervention, to ensure its validity and to understand the degree to which it accurately represents the real world. This alignment can be improved through calibration processes, which are defined as the adjustment of numerical or physical model parameters.

TABLE 6.2 Summary of validation and calibration studies for indoor daylight simulation.

Ref.	Aim	Daylight /Electric	Engine	Context	Building info	Compared data	Accuracy after calibration
Jones and Reinhart (2015, 2017)	Validate image-based glare prediction using ray-tracing renderings vs. HDR photographs	Daylight	Radiance, Accelerad	Cambridge, Massachusetts, USA	Full-scale conference room	HDR images; DGP; luminance distributions	$\leq$20% photometric error; DGP accuracy 93–99%; discomfort glare 71–99%; Accelerad 16–44$\times$ faster than Radiance
Lim et al. (2010)	Validate simulated results against physical model measurements	Daylight	Radiance (Desktop Radiance 2.0)	Malaysia	Scaled physical model under real sky	Workplane E_v, surface luminance, Daylight Factor (DF), luminance ratio	Absolute mean differences: 81.63%, 71.06%, 49.71%; relative ratios: DF 26.06%, luminance ratio 29.75%
Quek and Jakubiec (2021)	Calibration (lamp as tunable parameter)	Both	Radiance	Singapore	Open-plan offices	Horizontal and vertical E_v	Relative RMSE 25.8–45.5%

Ref.	Aim	Daylight /Electric	Engine	Context	Building info	Compared data	Accuracy after calibration
Sunger and Vaidya (2019)	Calibrate VT for dust factor to evaluate daylight performance	Daylight	Lightstanza	Ahmedabad, India	Workshop building	E_v	RMSE and Normalized Mean bias error (NMBE) $< 4\%$
Kim et al. (2022)	Integrated MPC	Both	DIVA	Incheon, South Korea	Open-spaced factory building	E_v	Daylighting: MBE $= 4.9\%$, CVRMSE $= 24\%$; Electric: MBE $= 3.7\%$, CVRMSE $= 7.7\%$
He et al. (2022)	Calibration of simulated circadian lighting model	Both	ALFA	Lawrence, Kansas, USA	Single room	E_v, m-EDI, Circadian Stimulus (CS), M/P, Spectral Power Distribution (SPD)	$r_{\mathrm{SPD}} \geq 0.9$; M/P $\lvert \mathrm{MBE}_{\mathrm{rel}} \rvert < 4\%$, $\mathrm{RMSE}_{\mathrm{rel}} \leq 7\%$; E_v, m-EDI, CS: $\lvert \mathrm{MBE}_{\mathrm{rel}} \rvert \leq 10\%$, $\mathrm{RMSE}_{\mathrm{rel}} \leq 20\%$; $\geq$75% within $\pm 20\%$

Table 6.2 summarises key validation and calibration studies which cover engines, contexts, compared data, and reported accuracies for indoor daylight and spectral simulation.

Jones et al. conducted an HDR-based comparison between real camera captures and those from *Radiance* and *Accelerad* renderings, resulting in magnitudes of error within the accepted bounds of 20%. In another study, they compare glare measurements from HDR photographs and computer renderings of the same day-lit room under 240 clear and 38 cloudy sky conditions in order to assess how accurately architects can predict glare through simulation. Depending on the scene, these methods predicted DGP levels due to bright sources with between 93% and 99% accuracy and discomfort glare due to contrast with between 71% and 99% accuracy (Jones and Reinhart, 2015, 2017).

Lim et al. conducted a validation study of the *Radiance* simulated results against a scaled model under the tropical sky of Malaysia. In their study, the absolute external illuminance, work plane illuminance, and surface luminance recorded high mean differences from the measured results, with 81.63%, 71.06%, and 49.71%, respectively. Relative ratios such as the DF yielded a mean difference of 26.06%, and the luminance ratio was 29.75% only, indicating that while absolute values showed large deviations under tropical sky conditions, relative metrics such as DF and luminance ratios provided more consistent agreement between simulation and measurement (Lim et al., 2010).

Another example is the work of Quek and Jakubiec on CBDMs for open office rooms. In their study, the properties of an electric lamp were used as a tunable parameter for calibration. The results showed a relative RMSE between 25.8% and 45.5% for horizontal and vertical photopic measurements (Quek and Jakubiec, 2021).

Sunger and Vaidya proposed a calibration process by adjusting the visible transmittance of the north-facing glazing to account for the dust factor. The errors in their final model were in the range of 4% in illuminance prediction after calibration (Sunger and Vaidya, 2019).

Kim et al. developed an integrated model predictive system for lighting control using *DIVA* programme, calibrated with measured illuminance using a deep deterministic policy gradient Kim et al. (2022).

He et al. proposed a two-stage calibration–validation workflow for circadian lighting simulation, which first calibrates a spectral model at night under electric lighting and then validates it in daytime with integrated daylight and electric lighting, implemented in ALFA's 81-channel spectral ray tracing. By iteratively tuning luminaire intensity distribution and lumen output, light-source Spectral Power Distribution (SPD), and surface SRD/STD, the fully calibrated model achieved high agreement between simulated and field-measured SPDs ($r_{\mathrm{SPD}} \geq 0.9$) and low relative errors: for the M/P ratio, $|\mathrm{MBE}_{\mathrm{rel}}| < 4\%$ and $\mathrm{RMSE}_{\mathrm{rel}} \leq 7\%$; for corneal illuminance (EV), m-EDI, and Circadian Stimulus (CS), $|\mathrm{MBE}_{\mathrm{rel}}| \leq 10\%$ and $\mathrm{RMSE}_{\mathrm{rel}} \leq 20\%$, with

at least 75% of data points within $\pm 20\%$ residuals during both calibration and validation. Sensitivity analyses further showed that mis-specifying the light-source SPD or luminaire distribution quickly degrades accuracy—even when photopic targets are met—highlighting the importance of field SPD measurement and material spectral characterisation when targeting non-visual metrics (He et al., 2022).

Existing spectral engines such as Lark and ALFA have been validated against field measurements (Pierson et al., 2023) and implemented in geometrically complex environments (Orman et al., 2025), but both rely on Graphical User Interface (GUI)-based workflows. This limits their efficient applicability for large-scale parametric studies, deployment on high-performance and embedded computing systems, and integration into automated calibration pipelines. In contrast, *Radiance v6.0* (released in 2024) introduced native hyperspectral rendering that partitions the spectrum into user-specified bands traced through a single ray tree, thereby avoiding per-band re-renders and reducing chromatic noise (Ward and Wang, 2024). This pipeline includes new spectral primitives (`spectrum`, `specfile`, `specfunc`, `specdata`, `specpict`) for single-pass spectral propagation. While this hyperspectral feature is not yet validated against field measurements, Radiance itself has long been validated for illuminance predictions across diverse building types, orientations, and sky conditions (Geisler-Moroder et al., 2016; Kharvari, 2020; Lee et al., 2018; Mardaljevic, 1995; McNeil et al., 2013; Mangkuto et al., 2014).

The objective of this study is to address the absence of standardised calibration workflows for spectral daylight simulation by introducing a method that relies on short-term *in situ* measurements and systematic adjustment of window transmittance as the primary tunable parameter.

6.3 Methods

The proposed calibration workflow was tested on a use case classroom (described in Section 6.3.1) in which spectral measurements were collected during a single visit (Section 6.3.2). The same classroom was then evaluated using spectral simulation tools (Section 6.3.3) and the resulting metrics were used to demonstrate a calibration workflow based on adjustments to window transmittance (Section 6.3.4).

6.3.1 Use case room

One university classroom at the University of Toronto was chosen as the case study. The room has dimensions of 16.6 m $\times$ 10.6 m $\times$ 3.5–6.7 m and a Window-to-Floor Ratio (WFR) of 9.1%. Toronto's climate is classified as a warm-summer humid continental (Dfb) under the Köppen–Geiger system, featuring large seasonal temperature differences, with warm, humid summers and cold winters, and precipitation distributed evenly throughout the year.

Geometrical configurations of the case study room was captured as a dense and accurate point cloud using a Light Detection and Ranging (LiDAR) scanner. The final point cloud was generated after automatic registration of multiple scans using checkerboard targets in the scene, followed by subsampling and removal of outliers. The surface polygonal 3D model was then constructed manually on top of the point clouds. This surface model along with the location of the sensors is shown in Fig.6.2. The spectral material properties of all opaque surfaces were measured using a Konica Minolta CM-2600d reflectance spectrophotometer. The overall appearance of these materials is shown in Fig. 6.2. Spectral transmittance of the glazing was determined by dividing the internal and external spectral irradiance measured with a Konica Minolta CL-500A spectrophotometer as shown in Fig. 6.3.

A 5-minute Tropical Atmosphere Ocean (TAO) weather dataset for the study location was acquired from the measurement station at the University of Toronto campus. Direct Normal Irradiance (DNI) and Diffuse Horizontal Irradiance (DHI) values for each time step were derived from the Global Horizontal Irradiance (GHI) using the Skartveit and Olseth split model (Skartveit and Olseth, 1987).

6.3.2 Spectral light measurements

Spectral irradiance within the spectral range of 380-780 nm was measured for 75 minutes, with a 1-minute time step at the occupants' eye level at 4 spots with a nanoLambda sensor. The measurements were done during daytime in the morning on the 13th of November 2022, under an overcast sky. One sensor was placed on the interior side of the window, approximately 200 centimetres from the floor, and served as a calibration sensor. This was done to separate the effects of inter-reflections of irradiance within the indoor room on the measurements. The measured m-EDI values are shown in Fig. 6.4 over the monitoring period.

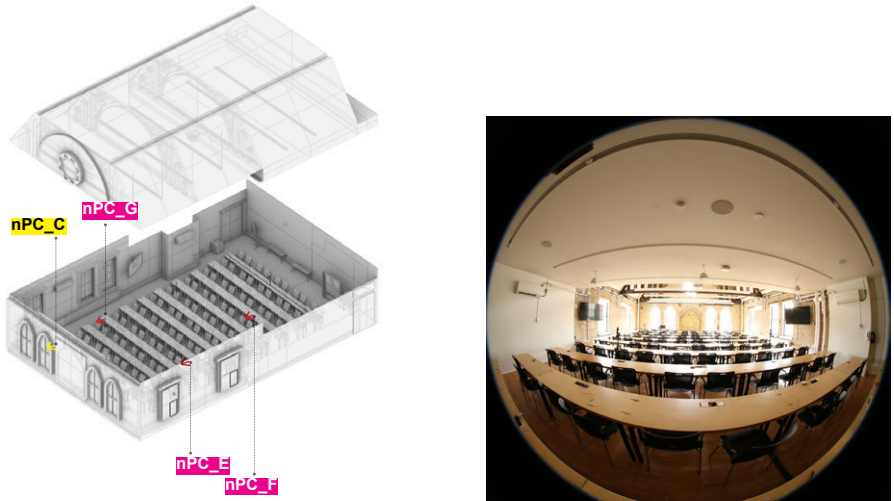

FIG. 6.2 3D model and real fisheye view of the studied room.

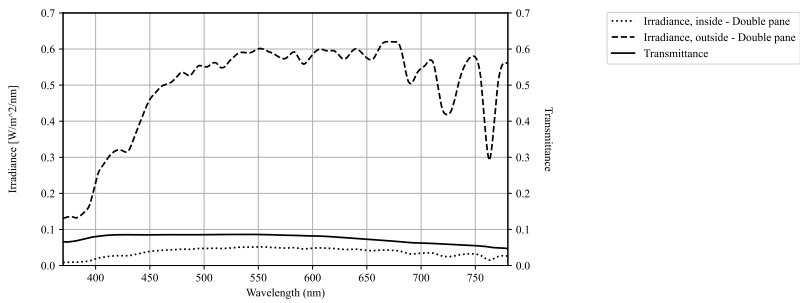

FIG. 6.3 Irradiance inside and outside of the window for transmittance calculation. This is measured by Konica Minolta CL-500A.

6.3.3 Simulated model

Radiance v6.0 offers a hyperspectral rendering feature and is a faster computational software compared to Lark or ALFA. Therefore, it was used for this study (Ward and Wang, 2024). Five ambient parameters, *i.e.*, *ad*, *as*, *ar*, *aa*, *ab*, were determined by a convergence test on a virtual sensor on the farthest wall from the facade at DA_200. The convergence range (and the final value) for each of the parameters is 32-8192 (1024), *ad*/2 (512), 8-32768 (512), 0.4-0.05 (0.2), and 1-8 (5), respectively. The simulations were performed in 18 channels, although the preliminary test showed that increasing the band count beyond 9 channels produced negligible changes in m-EDI. Geometry, surface spectral reflectance, sky/solar model selection, sensor

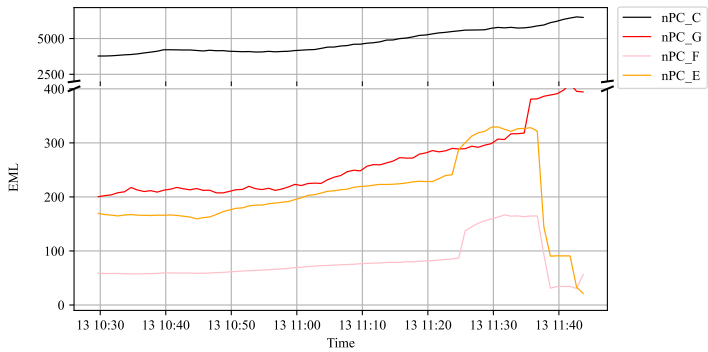

FIG. 6.4 m-EDI values from measurement.

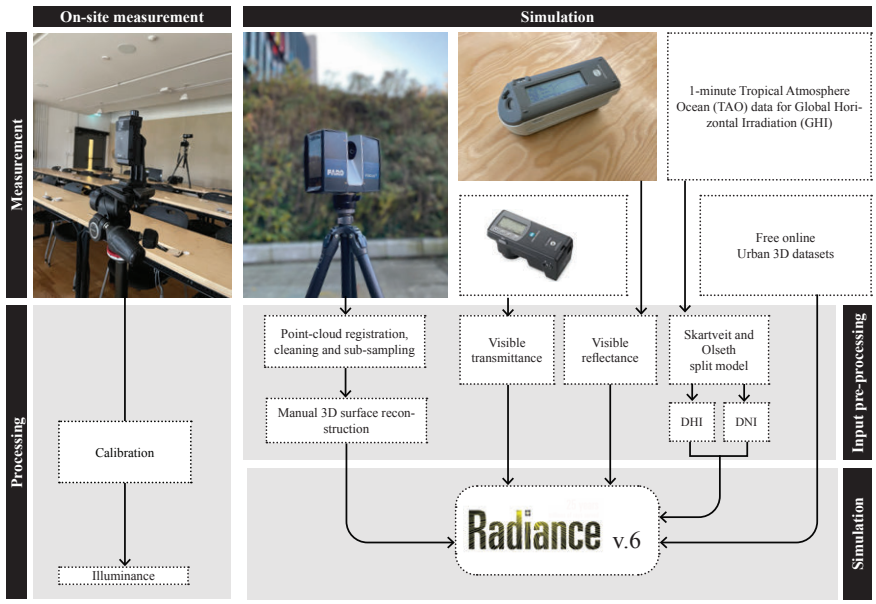

FIG. 6.5 Preparation of measured and simulated data

poses, and the simulation settings are held constant. Only the glazing spectral transmittance magnitude is varied with preserved spectral shape.

6.3.4 Calibration workflow

Simulation inputs can be assessed along two independent attributes: (i) their *characterisation uncertainty*, and (ii) their *output sensitivity*. The calibration decision (*i.e.*, which parameter to tune and within which range) follows this prioritisation (Fig. 6.6). Among the various inputs, window spectral transmittance shows both high uncertainty in practice—due to ageing, dirt, coatings, and limited on-site characterisation—and a strong influence on indoor illuminance (see Chapter 3). For this reason, it is selected as the sole calibrated input in this workflow, while other parameters with lower combined uncertainty and impact are kept fixed.

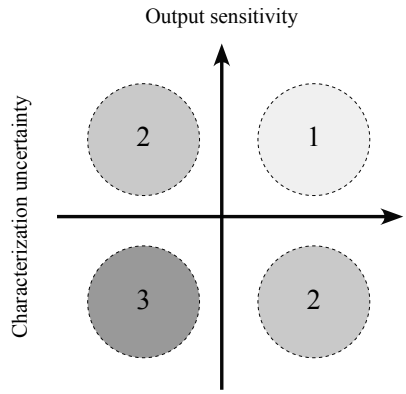

FIG. 6.6 Schematic prioritisation matrix for designing a calibration workflow for each influencing parameters listed in Fig.6.1.

The proposed calibration procedure, as shown in Fig. 6.7, is based on iterative adjustment of window transmittance to reduce the simulation error. This process began with the generation of window transmittance options, where the base transmittance values are measured on site (see Fig. 6.3). Each option is obtained by scaling the base spectrum up or down with successive factors, *i.e.*, multiplying or dividing the transmittance values by $1 + step \times 0.125$, while ensuring values remain between 0 and 1. Seven options are generated above the base and seven below, with a 0.1 step, while preserving the overall spectral distribution (Fig. 6.8). Next, the 18-channel irradiance values corresponding to each of these options are simulated for the control sensor across 16 time steps.

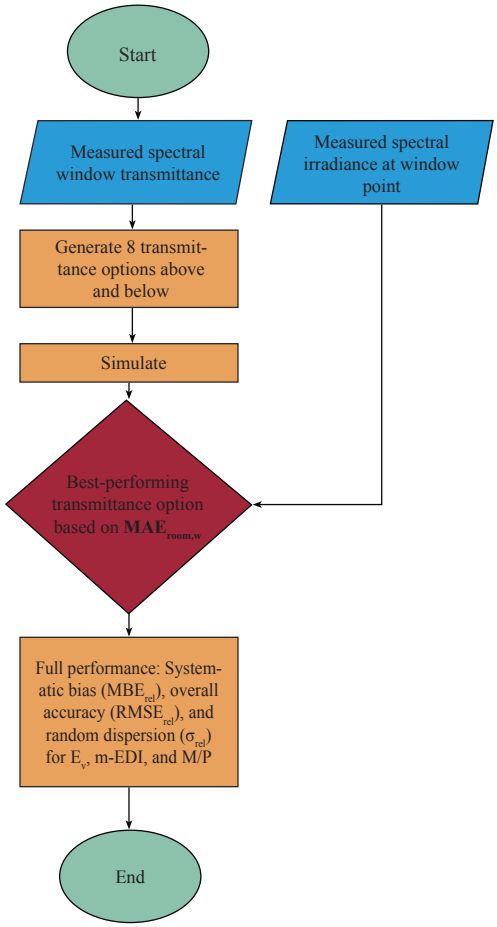

FIG. 6.7 Calibration pipeline

6.3.4.1 Finding the best-performing window

The best performing window is selected by comparing the 18-channel simulated and measured irradiance values for each window option. For this, a Mean Absolute Error (MAE) was calculated as the error metric as described in Eq. 6.1.

$$\text{MAE}_{\text{room},w} = \frac{1}{T}\sum_{ts=1}^{T}\frac{1}{cs}\sum_{i=1}^{cs}|y_{i,ts}^{\text{measured}} - y_{i,ts}^{\text{simulated}}| \tag{6.1}$$

Where:

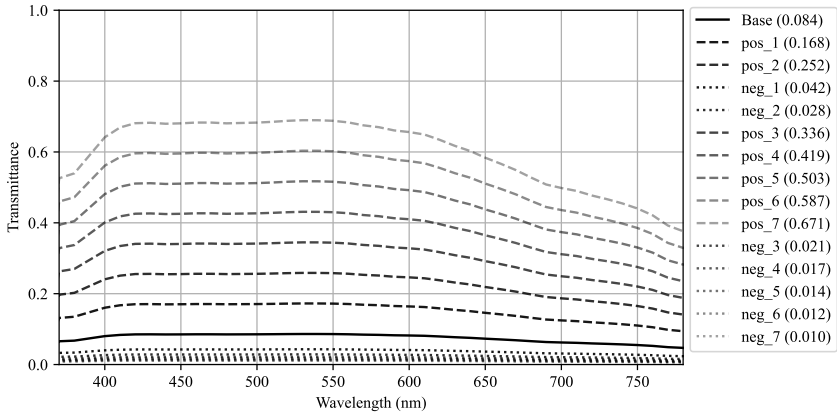

FIG. 6.8 Spectral properties of the window materials for each iteration of the calibration process. The dashed lines represent the positive adjustments, the dotted lines represent the negative adjustments, and the solid black line represents the measured data. The Visible Light Transmission (VLT) of each option is in the parenthesis.

- $y_{i,ts}^{\text{measured}}$ is the measured irradiance value for channel i at time ts.
- $y_{i,ts}^{\text{simulated}}$ is the simulated irradiance value for channel i at time ts.
- cs is the number of spectral channels.
- w is the window option.
- T is the total number of time steps.

6.3.4.2 Evaluation of the calibrated models

Following the identification of the best-performing transmittance option and linear transformation, the calibrated model is evaluated by comparing the measured and simulated data using the MBE_{rel}, the RMSE_{rel}, and the σ_{rel} for E_v, m-EDI, and M/P ratio. The MBE_{rel} quantifies the bias between simulated and measured values and indicates over- and under-estimations. The RMSE_{rel} combines both systematic and random errors to provide the overall magnitude of the deviations. Finally, σ_{rel} represents the spread of the errors around the mean bias and isolates the random component after removing the systematic bias.

$$\text{MBE}_{\text{rel}}(\%) \;=\; 100 \times \frac{1}{n} \sum_{i=1}^{n} \frac{y_i - \hat{y}_i}{\hat{y}_i} \tag{6.2}$$

$$\mathrm{RMSE}_{\mathrm{rel}}(\%) \;=\; 100 \times \sqrt{\frac{1}{n}\sum_{i=1}^{n}\left(\frac{y_i - \hat{y}_i}{\hat{y}_i}\right)^2} \tag{6.3}$$

$$\sigma_{\mathrm{rel}}(\%) \;=\; 100 \times \sqrt{\frac{1}{n}\sum_{i=1}^{n}\left(\frac{y_i - \hat{y}_i}{\hat{y}_i} - \overline{\left(\frac{y - \hat{y}}{\hat{y}}\right)}\right)^2} \tag{6.4}$$

Where n is the number of observations (time steps), y_i is the simulated value (E_v or m-EDI) for observation i $[lx]$, $\hat{y}_i$ is the measured value (E_v or m-EDI) for observation i $[lx]$.

6.4 Results

6.4.1 Best-performing window

Errors and correlation corresponding to each window option are presented in Table 6.3. The $\mathrm{MAE}_{\mathrm{room},w}$ values range between 0.0077 and 1.60 W/m^2. The spectral shape is consistently reproduced in all window options, with Pearson correlation coefficients between 0.89 and 0.91, which is visible in a single time step spectral comparison in Fig. 6.9. The best-performing window is *Window_neg_3* with a transmittance shown in Fig. 6.10. This window option corresponds to VLT of 0.021 which is one-fourth of the measured window. This is due to ageing and accumulated dust in on the windows. The corresponding spectral bias for all time steps in the control sensor is illustrated in Fig. 6.11 before and after calibration.

6.4.2 Errors in the calibrated models

A post-calibration comparison of measured and simulated E_v and m-EDI is shown in Fig. 6.12. The corresponding aggregate errors—reported both before and after the window-selection step—are summarized in Table 6.4 using RMSE_{rel}, MBE_{rel}, and σ (standard deviation of residuals). Together, these metrics indicate the systematic bias (MBE_{rel}), overall accuracy (RMSE_{rel}), and random dispersion after bias removal (σ_{rel}).

TABLE 6.3 $\mathrm{MAE}_{\mathrm{room},w}$ and correlation for different windows

Window ID	$\mathrm{MAE}_{\mathrm{room},w}$	Correlation
window_neg_7	0.0210	0.91
window_neg_6	0.0172	0.91
window_neg_5	0.0128	0.91
window_neg_4	0.0088	0.91
window_neg_3	**0.0077**	**0.90**
window_neg_2	0.0211	0.90
window_neg_1	0.0549	0.90
window_000_0	0.1555	0.89
window_pos_1	0.3672	0.89
window_pos_2	0.5857	0.89
window_pos_3	0.7888	0.89
window_pos_4	0.9947	0.89
window_pos_5	1.1965	0.89
window_pos_6	1.4064	0.89
window_pos_7	1.6044	0.89

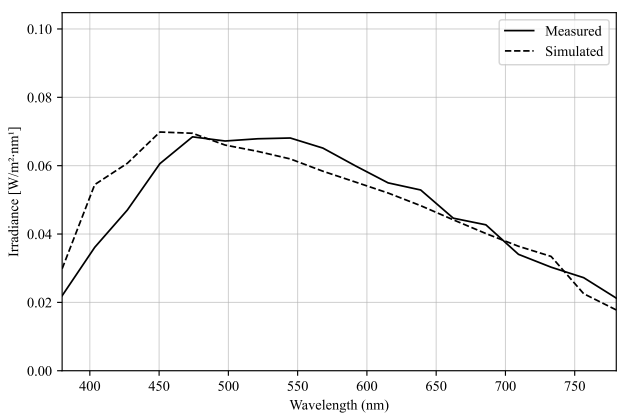

FIG. 6.9 Spectral comparison for a single example time step at the control nanoLambda sensor after calibration.

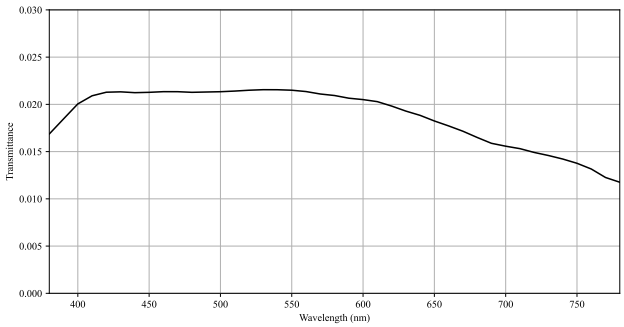

FIG. 6.10 Spectral transmittance of *Window_neg_3* window.

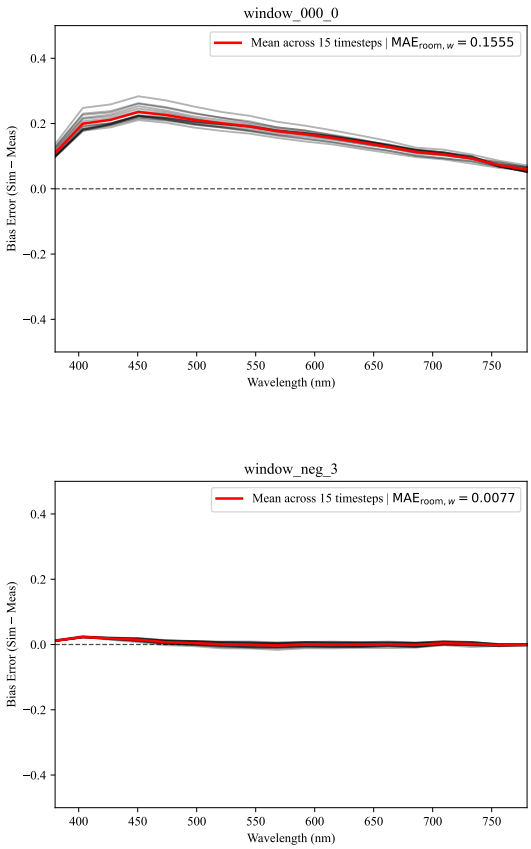

FIG. 6.11 Spectral simulation errors on the control sensor before (top) and after calibration (bottom).

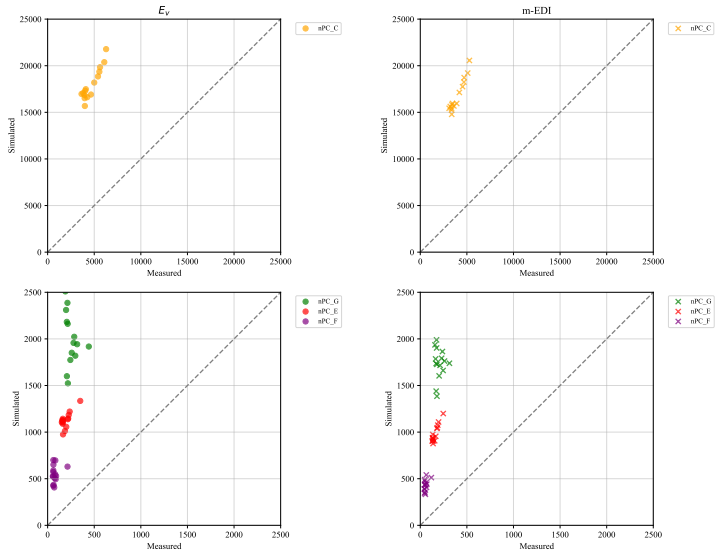

Before calibration

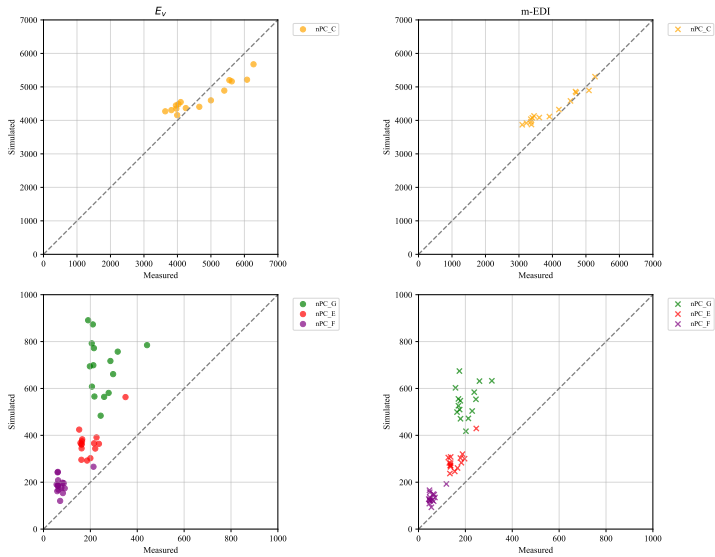

After calibration

FIG. 6.12 Comparison of measured and simulated E_v and m-EDI, before and after calibration for the control sensor and the other sensors; sensor locations as shown in Fig. 6.2.

Before calibration, the control sensor exhibited extremely high relative errors, with both MBE_{rel} and $RMSE_{rel}$ exceeding several hundred percent (*e.g.*, $MBE_{rel,Ev}$ =

290.42%, $\text{MBE}_{rel,m-EDI}$ = 330.64%). After calibration, MBE_{rel} values were reduced to within 11% (E_v = 1.36%, m-EDI = 10.98%). Similarly, RMSE_{rel} and σ_{rel} decreased substantially (photopic RMSE_{rel} from 293.28% to 10.22%, σ_{rel} from 40.81% to 10.13%). The M/P ratio remained stable across all sensors, with relatively low errors even before calibration (MBE_{rel} = 10.49%) and only a minor change after (9.68%), suggesting that the relative spectral balance between melanopic and photopic components was preserved.

After calibration, the accuracy for the control sensor was found to be within 11% for E_v and m-EDI, with σ around 10%. However, all other sensors resulted in higher errors than the control one; as it is shown in Fig. 6.12 and Fig. 6.13, accuracy and precision are highly location dependent: the greater the distance from the windows, the larger the imprecision and inaccuracy. There is consistent over-prediction both before and after calibration.

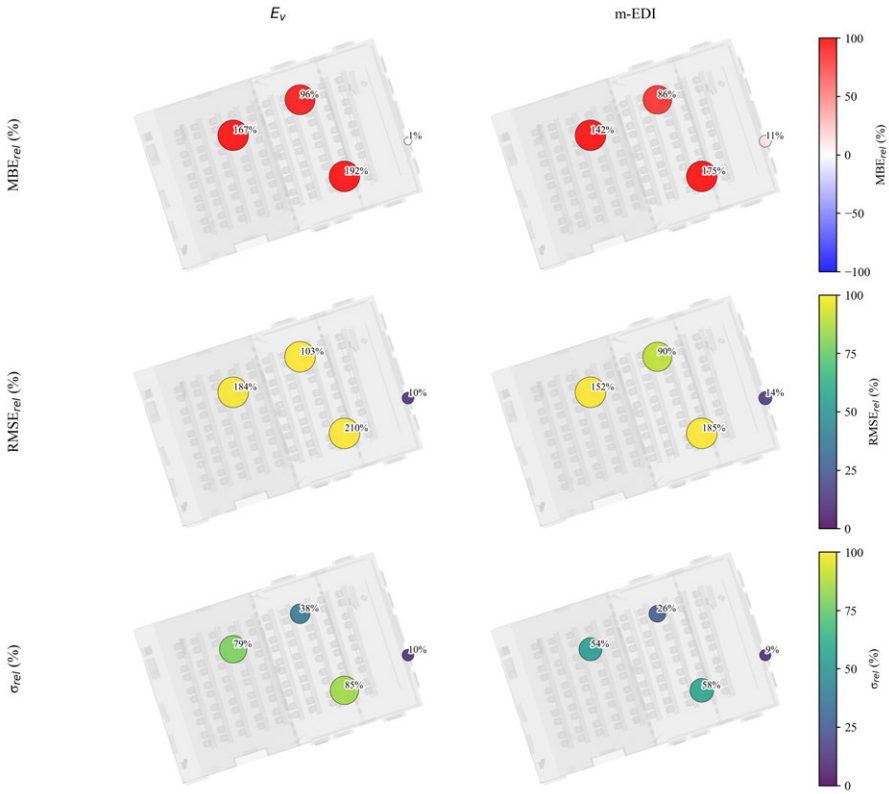

FIG. 6.13 Spatial pattern of accuracy (MBE_{rel}) and precision (σ_{rel}) after calibration. Point size indicates the magnitude of the metric.

TABLE 6.4 Relative error metrics before and after calibration for each sensor, the sensors are sorted based on their distance from the front facade.

Sensor	Metric	Step	E_v (%)	m-EDI (%)	M/P (%)
nPC_C (control)	MBE_{rel}	Before calibration	290.42	330.64	10.49
		After calibration	1.36	10.98	9.68
	RMSE_{rel}	Before calibration	293.28	332.77	10.68
		After calibration	10.22	14.33	9.87
	σ_{rel}	Before calibration	40.81	37.51	1.98
		After calibration	10.13	9.20	1.94
nPC_G	MBE_{rel}	Before calibration	758.79	781.33	5.38
		After calibration	191.81	175.49	-3.23
	RMSE_{rel}	Before calibration	800.80	803.64	11.11
		After calibration	209.82	184.73	9.72
	σ_{rel}	Before calibration	255.99	188.01	9.71
		After calibration	85.04	57.71	9.17
nPC_E	MBE_{rel}	Before calibration	500.45	528.94	5.92
		After calibration	95.59	86.21	-3.78
	RMSE_{rel}	Before calibration	510.23	533.41	9.76
		After calibration	102.91	90.17	7.02
	σ_{rel}	Before calibration	99.39	68.94	7.76
		After calibration	38.12	26.41	5.91
nPC_F	MBE_{rel}	Before calibration	668.03	672.67	3.81
		After calibration	166.65	142.00	-6.48
	RMSE_{rel}	Before calibration	702.20	690.64	13.45
		After calibration	184.45	151.88	13.24
	σ_{rel}	Before calibration	216.39	156.50	12.89
		After calibration	79.06	53.88	11.54

6.5 Discussion

The calibration strategy was constrained to a single, physically interpretable degree of freedom: window spectral transmittance. The procedure scaled the measured transmittance spectrum up or down in fixed steps while preserving its spectral shape to the measured value on-site, thereby addressing key uncertainties associated with external boundary conditions without conflating them with interior reflectance or geometric parameters. Within this framework, the best-performing option (*window_neg_3*) minimized the 18-channel irradiance discrepancy on the control sensor, with $\mathrm{MAE}_{\mathrm{room},w} = 0.0077\ \mathrm{W\,m^{-2}}$ and correlation $r = 0.90$.

This study shows that the simulated spectral shapes agree well with field measurements, even though the intensity shows a very high improvement after calibration. Pearson correlation coefficients between simulated and measured spectra remain in the range 0.89–0.91 across window options, indicating a consistent match in spectral form that underpins the stable behaviour of the melanopic/photopic (M/P) ratio. Consistent with this, the M/P errors were already low before calibration ($\mathrm{MBE_{rel}} = 10.49\%$, $\mathrm{RMSE_{rel}} = 10.68\%$) and improved slightly after calibration ($\mathrm{MBE_{rel}} = 9.68\%$, $\mathrm{RMSE_{rel}} = 9.87\%$).

After calibration, the systematic bias on the control sensor was effectively removed for both photopic and melanopic illuminance near the facade. For E_v, $\mathrm{MBE_{rel}}$ shifted from 290.42% to 1.36%, and for m-EDI from 330.64% to 10.98%. Overall accuracy and precision improved significantly: $\mathrm{RMSE_{rel}}$ declined to 10.22% (E_v) and 14.33% (m-EDI), while σ_{rel} was 10.13% and 9.20%, respectively. In practical terms, accuracy for the control sensor is within 11% for E_v and m-EDI, with a residual dispersion of about 10%. It is notable that both before and after calibration, the direction of the bias was consistently an overprediction.

Errors exhibit clear spatial dependence. Sensors located deeper in the room show larger biases and dispersion than the control sensor, consistent with increased sensitivity to inter-reflections and local modelling as distance from the façade increases. Part of this spread can be attributed to the limits of sensor calibration and to necessary simplifications in surface descriptions (*e.g.*, texture homogenization). These effects are visible in the spectral comparisons across sensors after calibration and in the spatial pattern of $\mathrm{MBE_{rel}}$ and σ_{rel}.

The calibrated transmittance that yielded the best agreement is substantially lower than the measured base spectrum. This outcome is consistent with the chosen workflow—*i.e.*, preserving spectral shape while scaling magnitude—and with the observation that external boundary conditions and glazing transmission exert first-order influence on the indoor spectral irradiance reaching the eye. Within the present pipeline, this parameterisation provided a direct and practical approach for aligning measured and simulated irradiance without adjusting interior inputs.

Finally, *Radiance v6.0* was adopted for its efficient, scriptable hyperspectral rendering, which enables tractable calibration runs and integration into automated workflows. While *Radiance* has a long record of validation for illuminance predictions under diverse conditions, its hyperspectral pipeline has not yet been systematically validated against field measurements.

The present results—strong spectral-shape agreement, and near-zero post-calibration bias on the control sensor—establish a practical calibration pathway based on short-term measurements and transmittance adjustment, and delineate where residual discrepancies persist (notably at locations farther from the façade).

6.6 Conclusion

This chapter introduces and tests a calibration workflow for indoor spectral daylight simulation that prioritises inputs by characterisation uncertainty and output sensitivity, and limits tuning to a single, physically interpretable parameter: window spectral transmittance. The procedure scales the measured transmittance while preserving its spectral shape and selects the option that minimizes 18-channel irradiance discrepancies on a control sensor. Implemented with *Radiance v6.0* single-pass hyperspectral rendering, the workflow is compatible with scripted and repeatable runs.

The results show that simulated spectral shapes agree well with field measurements across window options (correlations ≈ 0.89–0.91), which explains the stability of the melanopic/photopic (M/P) ratio. After calibration, systematic bias on the control sensor is largely removed for E_v and m-EDI: $\mathrm{MBE}_{\mathrm{rel}}$ is within 11%, overall error magnitude and dispersion decrease to $\mathrm{RMSE}_{\mathrm{rel}} \approx 14\%$ and $\sigma_{\mathrm{rel}} \approx 10\%$. The calibrated window has a lower magnitude than the measured base spectrum, consistent with the adopted strategy of preserving spectral shape while accounting for dominant external boundary effects.

Errors are spatially dependent. Sensors farther from the façade show larger bias and dispersion than the control sensor, reflecting increased sensitivity to inter-reflections and local modelling. These patterns delineate where residual discrepancies persist and indicate that, beyond transmittance, geometry and interior surface descriptions remain influential in deeper regions of the room.

The workflow is constrained by several factors. The study uses a single room, a short monitoring period, and overcast conditions. While *Radiance* has a record of validation for illuminance, its hyperspectral pipeline has not yet been validated against field

measurements; the present findings address this gap only indirectly through error reduction and spectral-shape agreement.

In summary, short in situ measurements combined with transmittance scaling provide a practical calibration pathway that reduces bias for E_v and m-EDI and preserves M/P stability.

7 Conclusions, Reflections and Future Research

7.1 Conclusions

This dissertation addressed key challenges of accurate and efficient daylight modelling in existing buildings. Despite the maturity of physically-based simulation tools, their application to real indoor environments remains constrained by difficulties in acquiring, defining, and validating the essential model inputs. These limitations manifest at multiple stages: reconstructing the indoor geometry in a way that satisfies the requirements of daylight models; characterising the optical properties of materials with sufficient accuracy and scalability; and calibrating simulation models. Each of these aspects represents a bottleneck that limits the reliability and broader applicability of daylight simulations in post-occupancy studies and retrofit analyses.

Building on these challenges, the subsequent sections summarise how this dissertation addressed them through five research questions. Each question targets one of the identified bottlenecks in daylight modelling: the effect of geometrical completeness, the influence of material accuracy, the reconstruction of indoor geometry from point clouds, the applicability of image-based material characterisation, and the calibration of spectral simulation models. Together, these results form an integrated overview of how the accuracy, effort, and reliability of indoor daylight simulations can be improved in practice.

7.1.1 Answers to the research questions

7.1.1.1 RQ1: How sensitive are Climate-based daylight modelling (CBDM) results to geometric levels of detail?

A new framework for defining indoor Geometrical Levels of Detail (GLoDs) was introduced to quantify the influence of geometrical completeness on CBDM results. Five GLoDs were defined by the size-wise inclusion of non-permanent indoor objects based on their Oriented Bounding Box (OBB) area from GLoD0 that included only the permanent elements of the room (walls, windows, floors, and ceilings), to GLoD4 which represented the most complete geometry, containing all indoor objects.

The intermediate GLoD1, GLoD2, and GLoD3 were defined by excluding objects smaller than 3.0, 2.4, and 0.5 m^2 of OBB area. This data-driven discretization allowed for the systematic evaluation of how gradually excluding non-permanent objects affects CBDM outputs.

Gradual exclusion of non-permanent objects from GLoD4 to GLoD0 caused on

average 1.08%, 6.55%, 11.21%, and 18.05% errors in the Total Annual Illumination (TAI) values, respectively. The spatial distribution of errors indicated that the largest deviations occurred around the locations of non-permanent objects, caused by their obstruction of daylight reaching nearby grid points. The magnitude of errors was higher in spaces with dense furniture arrangements (*e.g.*, *DA_200* and *MH_440*) and lower in more open spaces (*e.g.*, *W01050* and *DA_230*).

Excluding non-permanent objects also reduced the simulation time by up to three times, depending on the number and mesh complexity of objects in the model. The analysis revealed that GLoD2 models result in less than 15% error in TAI. This suggests that removing objects with OBB area smaller than 2.4 m^2 has a negligible impact on the results. In an office setting, such objects typically include desks, shelf contents, Air Conditioning (AC) units, certain chairs and lecterns, small radiators, flower boxes, and video projectors.

In summary, the work establishes a quantitative framework to determine the acceptable balance between geometrical completeness, computational cost, and predictive accuracy in CBDM.

7.1.1.2 RQ2 – What are the uncertainties caused by inaccurate material definition in CBDM results?

A concept of Material Classes of Precision (MCoPs) was developed to quantify the influence of inaccurate material definitions on annual daylight predictions. The optical properties of materials were defined as a randomly picked value from a normal distribution centred around the ground truth. Four different distributions were used to represent four MCoPs, derived from 106 measurements of opaque materials using Average Hemispherical Reflectance (AHR) with a reflectance spectrophotometer as ground truth. Reflectance and transmittance information were chosen as the key material optical properties for uncertainty quantification. Specifically, four material classes of precision were defined as normal distributions with four spreads, represented by different standard deviations, from 0.05 to 0.20.

For each room, five different GLoDs and four MCoPs were generated, resulting in a matrix of 20 models with varying levels of material and geometrical detail and accuracy. For each of the cells in the GLoD-MCoP matrix, a Monte Carlo experiment with 500 iterations was run (60,000 simulations in total), with randomised material properties from a given MCoP. The CBDM simulations and the annual TAI metrics are done as described earlier, and Percentage Error (PE), Mean Absolute Percentage Error (MAPE), and Root Mean Squared Error (RMSE) were used as error measures.

Annual simulation results showed that the distribution of the TAI results widens consistently with increasing uncertainty in the definitions of materials. In contrast, the median TAI does not vary noticeably. The distribution of simulation errors for TAI

appears symmetric. However, according to the normality test results, the majority of these output distributions deviate from normality, indicating the presence of non-linear transformations in the simulation process.

The uncertainty in predicting the annual daylight simulation results increases linearly with material uncertainty across all spaces and GLoDs. In the most complete model (GLoD4), the uncertainty ranges from 10% in MCoP0.05 to 35% in MCoP0.2 for *W01050*, *DA_230*, and *DA_200*. This range is slightly narrower in *WBG550* and *WBG640* (10%–30%), and in *MH_440* it ranges from 5% for MCoP0.05 to 15% in MCoP0.2.

A spatial analysis of the errors showed that the illuminance estimation uncertainty is larger around the glazing, suggesting a dominant influence of transmittance uncertainty on illuminance prediction. This was supported in *W01050* and *WBG640* (horizontal gradients), while *MH_440* shows a stronger relative influence from reflectance uncertainty.

In summary, inaccurate material definitions introduce uncertainties that increase linearly with input material uncertainty (typically $\sim$10%–30% depending on the space), with larger errors near openings due to the influence of transmittance, and with generally symmetric but often non-normally distributed output errors. This framework provides a basis for evaluating the propagation of errors caused by inaccurate modelling of material optical properties in CBDM.

7.1.1.3 RQ3 – How can indoor geometries be efficiently reconstructed to meet the requirements of daylight simulation models?

A semi-automatic pipeline for reconstructing indoor geometries from point cloud data for daylight simulation is developed. The pipeline focuses on generating GLoD0 models—window-containing watertight enclosures of indoor spaces—with reduced manual effort. It comprises three steps: (1) preprocessing, (2) reconstruction of a window-less watertight permanent structure, and (3) reconstruction of window boundaries with reduced user interaction (wall selection, candidate window patch detection, user window patch selection via lasso, boundary regularisation, and trimming/extrusion).

The approach was evaluated on rooms of varying sizes, shapes, and window complexity and validated against manually reconstructed models. For all successfully reconstructed cases, the total modelling time, comprising both user interaction and automated processing, remained under 5 minutes. The results demonstrate absolute errors below 10% for UDI, with mean TAI percentage errors within 18% for rooms containing rectangular windows and up to 44% for those with non-rectangular windows. The DGP error remains under 4% (RMSE < 0.04).

The main advantages include the significantly reduced modelling time compared to manual modelling; guaranteed water tightness to ensure daylight only enters through transparent surfaces; inclusion of window extrusion so that window details affecting glare and reflected luminance are captured; reduced user interaction to mitigate false detections in window finding; and a symmetric-window prior that is more robust than strict rectangularity.

Limitations include the assumption of planar surfaces inherited from *PolyFit*, the absence of mullions and co-planar subsurfaces, challenges with non-rectangular and arched windows (*e.g.*, *DA200*), susceptibility to complex geometries (*e.g.*, failure in *OrangeHall*), omission of beams and columns, untested scalability to multi-room configurations, and manual removal of out-of-room points during preprocessing.

In summary, the proposed pipeline enables rapid generation of simulation-ready GLoD0 geometry with acceptable accuracy for CBDM and glare analysis.

7.1.1.4 RQ4 – To what extent can image-based material characterisation techniques be applied to simulated indoor daylight models?

The applicability of three image-based techniques—Illuminance-Proxy, Ferwerda, and Luo—for estimating material reflectance from images was evaluated, and their influence on daylight simulation accuracy was assessed. Additionally, a spectral uplifting method was implemented to derive full spectral reflectance from tristimulus data for non-visual daylight simulations.

The results demonstrate that their accuracy varies considerably. Ferwerda's method, which estimates tristimulus reflectance using simple phone photography and chromatic adaptation, achieved the best balance between accessibility and accuracy. It produced a MRB of 13% and an RMSRE of 31%, with stable performance under different lighting conditions (MRB = 12%–16%). The resulting TAI errors ranged between 33%–65%, depending on illumination conditions, while the DGP errors remained below 0.02, indicating negligible influence on glare prediction. Its key advantage lies in requiring no controlled lighting or calibration setup, making it highly suitable for field applications.

Luo's deep-learning-based method, while capable of estimating diffuse and specular components, roughness, and normal maps, showed the most significant errors in reflectance estimation ($\Delta\rho$ up to 0.48, and ΔE_{ab} up to 70). It resulted in a substantial overestimation of daylight availability (TAI error of around 134%). The need for controlled flash illumination and its bias towards lower reflectances suggest limited transferability from synthetic to real-world conditions.

The Illuminance-Proxy method reconstructed spatially continuous reflectance maps

using sparse reference points and High Dynamic Range (HDR) luminance images. Despite its physical consistency, its accuracy depended strongly on the availability and precision of ground truth data. On a room scale, it yielded an MRB of 19% and RMSRE of 41%, but with an overestimation of TAI by about 101%. It performed best on diffuse, planar surfaces and under smoothly varying illumination but was sensitive to specular materials and sharp lighting gradients.

Spectral uplifting based on Jakob and Hanika's method reconstructed full spectral reflectance from RGB inputs with an RMSRE of below 20% across the visible range, leading to a deviation of less than 6% in predicted Melanopic equivalent daylight illuminance (m-EDI). This result confirms that tristimulus-based image techniques, when coupled with uplifting, can support non-visual and spectral daylight simulations with small added uncertainty.

In summary, image-based material characterisation techniques can provide practical, low-cost alternatives to laboratory-based measurements for daylight modelling. Among them, Ferwerda's approach offers the most robust trade-off between simplicity, scalability, and accuracy. Illuminance-Proxy is beneficial for spatially detailed reflectance mapping when partial ground truth is available. Luo's method, while automated, requires further adaptation for real indoor scenes. Spectral uplifting extends these methods to circadian and hyperspectral applications with negligible loss of accuracy.

7.1.1.5 RQ5 – How can simulated spectral indoor models be calibrated to account for uncertainties in scene reconstruction?

A calibration workflow for indoor spectral daylight simulation was introduced and validated that addresses dominant uncertainties in scene reconstruction, namely: (1) sun–sky conditions, (2) exterior obstructions, and (3) window spectral transmittance. The first two are typically beyond the practitioner's control during short on-site measurements, while the third is both highly variable and influential. The workflow therefore prioritises inputs by their characterisation uncertainty and output sensitivity, selecting window spectral transmittance as the single tunable parameter. The calibration scales the measured transmittance spectrum up or down while preserving its spectral shape, and identifies the best-performing option by minimizing 18-channel irradiance errors against field measurements.

The procedure was tested in a university classroom in Toronto under overcast sky conditions. Spectral irradiance was measured at four indoor points and one control point near the window using a Konica Minolta CL-500A spectroradiometer. The simulated model, developed in *Radiance v6.0* using single-pass hyperspectral rendering, was calibrated by iteratively adjusting window transmittance across 16 scaled options. The Mean Absolute Error (MAE) was used to select the optimal transmittance, followed by performance evaluation using MBE_{rel}, RMSE_{rel}, and σ_{rel}

for photopic (E_v), melanopic (m-EDI), and M/P ratio outputs. The results show strong agreement between simulated and measured spectral shapes even before calibration (Pearson $r = 0.89$–0.92), explaining the stability of the M/P ratio ($\mathrm{RMSE}_{\mathrm{rel}} < 10\%$). After calibration, systematic bias in both E_v and m-EDI was nearly eliminated on the control sensor ($\mathrm{MBE}_{\mathrm{rel}} = -5.8\%$ and 2.7%), while total error magnitude dropped to $\mathrm{RMSE}_{\mathrm{rel}} \approx 18\%$ and random dispersion to $\sigma_{\mathrm{rel}} \approx 18\%$. Residual spatial errors increased with distance from the façade, indicating that inter-reflections and local modelling inaccuracies dominate at greater depths in the room.

In summary, the proposed workflow provides a method for calibrating spectral daylight simulations of existing rooms using short-term field data. By tuning only window transmittance while preserving its spectral form, it reduces bias in photopic and melanopic predictions and maintains M/P stability. The workflow is fully compatible with automated pipelines and scalable to large datasets, offering a reproducible approach for improving the reliability of spectral daylight simulations in real-world applications.

7.2 Key Contributions

This PhD research developed and validated a comprehensive framework for constructing, evaluating, and calibrating digital indoor models for daylight and spectral simulation. The work advances the state of knowledge across five areas, namely geometry, materials, automation, image-based techniques, and spectral calibration, each contributing to the overarching goal of enabling experts to obtain valid indoor digital models with reduced error, effort, and time.

- **Chapter 2 (RQ1).** A new framework for defining indoor Geometrical Levels of Detail (GLoDs) was introduced, ranging from GLoD0 (permanent objects only) to GLoD4 (complete geometry). The levels were determined by size-wise inclusion of non-permanent objects based on their Oriented Bounding Box (OBB) area. The study quantified how reducing geometrical completeness affects daylight performance, which shows that simplifications can significantly reduce simulation time—up to threefold—while maintaining acceptable accuracy. Models at GLoD2, which exclude objects smaller than 2.4 m^2, produced less than 15% error in annual illuminance.
- **Chapter 3 (RQ2).** To evaluate the effect of uncertain material definitions, a concept of Material Classes of Precision (MCoPs) was developed based on 106 in-situ reflectance measurements. These accuracy classes, represented as normal distributions with varying spreads (0.05–0.20), were combined with the geometrical GLoDs in a Monte Carlo framework of 60,000 simulations across six rooms. The results showed that output errors increase linearly with input material uncertainty

(typically 10%–35%) and that transmittance inaccuracies have a greater influence on illuminance predictions than reflectance. The study provided a statistical basis for understanding and managing the propagation of material-related errors in daylight modelling.

- **Chapter 4 (RQ3).** A semi-automatic pipeline was developed to generate watertight, simulation-ready indoor models directly from point clouds. The method reconstructs walls, floors, ceilings, and windows with reduced user interaction, using regularisation and extrusion techniques to ensure geometric completeness and light-tightness. Across multiple case studies, models were reconstructed within five minutes and yielded daylight results with less than 10% UDI error and under 0.04 DGP RMSE. The approach demonstrated that reliable geometry can be obtained rapidly and reproducibly, thereby reducing manual modelling effort while maintaining photometric validity.

- **Chapter 5 (RQ4).** Three image-based reflectance estimation methods—Illuminance-Proxy, Ferwerda, and Luo—were systematically tested against spectrophotometer measurements and applied to daylight simulations. Ferwerda's method provided the best trade-off between simplicity and accuracy, achieving a mean bias error of 13% and stable results under varying illumination. The Illuminance-Proxy method proved effective for spatially continuous reflectance mapping but was sensitive to input precision, while Luo's deep-learning-based method showed high errors under real conditions. In addition, a spectral uplifting method was validated to extend these techniques to non-visual and hyperspectral applications, with deviations below 6% in melanopic illuminance.

- **Chapter 6 (RQ5).** A calibration method for spectral daylight simulation was established, targeting the most influential and uncertain parameter: window spectral transmittance. Using short-term in-situ measurements and hyperspectral rendering in *Radiance v6.0*, the method adjusted transmittance magnitude while preserving spectral shape to minimize errors. After calibration, the systematic bias in photopic and melanopic illuminance was reduced to within ±6%, with overall error magnitudes of around 18%. The approach demonstrated that physically interpretable, single-parameter calibration can effectively align measured and simulated spectral data.

Overall, this work provides quantitative evidence on where model simplification is acceptable, how uncertainty propagates through simulation workflows, and how limited field measurements can be used to achieve accurate simulated daylight models.

7.3 Future Work

This dissertation provides a foundation for the automation and formalisation of simulated daylight modelling in existing buildings. Several methodological and practical aspects remain open for exploration. The following subsections outline the main opportunities for future research aligned with the topics of Chapters 2–6.

7.3.1 Geometrical level of detail for indoor daylight simulation and sensitivity of daylight simulation results to geometry (RQ1)

This dissertation introduced a data-driven framework for defining geometric levels of detail (GLoDs) for indoor daylight simulations. Five GLoDs were defined based on the size-wise inclusion of non-permanent indoor objects using their oriented bounding box (OBB) area. The influence of geometric completeness on annual daylight availability was quantified across six case-study spaces, showing that removing objects smaller than 2.4 m^2 results in less than 15% error in TAI while significantly reducing computation time. The findings provide a quantitative basis for selecting sufficient geometric resolutions depending on desired accuracy and available resources. Future research can be structured around three directions to refine and extend this framework.

The current definition of GLoDs is based solely on object size, which introduces inherent limitations. Alternative definitions that consider other geometrical parameters beyond size—such as proximity to light sources—could provide a more complete understanding of how geometry affects daylight distribution. Moreover, incorporating directional or sensor-based metrics, rather than relying only on workplane-based evaluations, could capture variations in daylight propagation and visual perception more accurately. Finally, future research should address the geometry of permanent objects and explore bidirectional definitions of GLoDs—both via inclusion of non-permanent objects and reduction of geometric complexity through mesh simplification.

7.3.2 Material classes of precision and sensitivity of daylight simulation results to material characterisation (RQ2)

This work quantified the uncertainty in daylight simulations caused by inaccurate material definitions and introduced the concept of MCoPs, combining geometric and

material factors in a Monte Carlo framework to characterise how input uncertainty propagates to annual metrics. Future work can advance this framework in four key directions.

First, the proposed MCoPs were defined only based on measurement precision, while accuracy should also be incorporated in future studies. Second, extending this framework to include spectral information would enable a more comprehensive characterisation of material behaviour supporting both photopic and non-visual daylight assessments. Third, incorporating spectral and directional components into the MCoP definitions would capture wavelength- and angle-dependent behaviours relevant to glare and circadian studies. Finally, validation through controlled indoor experiments comparing simulated and measured illuminance and luminance for different MCoPs, together with applying a broader set of metrics—including glare indices, circadian indicators (m-EDI, CS), and visual comfort metrics—would help verify the modelled uncertainty ranges and improve result credibility.

7.3.3 Semi-automated reconstruction of indoor geometry for daylight simulation (RQ3)

This chapter developed a semi-automated pipeline that reconstructs watertight, window-containing GLoD0 indoor geometries from point clouds with reduced user input, achieving under-five-minute modelling times. Future work can proceed in three main directions to enhance robustness and scalability.

First, the method should be extended to generate more detailed geometrical representations (GLoD+) according to the required accuracy, which varies with the final application. Second, curved and non-planar geometries, complex or arched windows, mullions, co-planar subsurfaces, beams, and columns are not fully reconstructed due to planar assumptions and limitations inherited from *PolyFit*. These omissions have led to overestimated daylight predictions. Identifying and quantifying such errors can guide algorithmic improvements through enhanced boundary regularisation, curved-surface detection, and automated modelling of secondary architectural features. Finally, scalability and reproducibility should be assessed. The current approach has been validated on single-room point clouds only. Multi-room and multi-storey scalability, multi-user reproducibility studies, and automated room isolation during preprocessing would further reduce manual effort and ensure consistency.

7.3.4 Image-based material characterisation for daylight simulation (RQ4)

This chapter evaluated three image-based techniques—Illuminance-Proxy, Ferwerda, and Luo—for estimating material reflectance from images, and implemented a spectral uplifting method to derive full spectral reflectance from tristimulus data for non-visual daylight simulations. Future research can expand on three directions.

First, the implementation of image-based material characterisation should move from per-sample to per-scene estimation, which requires further verification under realistic indoor lighting conditions. Second, evaluating the applicability of scene-wide image-based methods in daylight simulations remains essential, particularly where lighting gradients, inter reflections, and specularities are significant. Finally, even though performance is promising, future implementations of spectral daylight simulations should better justify the choice of uplifting technique. Investigating more recent uplifting methods for spectral lighting evaluation would strengthen this justification and potentially improve accuracy.

7.3.5 Calibration of spectral daylight simulation models (RQ5)

This chapter introduced and validated a calibration workflow for indoor spectral daylight simulation that tunes window spectral transmittance while preserving spectral shape to reduce bias and uncertainty in photopic and melanopic predictions. Future developments can advance this framework along three primary directions.

First, calibration methods should explicitly address spatial discrepancies within indoor spectral models through localised calibration, and multi-sensor weighting. Second, generalisation across spaces and skies should be tested under diverse configurations and sky conditions, with extended monitoring to capture temporal variability and transient effects. Finally, spatial performance mapping, integration with electric lighting, and benchmarking across different simulation engines (e.g., Lark, ALFA) will help evaluating consistency, scalability, and applicability to mixed-mode lighting environments.

References

Abdollahzadeh, N., Tahsildoost, M., and Zomorodian, Z. S. (2020). A method of partition design for open-plan offices based on daylight performance evaluation. Journal of Building Engineering, 29:101171.

Adán, A., Ramón, A., Vivancos, J. L., Vilar, A., and Aparicio-Fernández, C. (2023). Automatic generation of as-is BEM models of buildings. Journal of Building Engineering, 73:106865.

Agarwal, M., Pastore, L., and Andersen, M. (2024). Risk of incorrect choices due to uncertainty in BPS evaluations of conceptual-stage neighbourhood-scale building designs. Journal of Building Performance Simulation, 17(2):234–252.

Ámundadóttir, M. L. (2016). Light-driven model for identifying indicators of non-visual health potential in the built environment. PhD thesis, Ecole Polytechnique Fédérale de Lausanne.

Assi, R., Landes, T., Macher, H., and Grussenmeyer, P. (2019). Energy function algorithm for detection of openings in indoor point clouds. The International Archives of Photogrammetry, Remote Sensing and Spatial Information Sciences, 42:747–752.

Bellia, L., Pedace, A., and Fragliasso, F. (2017). Indoor lighting quality: Effects of different wall colours. Lighting Research & Technology, 49(1):33–48.

Benner, J., Geiger, A., Gröger, G., Häfele, K.-H., and Löwner, M.-O. (2013). Enhanced LOD concepts for virtual 3D city models. In ISPRS annals of the photogrammetry, remote sensing and spatial information sciences. Proceedings of the ISPRS 8th 3D GeoInfo conference & WG II/2 workshop, pages 51–61.

Bian, Y., Luo, J., Hu, J., Liu, L., and Pang, Y. (2021). Visual discomfort assessment in an open-plan space with skylights: A case study with poe survey and retrofit design. Energy and Buildings, 248:111215.

Biljecki, F., Ledoux, H., and Stoter, J. (2016). An improved LOD specification for 3D building models. Computers, Environment and Urban Systems, 59:25–37.

Billen, R., Zaki, C., Servières, M., Moreau, G., and Hallot, P. (2012). Developing an ontology of space: Application to 3D city modeling. Usage, Usability, and Utility of 3D City Models–European COST Action TU0801, page 02007.

Bodart, M., de Peñaranda, R., Deneyer, A., and Flamant, G. (2008). Photometry and colorimetry characterisation of materials in daylighting evaluation tools. Building and Environment, 43(12):2046–2058.

Boeters, R., Arroyo Ohori, K., Biljecki, F., and Zlatanova, S. (2015). Automatically enhancing CityGML LOD2 models with a corresponding indoor geometry. International Journal of Geographical Information Science, 29(12):2248–2268.

Bognár, Á., Loonen, R. C., and Hensen, J. L. (2021). Calculating solar irradiance without shading geometry: a point cloud-based method. Journal of Building Performance Simulation, 14(5):480–502.

Brainard, G. C., Hanifin, J. P., Greeson, J. M., Byrne, B., Glickman, G., Gerner, E., and Rollag, M. D. (2001). Action spectrum for melatonin regulation in humans: evidence for a novel circadian photoreceptor. Journal of Neuroscience, 21(16):6405–6412.

Brembilla, E., Hopfe, C. J., and Mardaljevic, J. (2018). Influence of input reflectance values on climate-based daylight metrics using sensitivity analysis. Journal of Building Performance Simulation, 11(3):333–349.

Brown, T. M., Brainard, G. C., Cajochen, C., Czeisler, C. A., Hanifin, J. P., Lockley, S. W., Lucas, R. J., Münch, M., O'Hagan, J. B., Peirson, S. N., et al. (2022). Recommendations for daytime, evening, and nighttime indoor light exposure to best support physiology, sleep, and wakefulness in healthy adults. PLoS biology, 20(3):e3001571.

Building Research Establishment (BRE) (2023). BREEAM - Building Research Establishment Environmental Assessment Method. `https://www.breeam.com/`. Accessed July 2023.

Cai, H. (2013). High dynamic range photogrammetry for synchronous luminance and geometry measurement. Lighting Research & Technology, 45(2):230–257.

CEN (2018). EN 17037: Daylight in buildings.

Chakraborty, R., Ostrin, L. A., Nickla, D. L., Iuvone, P. M., Pardue, M. T., and Stone, R. A. (2018). Circadian rhythms, refractive development, and myopia. Ophthalmic and Physiological Optics, 38(3):217–245.

Chandraker, M. and Ramamoorthi, R. (2011). What an image reveals about material reflectance. In 2011 International Conference on Computer Vision, pages 1076–1083. IEEE.

CIBSE (1999). Lighting guide lg10. Chartered Institution of Building Services Engineers.

Coakley, D., Raftery, P., and Keane, M. (2014). A review of methods to match building energy simulation models to measured data. Renewable and sustainable energy reviews, 37:123–141.

Crawley, D. and Lawrie, L. (2019). Climate. onebuilding. org. http s://climate. onebuilding. org/default. html.[Accessed 25 3 2022].
D'agostino, R. and Pearson, E. S. (1973). Tests for departure from normality. empirical results for the distributions of b2 and squeare root of b. Biometrika, 60(3):613–622.
De La Barra, P., Brembilla, E., Prieto, A., Vásquez, C., Knaack, U., and Luna-Navarro, A. (2025). Influence of automated façades on comfort and energy: A critical review. Energy and Buildings, page 116290.
Delft High Performance Computing Centre DHPC (2024). DelftBlue Supercomputer (Phase 2). `https://www.tudelft.nl/dhpc/ark:/44463/DelftBluePhase2`.
Deschaintre, V., Aittala, M., Durand, F., Drettakis, G., and Bousseau, A. (2018). Single-Image SVBRDF Capture with a Rendering-Aware Deep Network. ACM Transactions on Graphics, 37(4).
Díaz-Vilariño, L., Lagüela, S., Armesto, J., and Arias, P. (2014). Indoor daylight simulation performed on automatically generated as-built 3D models. Energy and Buildings, 68:54–62.
Fabri, A. and Pion, S. (2009). CGAL: The computational geometry algorithms library. In Proceedings of the 17th ACM SIGSPATIAL international conference on advances in geographic information systems, pages 538–539.
Ferwerda, J. A. (2018). Lightweight estimation of surface BRDFs. Journal of Imaging Science and Technology, 62(5):50407–1.
Fischler, M. A. and Bolles, R. C. (1981). Random sample consensus: a paradigm for model fitting with applications to image analysis and automated cartography. Communications of the ACM, 24(6):381–395.
for Standardization (ISO), I. O. and on Illumination (CIE), I. C. (2019). Colorimetry — Part 1: CIE standard colorimetric observers. Identical to EN ISO/CIE 11664-1:2019 and NEN-EN-ISO/CIE 11664-1:2019.
Forouzandeh, N., Brembilla, E., Nan, L., Stoter, J., and Jakubiec, A. (2024). Influence of geometrical levels of detail and inaccurate material optical properties on daylight simulation. Energy and Buildings, 306:113924.
Forouzandeh Shahraki, N., Brembilla, E., and Jakubiec, J. A. (2022). Image-based material characterization for daylight simulation using illuminance-proxy and artificial neural networks. In Proceedings of the 14th European Lighting Conference LUX EUROPA.
Fotsing, C., Tchuitcheu, W. C., Besong, L. I., Cunningham, D. W., and Bobda, C. (2024). A specialized pipeline for efficient and reliable 3d semantic model reconstruction of buildings from indoor point clouds. Journal of Imaging, 10(10):261.
Garwood, T. L., Hughes, B. R., O'Connor, D., Calautit, J. K., Oates, M. R., and Hodgson, T. (2017). Geometry extraction for high resolution building energy modelling applications from point cloud data: a case study of a factory facility. Energy Procedia, 142:1805–1810.
Geisler-Moroder, D., Lee, E. S., and Ward, G. J. (2016). Validation of the five-phase method for simulating complex fenestration systems with Radiance against field measurements. Technical report, Lawrence Berkeley National Lab.(LBNL), Berkeley, CA (United States).
Ghansah, F. A. (2024). Digital twins for smart building at the facility management stage: a systematic review of enablers, applications and challenges. Smart and Sustainable Built Environment, 14(4):1194–1229.
Gkaintatzi-Masouti, M., van Duijnhoven, J., and Aarts, M. P. (2021). Review of spectral lighting simulation tools for non-image-forming effects of light. In Journal of Physics: Conference Series, volume 2042, page 012122. IOP Publishing.
Grobe, L. O. and Jakubiec, J. A. (2023). Impact of model detail on daylighting metrics in residential buildings. In Journal of Physics: Conference Series, volume 2600, page 112010. IOP Publishing.
Guideline, A. et al. (2014). ASHRAE Guideline 14-2014: Measurement of Energy, Demand, and Water Savings. Technical report, American Society of Heating, Refrigerating and Air-Conditioning Engineers (ASHRAE), Atlanta, GA. ASHRAE Guideline 14-2014.
Hagedorn, B., Trapp, M., Glander, T., and Döllner, J. (2009). Towards an indoor level-of-detail model for route visualization. In 2009 Tenth International Conference on Mobile Data Management: Systems, Services and Middleware, pages 692–697.
Hartman, P., Hanuliak, P., Maňková, L., and Hraška, J. (2014). The effect of the colour selection for internal surfaces on non-visual daylight human response. Advanced Materials Research, 1057:231–240.
Hashemi, A. (2014). Daylighting and solar shading performances of an innovative automated reflective louvre system. Energy and Buildings, 82:607–620.
He, S., Yan, Y., and Cai, H. (2022). Improving the accuracy of circadian lighting simulation with field measurement. Journal of Building Performance Simulation, 15(5):575–598.
Heschong, L. (1999). Daylighting in schools: An investigation into the relationship between daylighting and human performance. detailed report. ERIC.
Heschong, L. (2006). Windows and office worker performance. Creating the Productive Workplace; Taylor & Francis: London, UK, page 277.
Huang, J., Stoter, J., and Nan, L. (2023). Symmetrization of 2D Polygonal Shapes Using Mixed-Integer Programming. Computer-Aided Design, page 103572.
IEA (2011). Prefabricated systems for low energy renovation of residential buildings. Retrofit Module Design Guide, EMPA, Duebendorf, marzo.
International WELL Building Institute (IWBI) (2023). Well V2 standard. `https://v2.wellcertified.com/v/en/concepts`. Accessed July 2023.
Jakob, W. and Hanika, J. (2019). A low-dimensional function space for efficient spectral upsampling. Computer Graphics Forum (Proceedings of Eurographics), 38(2).
Jakubiec, A. (2022). Spectral Materials Database. `http://spectraldb.com/`.

Jiang, F., Ma, L., Broyd, T., and Chen, K. (2021). Digital twin and its implementations in the civil engineering sector. Automation in Construction, 130:103838.
Jones, N. L. and Reinhart, C. F. (2015). Validation of Gpu Lighting Simulation in Naturally And Artificially Lit Spaces. In Proceedings of Building Simulation 2015: 14th Conference of IBPSA, volume 14 of Building Simulation, pages 1229–1236, Hyderabad, India. IBPSA.
Jones, N. L. and Reinhart, C. F. (2017). Experimental validation of ray tracing as a means of image-based visual discomfort prediction. Building and Environment, 113:131–150.
Jradi, M., Veje, C., and Jørgensen, B. N. (2017). Deep energy renovation of the mærsk office building in denmark using a holistic design approach. Energy and Buildings, 151:306–319.
Jung, J., Stachniss, C., Ju, S., and Heo, J. (2018). Automated 3D volumetric reconstruction of multiple-room building interiors for as-built BIM. Advanced Engineering Informatics, 38:811–825.
Kavoosighafi, B., Hajisharif, S., Miandji, E., Baravdish, G., Cao, W., and Unger, J. (2024). Deep SVBRDF Acquisition and Modelling: A Survey. In Computer Graphics Forum, volume 43, page e15199. Wiley Online Library.
Kellner, M., Stahl, B., and Reiterer, A. (2023). Reconstructing geometrical models of indoor environments based on point clouds. Remote Sensing, 15(18):4421.
Kemec, S., Zlatanova, S., and Duzgun, S. (2012). A new LoD definition hierarchy for 3D city models used for natural disaster risk communication tool. In Proceedings of the 4th International Conference on Cartography & GIS, Volume 2, Albena, June 2012, pp. 17-28. International Cartographic Association.
Kharvari, F. (2020). An empirical validation of daylighting tools: Assessing radiance parameters and simulation settings in Ladybug and Honeybee against field measurements. Solar Energy, 207:1021–1036.
Kim, M. and Tzempelikos, A. (2021). Semi-automated luminance map re-projection via high dynamic range imaging and indoor space 3-D reconstruction. Automation in Construction, 129:103812.
Kim, M. and Tzempelikos, A. (2022). Performance evaluation of non-intrusive luminance mapping towards human-centered daylighting control. Building and Environment, 213:108857.
Kim, Y. S., Shin, H. S., and Park, C. S. (2022). Model predictive lighting control for a factory building using a deep deterministic policy gradient. Journal of Building Performance Simulation, 15(2):174–193.
Klepeis, N. E., Nelson, W. C., Ott, W. R., Robinson, J. P., Tsang, A. M., Switzer, P., Behar, J. V., Hern, S. C., and Engelmann, W. H. (2001). The National Human Activity Pattern Survey (NHAPS): a resource for assessing exposure to environmental pollutants. Journal of Exposure Science & Environmental Epidemiology, 11(3):231–252.
Knoop, M., Stefani, O., Bueno, B., Matusiak, B., Hobday, R., Wirz-Justice, A., Martiny, K., Kantermann, T., Aarts, M. P., Zemmouri, N., et al. (2020). Daylight: What makes the difference? Lighting Research & Technology, 52(3):423–442.
Koh, W. S., Liu, H., Somasundaram, S., Thangavelu, S. R., Chong, A., Pillai, K., Kojima, H., and Mori, Y. (2020). Evaluation of glazing retrofitting solution for the tropics. Energy and Buildings, 223:110190.
Köse, F. B., Tayfur, G., Duran, H. E., and Kazanasmaz, Z. T. (2022). Lighting quality and work performance based on glazing types and dynamic LED Lighting. In 2021 Joint Conference-11th International Conference on Energy Efficiency in Domestic Appliances and Lighting & 17th International Symposium on the Science and Technology of Lighting (EEDAL/LS: 17), pages 1–6. IEEE.
Küller, R., Ballal, S., Laike, T., Mikellides, B., and Tonello, G. (2006). The impact of light and colour on psychological mood: a cross-cultural study of indoor work environments. Ergonomics, 49(14):1496–1507.
Kunwar, N., Cetin, K. S., and Passe, U. (2021). Calibration of energy simulation using optimization for buildings with dynamic shading systems. Energy and Buildings, 236:110787.
Kurkela, M., Maksimainen, M., Julin, A., Rantanen, T., Virtanen, J.-P., Hyyppä, J., Vaaja, M. T., and Hyyppä, H. (2021). Utilizing a Terrestrial Laser Scanner for 3D Luminance Measurement of Indoor Environments. Journal of Imaging, 7(5):85.
Kurkela, M., Maksimainen, M., Julin, A., Virtanen, J.-P., Männistö, I., Vaaja, M. T., and Hyyppä, H. (2022). Applying photogrammetry to reconstruct 3D luminance point clouds of indoor environments. Architectural Engineering and Design Management, 18(1):56–72.
Kutzner, T., Chaturvedi, K., and Kolbe, T. H. (2020). Citygml 3.0: New functions open up new applications. PFG–Journal of Photogrammetry, Remote Sensing and Geoinformation Science, 88(1):43–61.
Larson, G. W. and Shakespeare, R. (1998). Rendering with Radiance: the art and science of lighting visualization. Morgan Kaufmann Publishers Inc.
Lee, E., Geisler-Moroder, D., and Ward, G. (2018). Validation of the five-phase method for simulating complex fenestration systems with radiance against field measurements. Lawrence Berkeley National Laboratory.
Lee, E. S., Claybaugh, E. S., and LaFrance, M. (2012). End user impacts of automated electrochromic windows in a pilot retrofit application. Energy and Buildings, 47:267–284.
Lee, E. S., Matusiak, B. S., Geisler-Moroder, D., Selkowitz, S. E., and Heschong, L. (2022). Advocating for view and daylight in buildings: Next steps. Energy and Buildings, 265:112079.
Li, J., Xiong, B., Qin, R., and Gruen, A. (2020). A flexible inference machine for global alignment of wall openings. Remote Sensing, 12(12):1968.
Li, P., Froese, T. M., and Brager, G. (2018). Post-occupancy evaluation: State-of-the-art analysis and state-of-the-practice review. Building and Environment, 133:187–202.
Lim, Y.-W., Ahmad, M. H., and Ossen, D. R. (2010). Empirical validation of daylight simulation tool with physical model measurement. American Journal of Applied Sciences, 7(10):1426.

Luo, X., Scandolo, L., Bousseau, A., and Eisemann, E. (2024). Single-image svbrdf estimation with learned gradient descent. Computer Graphics Forum (Proc. Eurographics), 43(2).
Ma, Z., Cooper, P., Daly, D., and Ledo, L. (2012). Existing building retrofits: Methodology and state-of-the-art. Energy and Buildings, 55:889–902. Cool Roofs, Cool Pavements, Cool Cities, and Cool World.
Mangkuto, R., Aries, M., van Loenen, E., and Hensen, J. (2014). Simulation study of a virtual natural lighting solutions prototype: validation and analysis. In Experiencing Light 2014: International Conference on the Effects of Light on Wellbeing, pages 54–57.
Mardaljevic, J. (1995). Validation of a lighting simulation program under real sky conditions. International Journal of Lighting Research and Technology, 27(4):181–188.
Mardaljevic, J. (2015). Climate-based daylight modelling and its discontents. Loughborough University.
Mardaljevic, J., Andersen, M., Roy, N., Christoffersen, J., et al. (2012). Daylighting metrics: is there a relation between useful daylight illuminance and daylight glare probability. In Proceedings of the building simulation and optimization conference (BSO12), Loughborough, UK, volume 1011.
Mardaljevic, J., Brembilla, E., Cannon-Brookes, S., and Blades, N. (2021). A hybrid measurement-simulation approach to determine the reflectance map of a historic tapestry. In Building Simulation 2021 Conference: BS2021. International Building Performance Simulation Association.
Mardaljevic, J., Brembilla, E., and Drosou, N. (2015). Illuminance-proxy high dynamic range imaging: a simple method to measure surface reflectance. Loughborough University.
Markovic, M., Olesen, S. K., and Hammershoi, D. (2013). Three-dimensional point-cloud room model for room acoustics simulations. In Proceedings of Meetings on Acoustics, volume 19, page 015122. Acoustical Society of America.
McNeil, A., Jonsson, C., Appelfeld, D., Ward, G., and Lee, E. S. (2013). A validation of a ray-tracing tool used to generate bi-directional scattering distribution functions for complex fenestration systems. Solar Energy, 98:404–414.
Mehranfar, M., Vega-Torres, M. A., Braun, A., and Borrmann, A. (2024). Automated data-driven method for creating digital building models from dense point clouds and images through semantic segmentation and parametric model fitting. Advanced Engineering Informatics, 62:102643.
Michailidis, G.-T. and Pajarola, R. (2017). Bayesian graph-cut optimization for wall surfaces reconstruction in indoor environments. The Visual Computer, 33:1347–1355.
Naik, N., Zhao, S., Velten, A., Raskar, R., and Bala, K. (2011). Single view reflectance capture using multiplexed scattering and time-of-flight imaging. In Proceedings of the 2011 SIGGRAPH Asia conference, pages 1–10.
Nan, L. (2021). Easy3D: a lightweight, easy-to-use, and efficient C++ library for processing and rendering 3D data. Journal of Open Source Software, 6(64):3255.
Nan, L. and Wonka, P. (2017). Polyfit: Polygonal surface reconstruction from point clouds. In Proceedings of the IEEE International Conference on Computer Vision, pages 2353–2361.
Ochmann, S., Vock, R., Wessel, R., and Klein, R. (2016). Automatic reconstruction of parametric building models from indoor point clouds. Computers & Graphics, 54:94–103.
Orman, A., Safranek, S., and Pierson, C. (2025). Evaluation of spectral light simulation tools for prediction of iprgc-influenced light responses in real-world offices with electrochromic glazing. Journal of Building Performance Simulation, pages 1–20.
Pan, Y., Braun, A., Borrmann, A., and Brilakis, I. (2022). 3D deep-learning-enhanced void-growing approach in creating geometric digital twins of buildings. Proceedings of the Institution of Civil Engineers-Smart Infrastructure and Construction, 176(1):24–40.
Pang, Z., O'Neill, Z., Li, Y., and Niu, F. (2020). The role of sensitivity analysis in the building performance analysis: A critical review. Energy and Buildings, 209:109659.
Perez, R., Ineichen, P., Seals, R., Michalsky, J., and Stewart, R. (1990). Modeling daylight availability and irradiance components from direct and global irradiance. Solar Energy, 44(5):271–289.
Peters, C., Merzbach, S., Hanika, J., and Dachsbacher, C. (2019). Using moments to represent bounded signals for spectral rendering. ACM Transactions on Graphics (TOG), 38(4):1–14.
Pierson, C., Aarts, M. P., and Andersen, M. (2023). Validation of spectral simulation tools in the context of iprgc-influenced light responses of building occupants. Journal of Building Performance Simulation, 16(2):179–197.
Potočnik, J. and Košir, M. (2020). Influence of commercial glazing and wall colours on the resulting non-visual daylight conditions of an office. Building and Environment, 171:106627.
Previtali, M., Díaz-Vilariño, L., and Scaioni, M. (2018). Indoor building reconstruction from occluded point clouds using graph-cut and ray-tracing. Applied Sciences, 8(9):1529.
Quek, G. and Jakubiec, J. A. (2021). Calibration and validation of climate-based daylighting models based on one-time field measurements: Office buildings in the tropics. Leukos, 17(1):75–90.
Radiance (2022). ral-colors — Radsite.
Regnier, C., Sun, K., Hong, T., and Piette, M. A. (2018). Quantifying the benefits of a building retrofit using an integrated system approach: A case study. Energy and Buildings, 159:332–345.
Roberts, S. (2008). Altering existing buildings in the UK. Energy policy, 36(12):4482–4486.
Rodrigue, M., Demers, C. M., and Parsaee, M. (2022). Lighting in the third dimension: Laser scanning as an architectural survey and representation method. Intelligent Buildings International, 14(2):222–238.
Sadeghi, R. and Mistrick, R. (2022). The impact of exterior surround detail on daylighting simulation results. LEUKOS, 18(3):341–356.

Shi, W., Ahmed, W., Li, N., Fan, W., Xiang, H., and Wang, M. (2018). Semantic geometric modelling of unstructured indoor point cloud. ISPRS international journal of geo-information, 8(1):9.
Skartveit, A. and Olseth, J. A. (1987). A model for the diffuse fraction of hourly global radiation. Solar energy, 38(4):271–274.
Smit, M. (2022). Deducing the Location of Glass Windows in 3D Indoor Environments. Master's thesis, Delft University of Technology.
Solemma LLC (2025). Custom daylight availability. `https://climatestudiodocs.com/docs/daylightCustom.html`. Accessed: 2025-10-16.
Soto Magán, V. (2021). Alertness in work environments. on the role of indoor daylight exposure. PhD diss., Ecole Polytechnique Fédérale de Lausanne (EPFL), Lausanne, Switzerland.
Stephens, M. A. (1974). EDF statistics for goodness of fit and some comparisons. Journal of the American statistical Association, 69(347):730–737.
Subramaniam, S. (2017). Daylighting simulations with Radiance using matrix-based methods. Lawrence Berke-ley National Laboratory.
Subramaniam, S. (2018). Parametric modeling strategies for efficient annual analysis of daylight in buildings. PhD thesis, Penn State.
Sunger, V. and Vaidya, P. (2019). Evaluation of daylight performance of the new workshop building at cept university, ahmedabad. In Building Simulation 2019, volume 16, pages 1160–1168. IBPSA.
Tabatabaei Manesh, M., Rajaian Hoonejani, M., Ghafari Gousheh, S., Abdolmaleki, A., Nikkhah Dehnavi, A., and Shahrashoob, A. (2025). Ai-driven control algorithm using machine learning and genetic optimization for enhancing visual comfort in adaptive façades. Automation in Construction, 179:106474.
Tang, P., Huber, D., Akinci, B., Lipman, R., and Lytle, A. (2010). Automatic reconstruction of as-built building information models from laser-scanned point clouds: A review of related techniques. Automation in construction, 19(7):829–843.
Tang, S., Zhang, Y., Li, Y., Yuan, Z., Wang, Y., Zhang, X., Li, X., Zhang, Y., Guo, R., and Wang, W. (2019). Fast and automatic reconstruction of semantically rich 3D indoor maps from low-quality RGB-D sequences. Sensors, 19(3):533.
Thapan, K., Arendt, J., and Skene, D. J. (2001). An action spectrum for melatonin suppression: evidence for a novel non-rod, non-cone photoreceptor system in humans. The Journal of physiology, 535(1):261–267.
Tódová, L., Wilkie, A., and Fascione, L. (2021). Moment-based constrained spectral uplifting. In EGSR (DL), pages 215–224.
Tregenza, P. and Wilson, M. (2013). Daylighting: architecture and lighting design. Routledge.
USGBC (2014). LEED v4 for building design and construction. USGBC Inc.
Valero, E., Mohanty, D. D., Ceklarz, M., Tao, B., Bosché, F., Giannakis, G. I., Fenz, S., Katsigarakis, K., Lilis, G. N., Rovas, D., et al. (2021). An integrated scan-to-BIM approach for buildings energy performance evaluation and retrofitting. In Proceedings of the International Symposium on Automation and Robotics in Construction, volume 2021, pages 204–211. ISARC.
Van De Ruit, M. and Eisemann, E. (2023). Metameric: Spectral uplifting via controllable color constraints. In ACM SIGGRAPH 2023 Conference Proceedings, pages 1–10.
Ward, G. and Wang, T. (2024). New hyperspectral rendering capabilities in radiance. Presented at the 22nd International Radiance Workshop, Salt Lake City, Utah, 2024. `https://www.radiance-online.org/community/workshops/2024-salt-lake-city-ut`.
Wei, J., Wu, H., Yue, H., Jia, S., Li, J., and Liu, C. (2023). Automatic extraction and reconstruction of a 3D wireframe of an indoor scene from semantic point clouds. International Journal of Digital Earth, 16(1):3239–3267.
Wienold, J. and Reetz, C. (2004). Evalglare–a new radiance-based tool to evaluate daylight glare in office spaces. In 3rd International RADIANCE workshop.
Wong, M. O., Sun, Y., Ying, H., Yin, M., Zhou, H., Brilakis, I., Kelly, T., and Lam, C. C. (2025). Image-based scan-to-BIM for interior building component reconstruction. Automation in Construction, 173:106091.
Xiaojuan, N., Man, W., Jing, T., Yinghui, W., et al. (2021). Structural wall facade reconstruction of scanned scene in point clouds. Advances in Electrical & Computer Engineering, 21(4).
Ye, M., Zhang, Y., Yang, R., and Manocha, D. (2015). 3d reconstruction in the presence of glasses by acoustic and stereo fusion. In Proceedings of the IEEE Conference on Computer Vision and Pattern Recognition, pages 4885–4893.
Yoo, H., Kim, K. Y., and Lee, K. H. (2009). Color calibration of hdr image under a known illumination for measuring reflectance property of materials. IEICE transactions on information and systems, 92(12):2548–2552.
Zhang, X., Cui, S., Cui, H., Yang, L., and Wu, T. (2017). Material appearance acquisition from a single image. In Seventh International Conference on Electronics and Information Engineering, volume 10322, pages 315–319. SPIE.
Zhong, M., Chen, X., Chen, X., Zeng, G., and Wang, Y. (2022). Maskgroup: Hierarchical point grouping and masking for 3D instance segmentation. In 2022 IEEE International Conference on Multimedia and Expo (ICME), pages 1–6. IEEE.
Zhou, X., Yan, D., Hong, T., and Ren, X. (2015). Data analysis and stochastic modeling of lighting energy use in large office buildings in china. Energy and Buildings, 86:275–287.

APPENDIX A

Uncertainty indicators

- Percentage Error (PE) for Total Annual Illumination (TAI).

$$100 * \frac{(TAI_i - TAI_{bm})}{TAI_{bm}} \tag{A.1}$$

Where:

TAI_i is Total Annual Illumination in [klx], and

TAI_{bm} is TAI for the benchmark model [klx].

- Mean Absolute Percentage Error (MAPE) for TAI.

$$\frac{100}{N} * |\frac{(TAI_i - TAI_{bm})}{TAI_{bm}}| \tag{A.2}$$

Where:

N is the number of iterations in the corresponding GLoD and MCoP.

- Root Mean Squared Error (RMSE) of the time-series annual simulation data averaged over all the iterations:

$$\frac{1}{N}\sum_{i=1}^{N}\sqrt{\frac{1}{H*G}\sum_{j=1}^{H}\left(\sum_{k=1}^{G}(x_{ijk} - \hat{x}_{ijk})^2\right)} \tag{A.3}$$

Where:

H represents the total number of occupancy hours between 8:00 and 17:00 throughout the year.

G is the total number of grid points within a space.

x_{ijk} denotes the illuminance value on the point k at time j in the i^{th} inaccurate iteration, and

$\hat{x}_{ijk}$ represents the benchmark value for the same point in time and space.

APPENDIX B

Results of the normality test

TABLE APP. B.1 Results of the normality test (p-value); normal distributions with p-values higher than 0.05 are marked with (*).

Space ID	GLoD	MCoP0.05	MCoP0.10	MCoP0.15	MCoP0.20
W01050	4	0.006	0.000	*0.216	0.017
	3	*0.451	0.000	0.003	0.000
	2	*0.470	0.002	0.000	0.001
	1	*0.373	0.000	0.000	0.001
	0	*0.433	0.003	0.000	0.000
DA_230	4	0.016	*0.076	0.001	0.001
	3	0.015	0.000	0.002	0.004
	2	0.008	0.003	0.000	0.000
	1	*0.111	0.000	0.001	0.015
	0	*0.126	0.008	0.000	0.002
DA_200	4	0.000	0.000	0.000	0.000
	3	0.002	0.003	0.001	0.000
	2	0.004	0.009	0.000	0.000
	1	*0.092	0.006	0.000	0.000
	0	0.002	0.000	0.000	0.000
	4	*0.131	0.000	0.010	0.004
	3	0.005	0.000	0.005	0.000
	2	*0.511	0.003	0.003	0.000

Continued on next page

Space ID	GLoD	MCoP0.05	MCoP0.10	MCoP0.15	MCoP0.20
MH_440	1	*0.056	0.000	0.001	0.000
	0	0.002	0.010	0.005	0.000
WBG550	4	0.001	*0.482	0.026	0.001
	3	*0.121	0.008	0.000	0.018
	2	*0.430	0.295	0.001	0.000
	1	*0.320	*0.106	0.021	0.002
	0	*0.760	0.004	0.002	0.001
WBG640	4	0.001	*0.483	0.027	0.001
	3	*0.121	0.008	0.000	0.018
	2	*0.438	*0.295	0.001	0.000
	1	*0.321	*0.107	0.022	0.002
	0	*0.763	0.005	0.002	0.002

APPENDIX C

UDI and TAI simulation results

TABLE APP. C.1 TAI [Mlx.hr/year]

Room	Manual		Semi-auto	
	Mean	STD	Mean	STD
W01050	0.40	0.47	0.47	0.55
WBG640	1.11	0.98	1.25	1.10
WBG550	3.23	2.51	3.75	2.90
DA200	0.57	0.49	0.82	0.69

TABLE APP. C.2 UDI_i [%]

Room	Manual		Semi-auto	
	Mean	STD	Mean	STD
W01050	65.90	22.88	60.82	24.17
WBG640	15.53	32.83	13.81	31.52
WBG550	13.38	28.74	12.18	27.70
DA200	59.47	22.92	48.31	25.41

TABLE APP. C.3 UDI_a [%]

Room	Manual		Semi-auto	
	Mean	STD	Mean	STD
W01050	33.10	21.45	37.87	22.41
WBG640	81.11	32.87	82.14	32.00
WBG550	60.47	26.84	55.09	27.61
DA200	38.11	21.16	47.86	22.96

TABLE APP. C.4 UDI_e [%]

Room	Manual		Semi-auto	
	Mean	STD	Mean	STD
W01050	0.98	3.34	1.28	4.16
WBG640	3.33	10.03	4.03	11.58
WBG550	26.13	22.15	32.71	26.65
DA200	2.40	3.99	3.80	5.87

APPENDIX D

Temporal Mean Relative Bias

TABLE APP. D.1 Summary of spatial TMRB values.

Room	Mean [%]	STD [%]
WBG640	14.20	13.06
WBG050	14.03	13.71
WBG550	28.93	40.39
DA200	22.40	145.76

APPENDIX E

Results of the three-channel illuminance-proxy

TABLE APP. E.1 Estimated RGB values for each sample grouped by Ground Truth (GT).

GT	Sample #	Estimated RGB
(0.12, 0.06, 0.08)	1	(0.13, 0.08, 0.10)
	2	(0.14, 0.08, 0.10)
	3	(0.14, 0.07, 0.10)
	4	(0.15, 0.08, 0.10)
	5	(0.14, 0.08, 0.10)
	6	(0.14, 0.08, 0.10)
	7	(0.16, 0.08, 0.12)
	8	(0.16, 0.09, 0.12)
	9	(0.15, 0.09, 0.11)
(0.77, 0.76, 0.58)	10	(0.79, 0.80, 0.54)
	11	(0.81, 0.83, 0.55)
	12	(0.78, 0.82, 0.50)
	13	(0.77, 0.80, 0.50)
	14	(0.76, 0.80, 0.48)
	15	(0.76, 0.81, 0.52)
	16	(0.79, 0.82, 0.54)
	17	(0.77, 0.80, 0.52)
	18	(0.81, 0.84, 0.53)
	19	(0.80, 0.84, 0.49)

Curriculum Vitae

Education

2021–2026	**Ph.D.**
	Delft University of Technology, Delft, The Netherlands
2018–2020	**M.Sc. in Building Physics**
	Shahid Beheshti University, Tehran, Iran
2013–2017	**B.Sc. in Architectural Engineering**
	Iran University of Science and Technology, Tehran, Iran
2009–2013	**Diploma in Mathematics and Physics**
	Ejei Highschool, Esfahan, Iran

Publications

JOURNAL

Forouzandeh, N., Nan, L., Stoter, J., Kim, D.-H., Brembilla, E. *Image-based characterisation of material optical properties for indoor daylight simulation*. Lighting Research & Technology. Under review.

Forouzandeh, N., Grobe, L. O., Brembilla, E. *Geometrical levels of detail for indoor daylight simulation*. Under review.

Forouzandeh, N. *Calibration of simulated spectral daylight for existing indoor spaces*.

Under review.

Forouzandeh, N., Brembilla, E., Nan, L., Stoter, J., Jakubiec, A. (2024). *Influence of geometrical levels of detail and inaccurate material optical properties on daylight simulation*. Energy and Buildings, 306, 113924. https://doi.org/10.1016/j.enbuild.2024.113924

Forouzandeh, N., Huang, J., Nan, L., Brembilla, E., Stoter, J. (2026). *Semi-automated indoor geometry reconstruction for daylight simulation*. Building and Environment, 289, 114045. https://doi.org/10.1016/j.buildenv.2025.114045

Forouzandeh, N., Zomorodian, Z. S., Shaghaghian, Z., & Tahsildoost, M. (2022). Room energy demand and thermal comfort predictions in early stages of design based on the Machine Learning methods. Intelligent Buildings International, 1-18. https://doi.org/10.1080/17508975.2022.2049190

Forouzandeh, N., Tahsildoost, M., & Zomorodian, Z. S. (2021). A review of web-based building energy analysis applications. Journal of Cleaner Production, 306, 127251.https://doi.org/10.1016/j.jclepro.2021.127251

Jami, S., **Forouzandeh, N.**, Zomorodian, Z. S., Tahsildoost, M., & Khoshbakht, M. (2021). The effect of occupant behaviors on energy retrofit: A case study of student dormitories in Tehran. Journal of Cleaner Production, 278, 123556. https://doi.org/10.1016/j.jclepro.2020.123556.

Forouzandeh, N., Ahmadi, J. H., & Nourkojouri, H. (2022). An Evaluation of Light Quantity and Quality in Reading Rooms, and Suggestions for Amendments; the Case of Shahid Beheshti University libraries.

CONFERENCE

Forouzandeh, N., Brembilla, E., Stoter, J., & Nan, L. (2023). Impact of geometrical resolution on long-term climate-based daylight metrics. In Building Simulation 2023 (Vol. 18, pp. 698-704). IBPSA.

Forouzandeh, N., Brembilla, E., & Jakubiec, J. A. (2022). Image-based material characterisation for daylight simulation using illuminance-proxy and artificial neural networks. In 14th European Lighting Conference: LUX EUROPA 2022 (pp. 171-178).

Masters supervision

2026 **Giorgos Iliopoulos**

Geomatics programme — *(Semi-)automatic modelling of indoor building 3D models for daylight simulation with LiDAR-enabled mobile devices*

Mentoring team: ***Nima Forouzandeh****, Ken Arroyo Ohori, Eleonora Brembilla*.

2024 **Maartje Damen**

Building Technology programme — *Enlightening Cities: Design for Natural Rhythm*

Mentoring team: ***Nima Forouzandeh****, Eleonora Brembilla, Giorgio Agugiaro*.

2024 **Thijs Hamilton**

Daylight Control Modelling with a Multi-Screen Shading Device

Civil Engineering programme — *Mentoring team: Roel Schipper, Sylvia Pont,* ***Nima Forouzandeh****, Christian Louter, Laura Franx.*

2022 **Tim Schouws**

Building Technology programme — *Measuring Daylight: The New European Standard and the Effect on Green Building Certificates*

Mentoring team: Eleonora Brembilla, Pirouz Nourian, Shervin Azadi, ***Nima Forouzandeh.***

Tutoring and lecturing during PhD

2025/26 **Advanced Building Physics** — Lecturer, CiTG

2024/25 **Advanced Building Physics** — Lecturer and Tutor, CiTG

2024/25 **Technolodge, Climate Design** — Tutor, BK

2023/24 **Advanced Building Physics** — Tutor, CiTG

2023/24 **Climate Design** — Lecturer and examiner, BK

2023/24	**MEGA** — Tutor, BK
2023/24	**Explore Lab Graduation** — Tutor, BK
2022/23	**MEGA** — Tutor, BK
2022/23	**Technolodge, Climate Design** — Tutor, BK
2021/22	**Technolodge, Climate Design** — Tutor, BK
2021/22	**Bucky Lab Engineering** — Tutor, BK

Conferences and workshops

2024	**LumeNet** — PhD Forum
2023	**Radiance workshop** — Semi-automatic daylight modelling for existing indoor spaces
2023	**IBPSA 2023 conference** — Impact of geometrical resolution on long-term climate-based daylight metrics
2022	**Radiance workshop** — Material and geometry for indoor daylight simulations.
2022	**LuxEuropa** — Image-based material characterisation for daylight simulation using illuminance-proxy and artificial neural networks

Professional experience

2019-2020	**Architect- Building Performance Specialist** — BSP Group, Tehran, Iran
2018	**Architect-Graphic Designer** — SEPID Group, Tehran, Iran
2017-2018	**Construction technical assistant** — Tandis-Ara Consultants, Lavasan, Iran
2014-2015	**Architect** — Chahar-Baq Nesf-e-Jahan Consultants, Baharestan, Iran

26#05

Modelling Daylight for Existing Indoor Spaces

Towards formalisation and automation of input data for robust simulations

Nima Forouzandeh

Despite the maturity of physically based daylight simulation tools, their broad applicability to existing buildings remains constrained. This is partly due to the lack of formal definitions that ensure comparability among models created in different contexts, partly due to inefficient techniques for input acquisition, and partly due to gaps in model calibration.
This work addresses these limitations by first defining different levels of geometric agreement between digital and real indoor spaces, termed Geometrical Levels of Detail (GLoD). These levels represent degrees of geometric completeness and resolution. The study quantifies how those degrees of representation translate into errors in daylight simulation results.
A similar framework is introduced for material inputs through Material Classes of Precision (MCoP). These classes represent different techniques for acquiring optical properties. The propagated uncertainty associated with each level of precision is systematically analysed to determine its influence on daylight simulation results.
Third, a semi-automatic pipeline is developed to reconstruct simulation-ready geometry from LiDAR point clouds. The workflow includes preprocessing, watertight reconstruction of permanent objects, and detection and reconstruction of window boundaries with minimal user interaction. Its performance is evaluated using daylight availability and glare metrics.
Fourth, image-based material characterisation techniques are assessed as accessible alternatives to laboratory measurements. Three techniques are validated, and their influence on daylight simulation results is quantified. A spectral uplifting method is further evaluated to reconstruct full spectral reflectance from RGB inputs for spectral daylight simulations.
Finally, a calibration workflow for indoor spectral daylight simulation is introduced to account for uncertainties related to exterior conditions and window characterisation. Measured spectral irradiance data are used to minimise simulation error. Together, these contributions enable practitioners and researchers to create a robust digital daylight model for existing indoor spaces.

A+BE | Architecture and the Built Environment | TU Delft BK